Fully-Additive Printed Electronics:

Synthesis and Characterization of Selenophene-Based p-Type Organic Semiconductor, and Formulation of P(VDF-TrFE)-Based Nanocomposite Dielectric

Hou Xiaoya

School of Electrical and Electronic Engineering

A thesis submitted to Nanyang Technological University in partial
fulfillment of the requirement for the degree of Doctor of Philosophy

2015

Acknowledgements

I would like to thank my PhD advisor Prof Chang Joseph (EEE), co-advisors Dr Zhang Jie (IMRE), Prof Hu Xiao (MSE), and Prof Ng Siu Choon (CBE). This research is multidisciplinary, embodying chemistry, physics, materials and microelectronics (fabrication).

I would like to thank Dr Ge Tong, Dr Zhang Xi, Zhou Jia, Ng Yi Kai Vincent, Ng Pei Jian Eileen, and Wang Meng Meng in our research group at NTU. My discussions with them have been highly stimulating and fruitful.

I would like to thank Dr Chen Hui, Dr Lu Yong, and Dr Ong Teng Teng at CBE/NTU, who also advised on the research work of organic semiconductor materials. I am grateful for Qiao Fen and Thelese (IMRE), who have been helpful with OPVs devices fabrication and characterization.

I would like to thank Dr Chang Kok Leong (IMRE), who helped me with the printer and the probe station. I am also obliged to Doreen (IMRE) for her great help with CP SEM measurements of the dielectric materials. I am grateful to Dr Xia Yijie (IMRE) for helping with the dielectric ink viscosity measurements.

Finally, I am very thankful to Nanyang Technological University for providing a PhD scholarship.

Table of Contents

Acknowledgements I

Table of Contents II

Summary V

Publications VII

Lists of Figures, Schemes and Tables VIII

List of Abbreviations and Symbols XV

Chapter 1 Introduction 1

1.1 Motivation 1

1.2 Objectives/Formulation of PhD research program 7

1.3 Contributions 8

1.4 Structure of the thesis 9

1.5 Conclusions 10

Chapter 2 Literature Review 11

2.1 The operating principle of OFETs 11

2.2 The electrical characteristics of OFETs 13

2.3 Charge transport in disordered organic materials 16

2.4 *p*-type organic semiconductors 19

2.5 *n*-type organic semiconductors 24

2.6 Gate dielectrics for OFETs 26

  2.6.1 Inorganic dielectrics 27

  2.6.2 Polymer dielectrics 28

  2.6.3 Polymer nanocomposite dielectrics 31

2.7 Printing methods for transistors and circuits 33

2.8 The operating principle of OPVs 39

2.9 The electrical characteristics of OPVs 40

2.10 Materials in OPVs 42

2.11 Conclusions 42

Chapter 3 Synthesis and Characterization Organic Semiconductors 44

3.1 Introduction 44

3.2 *p*-type organic semiconductor of PBTBS 45

- 3.2.1 Experimental 46
- 3.2.2 Synthesis of PBTBS 46
- 3.2.3 Optical properties of PBTBS 49
- 3.2.4 Electrochemical properties of PBTBS 51
- 3.2.5 Thermal and morphological properties of PBTBS 54
- 3.2.6 Characteristics of BHJ OPVs 55
- 3.2.7 External quantum efficiency of PBTBS 61
- 3.2.8 Characteristics of PBTBS-based OFETs 63

3.3 *n*-type organic semiconductor of T3PT3 64

- 3.3.1 Synthesis of T3PT3 65
- 3.3.2 Thermal properties of T3PT3 67
- 3.3.3 Optical properties of T3PT3 68
- 3.3.4 Electrochemical properties of T3PT3 70
- 3.3.5 Morphology of T3PT3 71
- 3.3.6 Characteristics of BHJ OPVs 72

3.4 Conclusions 74

Chapter 4 Fluoropolymers for Polymer Nanocomposite Dielectrics 76

4.1 Introduction 76

4.2 Fluoropolymer dielectrics 77

- 4.2.1 Experimental 80
- 4.2.2 P(VDF-HFP) as the gate dielectric 82

4.2.3 P(VDF-TrFE) as the gate dielectric 88

4.3 Polymer nanocomposite dielectric 94

4.3.1 Experimental 95

4.3.2 Morphology of P(VDF-TrFE)/PMMA/$BaTiO_3$ dielectrics 96

4.3.3 OFETs using P(VDF-TrFE)/PMMA/$BaTiO_3$ as gate dielectrics 99

4.4 OFET using printable dielectrics on an Al foil 103

4.5 Conclusions 109

Chapter 5 Formulation of Printable Dielectrics for Fully-Additive PE 110

5.1 Introduction 110

5.2 Experimental 111

5.3 OFETs using bilayer gate dielectrics 112

5.4 Fully-additive printed OFETs 120

5.5 Conclusions 133

Chapter 6 Conclusions and Future work 134

6.1 Conclusions 134

6.2 Future work 136

6.2.1 Materials engineering 136

6.2.2 Fully-additive printed electronics 138

References 139

Summary

This thesis pertains to printed electronics (PE), particularly to the first and second chains of the PE supply chain - Materials and Printing. In the Materials supply chain, the first objective is to design and synthesize novel π-conjugated organic semiconductor materials for organic photovoltaics (OPVs) and organic field-effect transistors (OFETs). The second objective is to formulate screen-printable high-*k* polymer nanocomposite dielectric inks for OFETs. In the Printing supply chain, the objective is to apply the synthesized or formulated materials to realize fully-additive (vis-à-vis subtractive or a combination of additive and subtractive) printed OFETs on flexible substrates.

In said first objective of the Materials supply chain, a novel π-conjugated selenophene and thiophene-based poly(2,5-bis(3-dodecylthiophen-2-yl)-2',2''-biselenophene) (PBTBS) was synthesized. This was explored as a promising electron donor material to be blended with [6,6]-phenyl-C61 butyric acid methyl ester (PCBM) for the fabrication of bulk heterojunction (BHJ) solar cells. The optical, electrochemical and photovoltaic properties of PBTBS were investigated and compared to those of poly(3,3'''-didodecylquaterthiophene) (PQT-12). A comparison of photovoltaic properties between polymer donors PBTBS and PQT-12 cells was also carried out. The results depicted that PBTBS cells had comparable photovoltaic parameters to PQT-12 cells. In particular, a short-circuit current (J_{sc}) of 1.7 mA/cm^2, an open voltage (V_{oc}) of 0.46 V, a fill factor (*FF*) of 0.32 and a power conversion efficiency (PCE) of 0.34% were achieved at 100 mW/cm^2.

In said second objective of the Materials supply chain, a screen-printable polymer nanocomposite dielectric material for OFETs was formulated. This dielectric ink composed of poly(vinylidenefluoride-co-trifluoroethylene) (P(VDF-TrFE)) and poly(methyl methacrylate) (PMMA) blend as the polymer binder, $BaTiO_3$ as the ceramic fillers, and fumed silica as the viscosity modifier. The thickness of dielectric P(VDF-TrFE)/PMMA/$BaTiO_3$/Silica (PPBS) printed on an aluminum (Al) foil was 3.5 μm, and the capacitance was 2.2 nF/cm^2. The breakdown voltage of this dielectric was greater than 200 V for 3.5 μm thickness. A small hysteresis was observed in the transfer characteristics under dual bias sweeping and there was a slight threshold voltage shift under multiple bias sweeping. 6,13-bis(triisopropylsilylethynyl) pentacene (TIPs-pentacene) OFETs were fabricated on an Al foil using PPBS as the gate dielectric, and featured a mobility of 0.01 cm^2/Vs with a threshold voltage of 2 V.

For the Printing supply chain, Fully-additive (vis-à-vis subtractive) printed TIPs-pentacene OFETs were successfully fabricated on PET substrate using optimized dielectric inks of P(VDF-TrFE)/PMMA/Silica (S1), and P(VDF-TrFE)/PMMA/$BaTiO_3$/Silica with $BaTiO_3$ loadings of 22% (S2), 36% (S3) and 52% (S4), respectively. The OFETs using dielectric S1 without $BaTiO_3$ had an order of magnitude higher leakage current (10^{-8} A at -60 V gate bias) compared to the leakage current (10^{-9} A) of OFETs using dielectric S2 at similar operating conditions. The desirable lower leakage current obtained from OFETs using dielectric S2 was attributed to good miscibility of modified $BaTiO_3$ and the polymer binder. With GPTMS-modified $BaTiO_3$ loading of 52%, the fabricated OFET can operate at a relatively low drain voltage of -20 V, and features a mobility of 0.2 cm^2/Vs and an I_{on}/I_{off} of 10^4. On this basis, this dielectric ink is promising for the realization of fully-additive printed analog and digital printed circuits.

Publications

1) Hou Xiaoya, Ng Siu Choon, Zhang Jie, Chang Joseph Sylvester. *Polymer Nanocomposite Dielectric Based on P(VDF-TrFE)/PMMA/BaTiO$_3$ for TIPs-Pentacene OFETs*, Organic Electronics, 2015. **17**: p. 247-252.

2) Hou Xiaoya, Xia Yijie, Ng Siu Choon, Zhang Jie, Chang Joseph Sylvester. *Formulation of Novel Screen-Printable Dielectric Ink for Fully-Printed TIPs-Pentacene OFETs*, RSC Advances, 2014. **4**: p. 37687-37690.

3) Qiao Fen, Hou Xiaoya, Lu Yong, Chen Hui, Liu Aimin, Hu Xiao, Ng Siu Choon. *Photovoltaic characterization of poly(2,5-bis(3-dodecylthiophen-2-yl)-2',2''-biselenophene) for organic solar cells*, Solar Energy Materials & Solar Cells, 2010. **94**: p. 442-445.

Lists of Figures, Schemes and Tables

List of Figures

Fig. 1-1 Organic Electronics Association's roadmap

Fig. 1-2 Supply chain for printed electronics

Fig. 2-1 Illustration of the working principle of OFETs (a) Energy level diagram at $V_G = 0$ and $V_D = 0$; (b) Operation for hole accumulation; (c) Operation for hole transport; (d) Operation for electron accumulation; and (e) Operation for electron transport

Fig. 2-2 Energy level diagram illustrating hole and electron trapping in organic semiconductor films

Fig. 2-3 Molecular orbital interactions of donor and acceptor units, resulting in a narrowing of the bandgap in donor-acceptor polymer

Fig. 2-4 Molecular structure of small molecule organic semiconductors

Fig. 2-5 Molecular structure of *p*-type polymer organic semiconductors

Fig. 2-6 Molecular structure of *n*-type organic semiconductors

Fig. 2-7 (a) A hydroxyl groups terminating the SiO_2 surface; and (b) Proposed mechanism of electron trapping at the hydroxyl groups terminating the SiO_2

Fig. 2-8 Physical cross-linked network of c-PMMA

Fig. 2-9 Synthesis of PMSQ

Fig. 2-10 Screen printing process

Fig. 2-11 Slot die coating process

Fig. 2-12 Crystal formation with coating direction of (a) Follow; and (b) Across channel

Fig. 2-13 Scheme of operation principle in OPVs

Fig. 2-14 *I-V* curves of OPV in dark (left) and under illumination (right)

Fig. 3-1 UV-vis spectra of PBTBS in the solution and the film state

Fig. 3-2 PL spectra of PBTBS in the solutions

Fig. 3-3 PL spectra of the PBTBS film and PBTBS/PCBM blend film

Fig. 3-4 Cyclic voltammogram of PBTBS film coated on a glass carbon electrode in 0.1 M Bu_4NBF_4/acetonitrile at scan rate of 100 mV/s (3 cycles)

Fig. 3-5 Cyclic voltammogram of BTBS film coated on a glass carbon electrode in 0.1 M Bu_4NBF_4/acetonitrile at scan rate of 100 mV/s

Fig. 3-6 (a) TGA curve of PBTBS under N_2; and (b) DSC curves of PBTBS at 10 °C/min heating rate under N_2

Fig. 3-7 Powder XRD patterns for PBTBS (a) before annealing; and (b) annealing at 80 °C

Fig. 3-8 Energy level diagram of the materials used for the solar cell devices

Fig. 3-9 Typical device structure of bulk heterojunction organic solar cell device

Fig. 3-10 The scheme of ITO glass after etching

Fig. 3-11 The schematic of shadow mask with the related size

Fig. 3-12 *I-V* characteristics of solar cells based on PBTBS/PCBM and PQT-12/PCBM

Fig. 3-13 *I-V* characteristics of solar cells based on PBTBS/PCBM and PQT-12/PCBM with and without thermal annealing treatment; respectively.

Fig. 3-14 The EQE curves of solar cells based on PBTBS/PCBM and PQT-12/PCBM

Fig. 3-15 The transfer (a) and output (b) characteristics of PBTBS-based OFETs

Fig. 3-16 (a) TGA curve of PBTBS under N_2; and (b) DSC curves of T3PT3 at 10 °C/min heating rate under N_2

Fig. 3-17 UV spectra of T3PT3 in the solution and the film state

Fig. 3-18 UV spectra of the pristine P3HT film and the P3HT/T3PT3 blend film

Fig. 3-19 PL spectra of the pristine P3HT film and the P3HT/T3PT3 blend film

Fig. 3-20 Cyclic voltammogram of T3PT3 film coated on a glass carbon electrode in 0.1 M Bu_4NBF_4/acetonitrile at scan rate of 100 mV/s: (a) negative scanning; and (b) positive scanning

Fig. 3-21 AFM topographic images of (a) T3PT3 film; and (b) P3HT/T3PT3 blend film

Fig. 3-22 Energy level diagram of the materials used for the solar cell devices

Fig. 3-23 *I-V* curves of the blend P3HT/T3PT3 solar cell device

Fig. 4-1 Molecular structure of two fluoropolymers

Fig. 4-2 Molecular structure of (a) TIPs-pentacene; and (b) PFBT

Fig. 4-3 Schematic cross section of BGBC OFETs

Fig. 4-4 AFM topographical (a) and phase (b) images of (i) pristine P(VDF-HFP) and P(VDF-HFP) blending PMMA concentrations of (ii) 10 wt%, (iii) 20 wt%, and (iv) 30 wt%

Fig. 4-5 Cross section SEM micrograph of P(VDF-HFP)/PMMA (30 wt%)

Fig. 4-6 The transfer (a) and output (b) characteristics of TIPs-pentacene OFETs with (i) P(VDF-HFP)/PMMA (10 wt%), (ii) P(VDF-HFP)/PMMA (20 wt%), and (iii) P(VDF-HFP)/PMMA (30 wt%) as gate dielectrics

Fig. 4-7 The *I-V* characteristics of TIPs-pentacene OFETs with P(VDF-HFP)/PMMA (30 wt%) as the gate dielectric under dual bias sweeping

Fig. 4-8 AFM topographical (a) and phase (b) images of (i) pristine P(VDF-TrFE) and P(VDF-TrFE) blended with PMMA concentrations of (ii) 10 wt%, (iii) 20 wt% , and (iv) 30 wt%

Fig. 4-9 Cross section SEM micrograph of P(VDF-TrFE)/PMMA (30 wt%)

Fig. 4-10 The transfer (a) and output (b) characteristics of TIPs-pentacene OFETs with (i) P(VDF-TrFE)/PMMA (10wt%), (ii) P(VDF-TrFE)/PMMA (20 wt%), and (iii) P(VDF-TrFE)/PMMA (30 wt%) as gate dielectrics

Fig. 4-11 Molecular structure of GPTMS

Fig. 4-12 AFM topographical (a) and phase (b) images of P(VDF-TrFE)/PMMA with $BaTiO_3$ loadings of (i) 9 wt%, (ii) 16 wt%, (iii) 23 wt%, (iv) 28 wt%, and (v) 33 wt%

Fig. 4-13 Cross section SEM micrograph of P(VDF-TrFE)/PMMA/$BaTiO_3$ (23 wt%)

Fig. 4-14 The transfer (a) and output (b) characteristics of TIPs-pentacene OFETs with (i) P(VDF-TrFE)/PMMA/$BaTiO_3$ (9wt%), (ii) P(VDF-TrFE)/PMMA/$BaTiO_3$ (16 wt%), and (iii) P(VDF-TrFE)/PMMA/$BaTiO_3$ (23 wt%) as gate dielectrics

Fig. 4-15 The transfer characteristics of TIPs-pentacene OFETs with P(VDF-TrFE)/PMMA/$BaTiO_3$ (23 wt%) as the gate dielectric under dual bias sweeping

Fig. 4-16 The transfer (a) and output (b) characteristics of TIPs-pentacene OFETs with P(VDF-TrFE)/PMMA/$BaTiO_3$ (28 wt%) as the gate dielectric

Fig. 4-17 The transfer characteristics of TIPs-pentacene OFETs with P(VDF-TrFE)/PMMA/$BaTiO_3$ (33 wt%) as the gate dielectric

Fig. 4-18 AFM topographical (a) and phase (b) images of the dielectrics of (i) PPS, and (ii) PPBS

Fig. 4-19 Cross section SEM micrograph of the dielectric PPBS on an Al foil

Fig. 4-20 The transfer (a) and output (b) characteristics of TIPs-pentacene OFETs using (i) the dielectric PPS, and (ii) the dielectric PPBS

Fig. 5-1 Cracked dielectric film on PET after thermal curing

Fig. 5-2 Schematic cross section of BGBC OFETs using the bilayer dielectric

Fig. 5-3 The transfer (a) and output (b) characteristics of TIPs-pentacene OFETs using the bilayer dielectrics of (i) PPBS on B1, (ii) PPBS on B2, (iii) PPBS on B3, and (iv) PPBS on B4

Fig. 5-4 The transfer characteristics of TIPs-pentacene OFETs using the bilayer dielectrics of (a) PPBS on B1, (b) PPBS on B2, (c) PPBS on B3, and (d) PPBS on B4 under dual bias sweeping

Fig. 5-5 The optic image of fully-additive printed OFETs on a PET substrate

Fig. 5-6 AFM topographical (a) and phase (b) images of the dielectrics of (i) S1, (ii) S2, (iii) S3, and (iv) S4

Fig. 5-7 Cross section SEM micrographs (a) dielectric S1, (b) S2, (c) S3, and (d) S4

Fig. 5-8 The comparison of leakage current of OFETs using S1 (a) and S2 (b) as gate dielectrics

Fig. 5-9 The transfer characteristics of TIPs-pentacene OFETs using the dielectric S1 at V_D of -20 V (a), -40 V (b), and -60 V (c); The output characteristics (d) of TIPs-pentacene OFETs using the dielectric S1

Fig. 5-10 The transfer characteristics of TIPs-pentacene OFETs using the dielectric S2 at V_D of -20 V (a), -40 V (b), and -60 V (c); The output characteristics (d) of TIPs-pentacene OFETs using the dielectric S2

Fig. 5-11 The transfer characteristics of TIPs-pentacene OFETs using the dielectric S3 at V_D of -20 V (a), -40 V (b), and -60 V (c); The output characteristics (d) of TIPs-pentacene OFETs using the dielectric S3

Fig. 5-12 The transfer characteristics of TIPs-pentacene OFETs using the dielectric S4 at V_D of -20 V (a), -40 V (b), and -60 V (c); The output characteristics (d) of TIPs-pentacene OFETs using the dielectric S4

List of Schemes

Scheme 3-1 Synthetic routes of PBTBS

Scheme 3-2 Synthetic route of T3PT3

List of Tables

Table 2-1 Basic parameters of OFETs based on *p*-type polymer semiconductors

Table 2-2 Basic parameters of common fully-additive printing technologies

Table 2-3 Fully-Additive printed circuits (and systems)

Table 3-1 Photovoltaic properties of PBTBS and PQT-12 in BHJ OPVs

Table 4-1 Properties of P(VDF-HFP)/PMMA and TIPs-pentacene OFETs with P(VDF-HFP)/PMMA as gate dielectrics

Table 4-2 Properties of P(VDF-TrFE)/PMMA and TIPs-pentacene OFETs with P(VDF-TrFE)/PMMA as gate dielectrics

Table 4-3 Compositions of polymer nanocomposite dielectrics of P(VDF-TrFE)/PMMA/$BaTiO_3$

Table 4-4 Properties of P(VDF-TrFE)/PMMA/$BaTiO_3$ and TIPs-pentacene OFETs with P(VDF-TrFE)/PMMA/$BaTiO_3$ as gate dielectrics

Table 4-5 Compositions of polymer nanocomposite dielectrics on an Al foil

Table 4-6 Properties of dielectrics of PPS and PPBS and TIPs-pentacene OFETs using dielectrics of PPS and PPBS

Table 5-1 Compositions of the buffer dielectric layers of PMMA/$BaTiO_3$/Silica

Table 5-2 Properties of TIPs-pentacene OFETs using the bilayer dielectrics

Table 5-3 Compositions of screen printable polymer nanocomposite dielectrics

Table 5-4 Properties of polymer nanocomposite dielectrics and TIPs-pentacene OFETs

List of Abbreviations and Symbols

PE	Printed electronics
OFETs	Organic Field-Effect Transistors
OLEDs	Organic Light-Emitting Diodes
OPVs	Organic Photovoltaics
OTFTs	Organic Thin-film Transistors
IMRE	Institute of Materials Research and Engineering
NSF	National Science Foundation
BGBC	Bottom Gate Bottom Contact
μ	Field-Effect Mobility
$I_{\mathrm{on}}/I_{\mathrm{off}}$	The Current on-to-off Ratio
V_{G}	Gate Voltage
V_{D}	Drain Voltage
I_{D}	Drain Source Current
V_{T}	Threshold Voltage
g_{m}	Transconductance
C	Capacitance
k	Dielectric Constant
ε_0	Vacuum Permittivity
d	Insulator Thickness
diF-TESADT	2,8-difluoro-5,11-bis(triethylsilylethynyl) anthradithiophene
TIPs-pentacene	6,13-bis(triisopropylsilylethynyl) Pentacene
DTBDT-C6	Dithieno[2,3-d;2,3-d]benzo[1,2-b;4,5-b]dithiophene
OTS	Octadecyltrichlorosilane

HMDS	Hexadimethyldisilazane
PFBT	Pentafluorobenzenethiol
GPTMS	3-glycidoxypropyltrimethoxysilane
BCB	Divinyltetramethylsiloxane-bis(benzocyclobutene)
CYTOP	Poly(perfluorobutenylvinylether)
c-PMMA	cross-linked Poly(methyl methacrylate)
BHJ	Bulk Heterojunction
D-A	Donor-Acceptor
ICT	Intramolecular Charge Transfer
ITO	Indium Tin Oxide
PEDOT	Poly(3,4-ethylenedioxythiophene)
PSS	Poly(styrene sulfonate)
PCBM	[6,6]-phenyl-C61 butyric acid methyl ester
PDA	Perylene Tetracarboxylic Dianhydride
PDI	Perylene-3,4:9,10-bis(dicarboximide)
PTCDA	perylene-3,4,9,10-tetracarboxylic dianhydride
NDI	Naphthalene-1,8:4,5-bis(dicarboximide)
P3HT	Poly(3-hexylthiophene)
PBTBS	Poly(2,5-bis(3-dodecylthiophen-2-yl)-2',2"-biselenophene)
F8T2	Poly(9,9'-dioctylfluorene-co-bithiophene)
PQT-12	Poly(3,3'''-didodecylquaterthiophene)
PBTTT	Poly(2,5-bis(3-alkylthiophen-2-yl)thieno[3,2-*b*]thiophene)
P(VDF-HFP)	Poly(vinylidene fluoride-co-hexafluoropropylene)
P(VDF-TrFE)	Poly(vinylidenefluoride-co-trifluoroethylene)
PMMA	Poly(methyl methacrylate)

EQE	External Quantum Efficiency
J_{sc}	Short Circuit Current Density
V_{oc}	Open-Circuit Voltage
FF	Fill Factor
PCE	Power Conversion Efficiency
PL	Photoluminescence
UV-vis	Ultraviolet-visible
CV	Cyclic Voltammetry
n-Bu_4NBF_4	Tetrabutylammonium Tetrafluoroborate
HOMO	Highest Occupied Molecular Orbital
LUMO	Lowest Unoccupied Molecular Orbital
Eg	Bandgap Energy
IP	Ionization Potential
EA	Electron Affinity
XRD	X-ray Diffraction
TGA	Thermogravimetric Analysis
DSC	Differential Scanning Calorimetry
GPC	Gel Permeation Chromatography

Chapter 1 Introduction

1.1 Motivation

Present-day electronics and electronics over the last four decades are predominantly silicon-based. This is in part because of the favorable characteristics of silicon-based devices and their associated processing properties, including the relative ease in crystal growth, purification and doping, high resolution fabrication and favorable electronic-transport properties such as high mobility (speed) and efficiency (for solar cells). The technological infrastructure of silicon-based electronics is mature with sophisticated commercial electronic design automation tools (Computer Aided Design) and manufacturing (and test and verification) processes. Not unexpectedly, at least for the mid-term, silicon-based electronics are projected to continue to dominate the electronics industry.

Printed electronics (PE) [1-15] is a general term commonly used to describe electronics based on organic semiconductor materials, usually in a solution-based form, making it possible to deposit materials onto a surface using additive or printing techniques. PE cannot compete with or replace silicon-based electronics, because it is slow (carrier mobility is typically more than three orders of magnitude slower) and its minimum feature size is large (also typically more than three orders larger) compared to silicon. However, PE is often deemed as complementary technology to silicon-based electronics. Its advantages [16] include the potential of an electronic ‘printing press’ that can produce electronic products on-demand (where production time goes from weeks to minutes), so inexpensive that they can be used wherever print media is used (where product cost falls from dollars to cents and hence disposable) and flexible (printed on flexible substrates such as paper, plastic, etc.) that they can be molded or bent to fit in odd and uneven spaces. In short, PE should ideally be Green (little/no toxic/corrosive, low-cost, print on-demand and scalable, and on flexible substrates).

Consequent to said attractive attributes, PE is expected to be increasingly ubiquitous. This is, in part, evident from the Organic Electronics Association's roadmap [17] for PE applications depicted in Fig. 1-1, and projection that printed electronics will grow from ~$8B in 2012 to $190B by 2025.

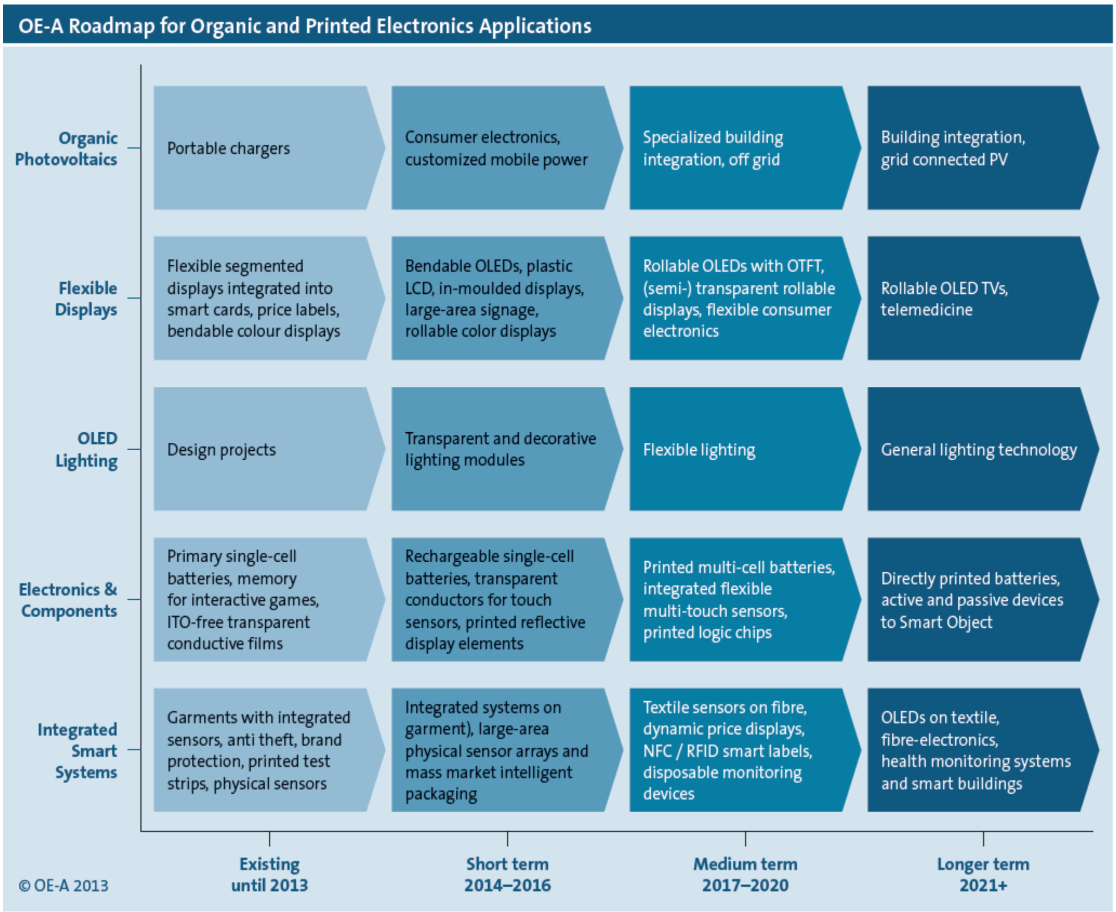

OE-A Roadmap for Organic and Printed Electronics Applications

	Existing until 2013	Short term 2014–2016	Medium term 2017–2020	Longer term 2021+
Organic Photovoltaics	Portable chargers	Consumer electronics, customized mobile power	Specialized building integration, off grid	Building integration, grid connected PV
Flexible Displays	Flexible segmented displays integrated into smart cards, price labels, bendable colour displays	Bendable OLEDs, plastic LCD, in-moulded displays, large-area signage, rollable color displays	Rollable OLEDs with OTFT, (semi-) transparent rollable displays, flexible consumer electronics	Rollable OLED TVs, telemedicine
OLED Lighting	Design projects	Transparent and decorative lighting modules	Flexible lighting	General lighting technology
Electronics & Components	Primary single-cell batteries, memory for interactive games, ITO-free transparent conductive films	Rechargeable single-cell batteries, transparent conductors for touch sensors, printed reflective display elements	Printed multi-cell batteries, integrated flexible multi-touch sensors, printed logic chips	Directly printed batteries, active and passive devices to Smart Object
Integrated Smart Systems	Garments with integrated sensors, anti theft, brand protection, printed test strips, physical sensors	Integrated systems on garment), large-area physical sensor arrays and mass market intelligent packaging	Textile sensors on fibre, dynamic price displays, NFC / RFID smart labels, disposable monitoring devices	OLEDs on textile, fibre-electronics, health monitoring systems and smart buildings

© OE-A 2013

Fig. 1-1 Organic Electronics Association's roadmap [17]

Somewhat unlike its silicon-based counterpart, the supply chain (or equivalently, the complete manufacturing flow) of PE, depicted in Fig. 1-2 [17], is somewhat less complex. Despite the immense interest within the academic and industry communities, PE technology remains nascent. This could perhaps be explained by the challenges and ensuing immaturity of each chain of the supply chain.

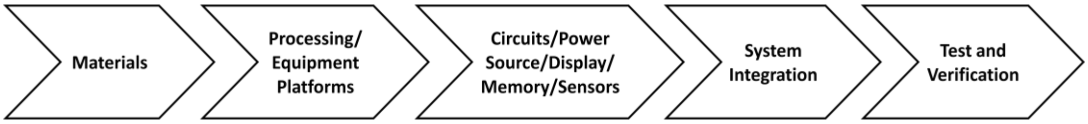

Fig. 1-2 Supply chain for printed electronics [17]

In the first chain, ‘Materials’ at left-most in Fig. 1-2, the principle challenges are the very low (relative to silicon) charge carrier mobility, poor electrical conductivity of materials and process stability. In the perspective of the PE community, charge carrier mobility over 1 cm^2/Vs for processable semiconductors will be needed. These values have to be achieved in the final device using high volume process. Functional organic semiconductor materials with a charge carrier mobility in the order of 5-10 cm^2/Vs when printed would be considered a breakthrough [16], since it would enable more complex device. Moreover, as most materials applied in PE are made from organic, carbon-based compounds, they suffer from degradation due to the intolerance of most organic semiconductors to UV radiation, water and oxygen. Not unexpectedly, the process parameters of PE such as charge carrier mobility and threshold voltage vary significantly when these conditions change. Put simply, the stability of the semiconductor in the printed transistor is important to obtain reliable printed circuits.

A further formidable challenge is the unbalanced hole and electron mobility of organic semiconductors. The device performance, particularly the charge carrier mobility, of soluble *n*-type organic semiconductors remains significantly lower (typically 10 times) than that of the *p*-type organic semiconductors. This renders poor performance complementary *p*-type and *n*-type PE circuits, particularly different rise and fall transistors of digital circuits [18]. In order to realize practical complementary PE circuits, it is necessary that air-stable, solution-processable *n*-type small molecules and polymeric semiconductors are available for organic field-effect transistors (OFETs) with device performance comparable to that of *p*-type organic semiconductors - to date, this is yet unavailable.

Apart from high-mobility organic semiconductor to realize high-performance PE devices (OFETs and capacitors), it is also necessary that high-capacitance gate dielectrics for low-voltage operation are available. PE electronic circuits operate at relatively high supplied bias ($V_{DD} \geq 60$ V), which is largely unacceptable for practical reasons. Instead, the desired operating voltage should be reduced to ≤ 10 V [19]. The capacitance can typically be increased either by increasing the dielectric constant (k) or decreasing the thickness (d) of the gate dielectric. The latter is particularly challenging for the additive-printed processes (vis-à-vis subtractive process; see later) where a relatively thick layer is often needed to be printed to prevent short circuits. To realize relatively high capacitance, the printed thick gate dielectrics should be counterbalanced by using high-k dielectrics. Furthermore, in PE the gate dielectric materials must meet the requirements of low processing temperature, good compatibility with the flexible substrate and the organic semiconductors. Commercially available dielectric materials are largely inadequate for PE, and the PE research community is actively developing formulation of printable high-capacitance dielectric inks. Collectively, these shortcomings result in low speed and somewhat unreliable electronics.

In the second chain, ‘Processing Equipment/Platform’, the equipment for fabricating PE continues to evolve, where the equipment used is typically adapted from that employed by the silicon-fabrication and the print art media. While the equipment employed by the silicon-fabrication offers relatively sophisticated PE circuits, particularly high resolution (e.g. $< 5\ \mu$m), the cost of the printed circuits is high and the process is not Green - contravenes the spirit of PE, delineated earlier. The equipment employed by the print art media, on the other hand, suffers from poor resolution and registration (alignment between different layers); see later.

In general, the PE printing technologies can be classified as either 'Subtractive' or 'Additive' processes. Subtractive-based processes include Laser Ablation [20-23] and Photolithography [24], and these processes are largely based on silicon IC fabrication processes [15]. As they involve a complex sequence of depositions, and etchings (a subtractive step), this process is expensive; hence somewhat contravening the spirit of PE. The advantages of these processes are relatively high charge carrier mobility (high speed), and high resolution.

Additive processes, on the other hand, involve only depositions where each printed layer is deposited by layer-by-layer to realize transistors and passive components, etc. As depositions are process-simple, the equipment is unsophisticated and the ensuing cost is low/cheap. Several fully-additive processes [25-27] have been reported, and arguably, the most advanced Fully-Additive process is that reported by the NTU research group [15] where the author of this thesis is associated with. This Fully-Additive process features printed transistors with high (~1.5 cm^2/Vs) semiconductor carrier-mobility [15], ~3x higher than competing state-of-the-art Fully-Additive processes [28] and comparable to Subtractive processes [29]. Nevertheless, the primary shortcoming is the larger minimum feature size (from 10 μm to larger than 100 μm), resulting in low circuit density and reduced speed. In many cases, as PE is viewed as complementary technology to silicon, the cost is of paramount importance and these shortcomings can be tolerated in many practical applications.

Not surprisingly, in light of the shortcomings of the first two chains, the ensuing third chain, ‘Circuits/Power Source/Display/Memory/Sensor’, is challenging and the slow, inconsistency, and unreliability (unless specific remedial processing steps are employed) attributes of PE circuits need to be accommodated. It is generally accepted that PE circuits are ‘poor cousins’ to their silicon counterparts. Nevertheless, these attributes conversely present the opportunity for 'new' or 'adapted' applications that are insensitive or tolerant to these shortcomings, particularly technologies that are compatible with low-cost printing techniques. These include circuits embodying OFETs [30], organic light-emitting devices (OLEDs) [31], organic photovoltaics (OPVs) [32, 33], electronic paper, wearable electronics, flexible batteries, sensors, and perhaps sophisticated circuits and systems [34], as depicted in Fig. 1-1.

The fourth chain collectively encompasses the former three - the system integration of materials, its processing and circuit design. Finally, as depicted in the last chain, the PE product has to be tested and verified.

In summary, PE technology embodies multidisciplinary technologies. PE technology remains nascent, where many technological issues remain unresolved, particularly for relatively sophisticated applications.

This PhD project is part of a larger PE program supported by two A*STAR grants (one in collaboration with the Institute of Materials Research and Engineering (IMRE, Singapore)) and an NSF (National Science Foundation, USA; in collaboration with Caltech) grant. The collective long-term intentions are to realize relatively sophisticated PE circuits and systems; congruous with the latter part of the 'medium-term' and for the 'long-term' tabulated in Fig. 1-1, and where the PE printing is based on a Fully-Additive process, thereby fully congruous with the spirit of PE - Green, Low-Cost, Print On-Demand and Scalable, and on Flexible Substrates.

1.2 Objectives/Formulation of PhD research program

The grand vision of this PhD research program pertains to the fabrication of relatively sophisticated PE circuits and systems where said fabrication is Fully-Additive, thereby congruous to said spirit of PE. Particularly, in view of the numerous principle challenges within all chains of PE, the objectives of this PhD program will be limited to the first two PE chains in Fig. 1-2 - research on the design and synthesis of organic semiconductors, formulation of printable dielectrics and printing thereof.

The specific objectives are:

(i) Design and synthesize novel organic semiconductors via molecular engineering, and to investigate their properties for the application of OPVs and OFETs using the standard silicon-based fabrication;

(ii) Formulate high-capacitance dielectric materials for OFETs in PE, and realization thereof in a printable form for OFETs fabrication; and

(iii) Following (i) and (ii), to fabricate fully-additive printed low-operating-voltage OFETs on a flexible substrate using said organic semiconductors and said formulated high-capacitance dielectric inks.

1.3 Contributions

The contributions to Specific Objective (i), pertaining to the organic semiconductor, included the synthesis of an air-stable and solution-processable π-conjugated organic semiconductor. This versatile *p*-type organic semiconductor of PBTBS was applied as a promising donor material to be blended with PCBM for the fabrication of bulk heterojunction (BHJ) OPVs. These results are detailed in Chapter 3, and have been published [35] in the Solar Energy Materials & Solar Cells journal.

The contributions to Specific Objective (ii), pertaining to the dielectric, included the successful formulation of a polymer nanocomposite dielectric ink. These results are detailed in Chapter 4, and have been published [36] in the Organic Electronics journal.

The contributions to Specific Objective (iii), pertaining to the fabrication of fully-additive printed low-operating-voltage OFETs, included the successful fabrication of Fully-additive (vis-à-vis subtractive) printed TIPs-pentacene OFETs on a flexible substrate. Based on the results of dielectric ink formulation delineated in Chapter 4, the dielectric ink composition was optimized to make good compatibility with the polyethylene terephthalate (PET) substrate. This dielectric ink is promising for the realization of fully-additive printed analog and digital printed circuits. These results are detailed in Chapter 5, and have been published [37] in the Royal Society of Chemistry (RSC) Advances journal.

In summary, contributions are made for said Specific Objectives (i), (ii) and (iii).

1.4 Structure of the thesis

Chapter 1 provides an introduction to PE, and delineates the motivation, the objectives, the formulation and the contributions of this PhD research program. In Chapter 2, the electrical characteristics of OFETs are reviewed, followed by the charge transport mechanism and the developments of organic semiconductors, and the applications of dielectric materials for OFETs, additive printing methods for PE, and finally, a review of the operating principle and the electrical characteristics of OPVs. Chapter 3, largely an extraction of the author's publication [35], delineates the research work towards Specific Objective (i) - synthesis, characterization, and application of organic semiconductors for OPVs and OFETs.

Chapter 4, largely an extraction of the author's publication [36], delineates the formulation of a polymer nanocomposite dielectric based on high-*k* fluoropolymers. The effects of different concentrations of low-*k* amorphous polymer and high-*k* nanoparticles on dielectric properties were investigated. TIPs-pentacene OFETs using this formulated dielectric were fabricated on an aluminium (Al) foil as the common gate and characterized under ambient atmosphere. The formulation of printable polymer nanocomposite dielectric ink was also preliminarily explored for fully-additive printed devices. The dielectric ink based on P(VDF-

TrFE)/PMMA/$BaTiO_3$/Silica (PPBS) was formulated for TIPs-pentacene OFETs fabrication on the Al foil.

Chapter 5, largely an extraction of the author's publication [37], delineates the optimization of the ink formulation to obtain compatibility between the dielectric ink and the PET substrate as well as patterned gate electrodes. This is to allow the transfer of the dielectric ink from the Al foil to the PET substrate. Eventually, fully-additive printed OFETs using the optimized dielectric ink were achieved.

Chapter 6 delineates the overall conclusions of this PhD program and provides suggestions for future research work.

1.5 Conclusions

This introductory chapter has delineated the motivations of this PhD program which pertains to the first and second supply chains of PE: ‘Materials’ and ‘Processing/Equipment Platforms’. The objectives and formulation of this PhD research program have been described, including the contributions and the overall structure of this PhD thesis.

Chapter 2 Literature Review

This chapter provides a literature review of PE technology and serves as a preamble to the author's contributions delineated in Chapters 3, 4 and 5.

In Section 2.1 and Section 2.2, the operating principles of OFETs and the essential parameters and characteristics of OFETs are reviewed. In Section 2.3, the charge transport mechanism by the hopping process in organic semiconductor materials is reviewed.

In Sections 2.4, 2.5 and 2.6, the development of *p*-type organic semiconductors, *n*-type organic semiconductors and gate dielectrics are reviewed, respectively. In Section 2.7, the different reported printing methods are reviewed for single transistor device and complex-circuit fabrication.

In Section 2.8, 2.9 and 2.10, the operating principle, the electrical characteristics and materials of OPVs are reviewed, respectively. Section 2.11 draws the conclusions for this review chapter.

2.1 The operating principle of OFETs

For a given source-drain voltage, V_D (with $V_S = 0$), the current that flows from the source electrode to the drain electrode through the organic semiconductor layer is a function of the gate-source voltage, V_G. When no gate bias is applied, as depicted in Fig. 2-1(a), as there is largely no charge carrier, the current will be relatively small owing to the low conductivity of the organic semiconductor; in Fig. 2-1, the ordinate height indicates the energy level. When a negative gate voltage is applied with $V_D = 0$

and $V_D < 0$, as depicted in Fig. 2-1(b) and (c) respectively, a large electric field is induced to enhance the highest occupied molecular orbital (HOMO) and the lowest unoccupied molecular orbital (LUMO) levels of the organic semiconductor. When the gate voltage is sufficiently large, the HOMO level of the organic semiconductor will match the work function of the electrodes. Electrons will subsequently be injected from the organic semiconductor into the electrodes, and holes will remain in the semiconductor and become mobile. These types of organic semiconductors are termed as *p*-type semiconductors.

Conversely, when a positive gate voltage is applied with $V_D = 0$ and $V_D > 0$, as depicted in Fig. 2-1(d) and (e) respectively, a large electric field is induced to lower the HOMO and LUMO levels of the organic semiconductor. When the gate voltage is sufficiently large, the LUMO level of the organic semiconductor will match the work function of the electrodes. In this case, the electrons become mobile in the organic semiconductors termed as *n*-type semiconductors. There are also types of organic semiconductors that can transport both holes and electrons, and are termed as ambipolar semiconductors.

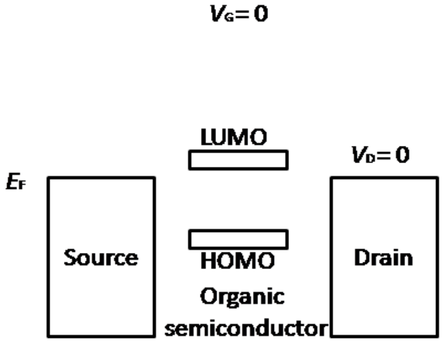

(a)

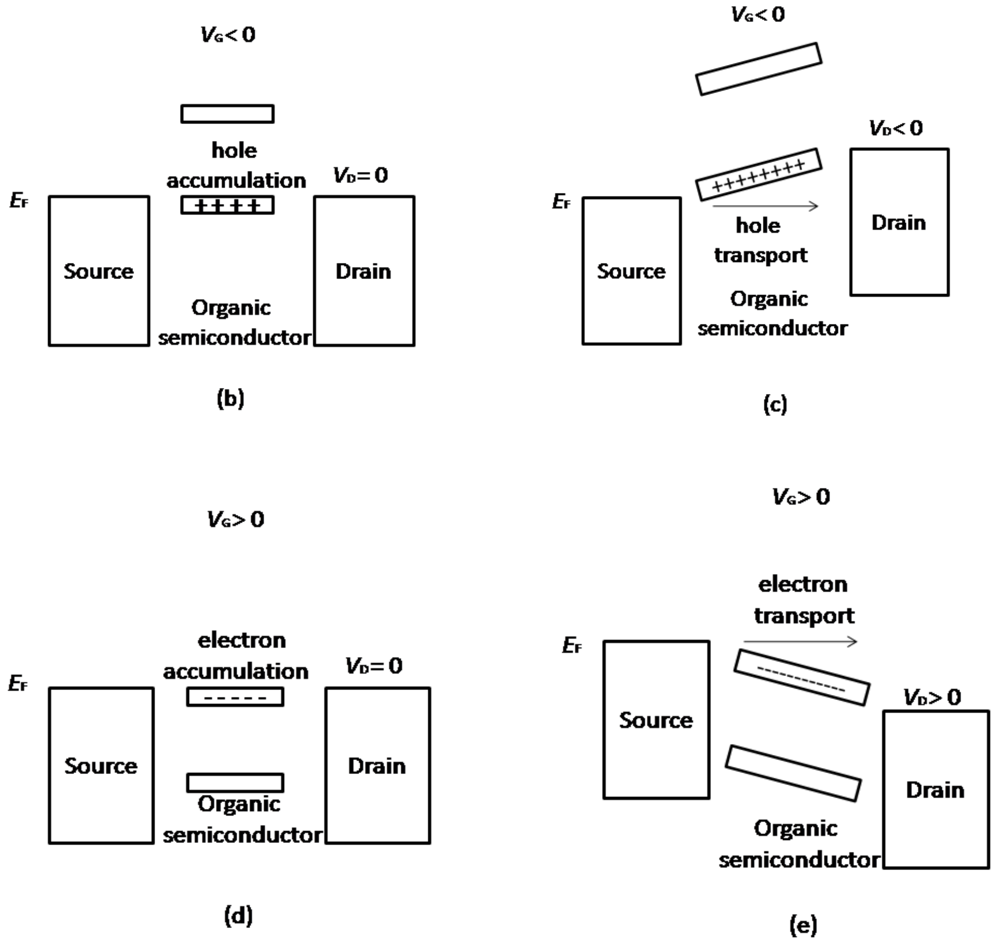

Fig. 2-1 Illustration of the working principle of OFETs (a) Energy level diagram at $V_G = 0$ and $V_D = 0$; (b) Operation for hole accumulation; (c) Operation for hole transport; (d) Operation for electron accumulation; and (e) Operation for electron transport

2.2 The electrical characteristics of OFETs

The essential parameters of OFETs with organic semiconductors as the active channel include the threshold voltage (V_T), on/off current ratio (I_{on}/I_{off}), and the charge carrier mobility (μ). The charge carrier mobility μ is the average drift velocity of the charge carrier per unit electric field, and determines the operating speed of OFETs. Generally, a high μ is desirable for a large saturation current. The key quantity that characterizes the charge transport in the organic semiconductor is the charge carrier mobility, and the charge transport mechanism will be delineated in Section 2.3. V_T determines the switching behaviour of OFETs, and is used to control and bias OFETs to operate in a proper regime to facilitate the function of circuits [38, 39]. $I_{\mathrm{on}}/I_{\mathrm{off}}$ is the ratio between the on-state drain current and the off-state drain current of the OFETs. Collectively, these parameters are influenced by several factors, including the morphology of organic semiconductors, dielectric materials and device geometry, etc. In general, a high-performance OFET should feature a high charge carrier mobility, a low threshold voltage, and a large on/off current ratio.

There are two common methodologies to characterize the OFET performance, including the transfer characteristics (drain current vs gate voltage V_{G}, e.g. see Fig. 5-12(c)) and the output characteristics (drain current vs drain voltage, e.g. see Fig. 5-12(d)). The output characteristics are obtained by keeping V_{G} constant and sweeping V_{D}, and repeating for different V_{G} voltages. Depending on V_{G}, the organic transistor device may operate in three regions: cutoff region, linear region and saturation region. According to the common model of OFETs, at the linear region with low $V_{\mathrm{D}} < (V_{\mathrm{G}} - V_{\mathrm{T}})$, the drain current I_{D} increases linearly with V_{D} and is approximately expressed by the equation 2.1 [40]:

$$I_{\mathrm{D}} = \frac{W}{L}\mu C\left(V_{\mathrm{G}} - V_{\mathrm{T}} - \frac{V_{\mathrm{D}}}{2}\right)V_{\mathrm{D}} \qquad (2.1)$$

where W is the channel width,

L is the channel length,

C is the capacitance of gate dielectric per unit area

V_{T} is the threshold voltage, and

μ is the field-effect mobility.

The mobility in the linear region can be calculated from the transconductance (g_m) by the equation 2.2:

$$\mu = \frac{g_\mathrm{m} L}{W C V_\mathrm{D}} = \frac{L}{W C V_\mathrm{D}} \left(\frac{\partial I_\mathrm{D}}{\partial V_\mathrm{G}}\right)_{V_\mathrm{D}=\mathrm{const}} \qquad (2.2)$$

With $V_\mathrm{D} > (V_\mathrm{G} - V_\mathrm{T})$, the drain current I_D tends to saturate due to the pinch-off of the accumulation layer, and is approximately determined by the equation 2.3. In the saturation regime, the mobility can be ascertained from the slope of the plot of $|I_\mathrm{D}|^{1/2}$ versus V_G in the equation 2.3 [40]:

$$I_\mathrm{D} = \frac{W}{2L} \mu C (V_\mathrm{G} - V_\mathrm{T})^2 \qquad (2.3)$$

The charge carrier mobility μ extracted from the OFET *I*-*V* characteristics is generally higher in the saturated regime than that in the linear regime as a result of different electric-field distributions. Saturation mobility is much closer to a material parameter and linear mobility is affected by series resistance of the electrodes or the contact resistance at the interface between the electrodes and the semiconductor [40]. Strictly speaking, the equations 2.1 and 2.3 are valid only when the mobility is constant. In some cases, the mobility can be found to be gate voltage dependent. It was reported [41] that the charge carrier mobility of a pentacene OFET increased from a relatively low value of 0.02 cm^2/Vs at -14 V to 1.26 cm^2/Vs at -146 V.

2.3 Charge transport in disordered organic materials

The charge transport in organic materials is different from that in inorganic semiconductors. Instead of energy band structures (valence and conduction bands) formed by inorganic materials, the HOMO and LUMO levels were formed in organic materials. Charge carriers (hole and electron) for organic materials correspond to the cation and anion radicals of a molecule. It has been generally accepted that the charge transport in disordered organic materials takes place by a hopping process [42]. Electrons are sequentially transferred from a neutral molecule to its cation radical through the HOMO level for hole transport; electrons from the anion radical of a molecule to the neutral molecule through the LUMO level for electron transport. Hole and electron differ from their sensitivity to trapping at defects or impurities. The transport of electrons in a wide range of semiconducting polymers is limited by trapping. Most organic semiconductors typically are *p*-type, that is, the hole mobility exceeds the electron mobility by orders of magnitude.

As depicted in Fig. 2-2, the HOMO level of most organic semiconductors is located at ~ -5 eV to -6 eV versus vacuum, whereas the LUMO level ranges from ~ -2 eV to -3 eV [43]. Defects or impurities frequently have empty orbitals below -3 eV (green line) that can take up an electron. Filled orbitals above -5 eV, which are suitable for accepting holes, are more elusive. On one hand, the way to obtain balanced electron and hole mobility is to eliminate the electron traps. It was found that the hydroxyl groups at the interface of the semiconductor/dielectric are responsible for the electron trapping. When dielectric materials free of hydroxyl groups were used, the electron trapping was inhibited to achieve *n*-type transistor [44].

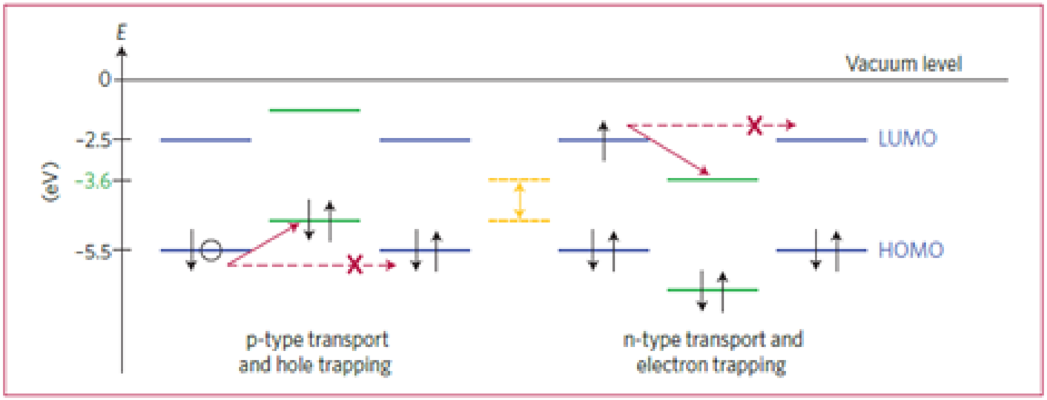

Fig. 2-2 Energy level diagram illustrating hole and electron trapping in organic semiconductor films [43]

On the other hand, balanced electron and hole mobility can be achieved in low bandgap organic semiconductors. Construction of low bandgap polymers is attainable by the following approaches: (1) enlargement of the π systems using fused aromatic rings; (2) construction donor-acceptor (D-A) alternating backbones with an electron-rich donor and electron-deficient acceptor unit; (3) stabilization of the quinoid resonance structure; (4) attachment of strong electron-withdrawing substituents [45]. By using or combining these approaches, hundreds of conjugated polymers have been prepared in the last decade in pursuit of ideal material. Among them, the D-A alternating backbones have attracted much interest in design of low bandgap organic semiconductors. As depicted in Fig. 2-3, the two new occupied molecular orbitals (one is lower and the other is higher than the two initial HOMO levels of the two moieties) are generated by the molecular orbital hybridization of the HOMO level of the donor group interacted with that of the acceptor group by covalent bond connection. Two new unoccupied molecular orbitals are also generated in a similar manner after the molecular orbital hybridization. Hence, the overall effect of this redistribution of frontier molecular orbitals is the formation of a higher lying HOMO level and a lower lying LUMO level in the conjugated polymer chain, thereby resulting in a narrow band gap [46].

Moreover, Meijer et al. [47] report ambipolar behavior in three classes of organic semiconductors that can be solution-processed. First is the blends of *p*- and *n*-type conjugated polymers; second is the low bandgap conjugated polymer; third is the formation of a weak inversion layer in common *p*-type organic semiconductor. These results establish that ambipolar conduction is generic feature of organic semiconductors.

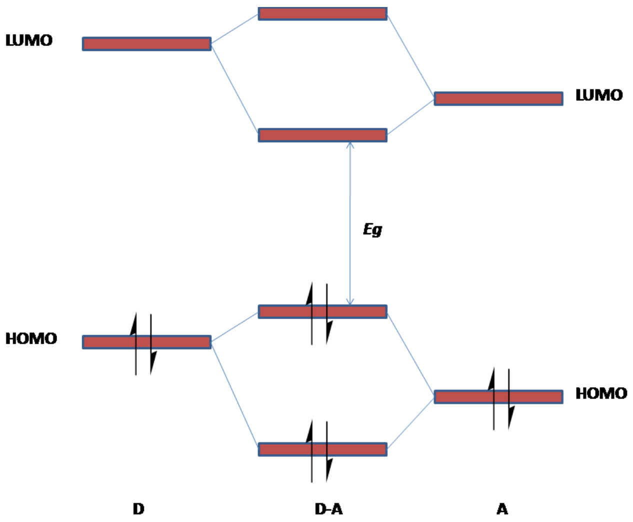

Fig. 2-3 Molecular orbital interactions of donor and acceptor units, resulting in a narrowing of the bandgap in donor-acceptor polymer [46]

In summary, the design of the organic semiconductor is of specific interest in this thesis for OPVs in PE, and this will be presented in Chapter 3. Of specific interest is the synthesis of a *p*-type polymer semiconductor with the incorporation of selenophene moieties in the polymer backbone to achieve good optical and electrochemical properties; and the synthesis of a *n*-type small molecule semiconductor via D-A molecular structure for OPVs will also be presented in Chapter 3.

2.4 *p*-type organic semiconductors

Organic semiconductor materials for OFETs may be generally classified into two main groups, small molecules and polymers. The charge carrier mobility of small molecule single crystals of pentacene and rubrene [48, 49] is largely comparable to that of amorphous silicon.

In general, high-performance small molecule semiconductors such as pentacene are not readily solution-processable due to their poor solubility, and require vacuum deposition, thereby limiting their application in PE. Nevertheless, recent solution-processable, high-mobility pentacene derivatives have been intensely researched by the PE community [29, 50, 51]. While the substitution of pentacene on carbon atoms in positions 6 and 13 greatly improves its chemical stability and solubility, the nature of alkyl substituents on the silicon atom allows the crystallization of the molecule to be finely controlled. 2,8-difluoro-5,11-bis(triethylsilylethynyl) anthradithiophene (diF-TESADT) and 6,13-bis(triisopropylsilylethynyl) pentacene (TIPs-pentacene) are prototypes in this new family. Due to the their crystallization mode in two dimensions with the π-conjugated core favourably oriented in the direction parallel to the molecular plane, the TIPs-pentacene and diF-TESADT prove among the best suited molecules for applications in transistors. Excellent levels of performance and stability have been demonstrated with mobilities of 1 cm^2/Vs for OTFTs based on organic semiconductor layers deposited by a solution process. The interest of the scientific community in this new class of soluble organic semiconductors with high mobility was therefore continually increasing up to commercialization of TIPs pentacene by Sigma-Aldrich in 2009. Due to its ease of the morphology control when deposited from solution, TIPs-pentacene is chosen as the active semiconductor for OFETs fabrication in this PhD research - see Chapters 4 and 5 later. Fig. 2-4 depicts the molecular structure of small molecule organic semiconductors.

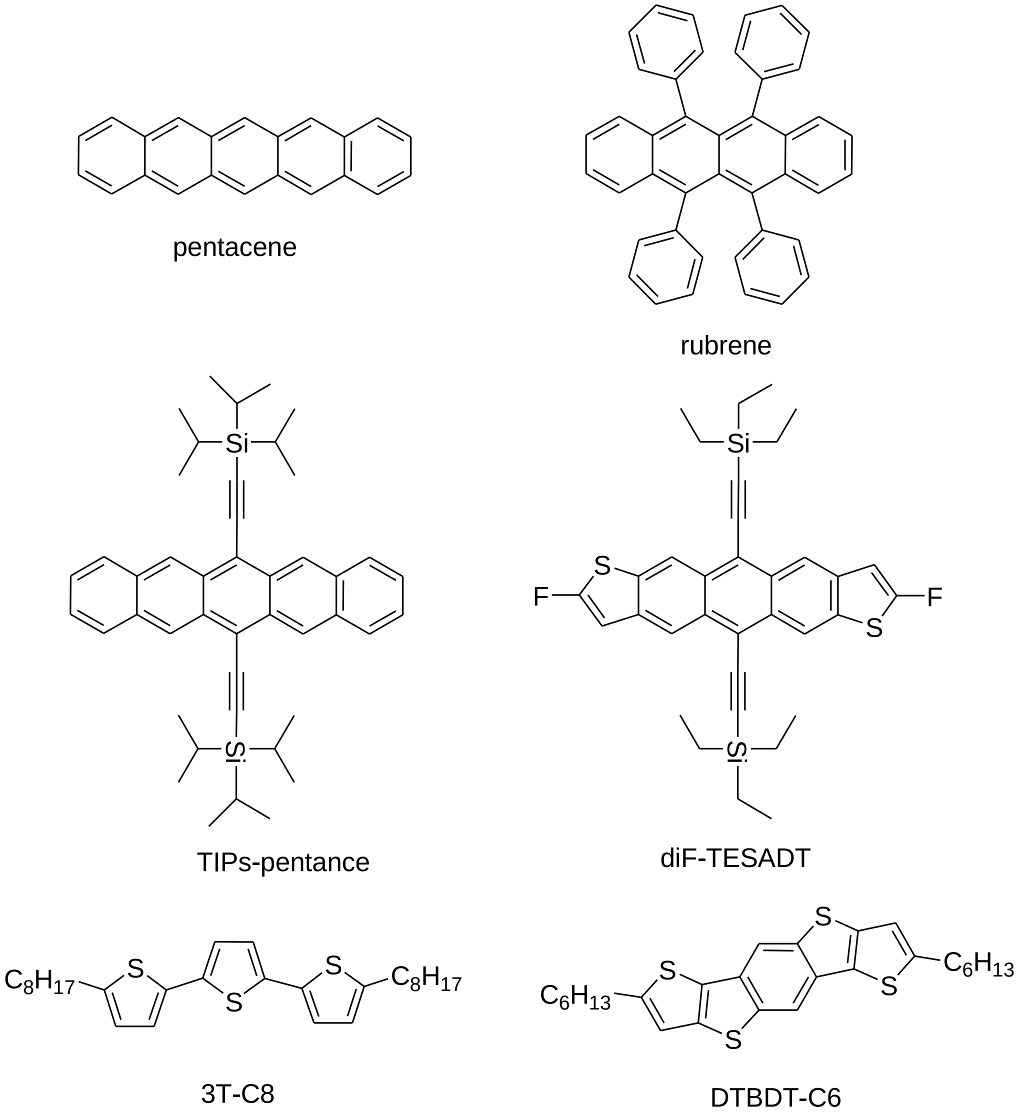

Fig. 2-4 Molecular structure of small molecule organic semiconductors

Another important class of small molecules is based on the oligothiophene and its derivatives. A simple substituted terthiophene with octyl chains (3T-C8) leads to a liquid crystal semiconductor with a mobility of 0.1 cm^2/Vs for thin films deposited by spin-coating [52]. In addition to graft solubilizing side-groups, one approach consists of the rigidification of conjugated systems. Dithieno[2,3-d;2,3-d]benzo[1,2-b;4,5-b]dithiophene compound (DTBDT-C6) gives high performing transistors with mobilities up to 1.7 cm^2/Vs [53].

Polymer semiconductors, on the other hand, often feature better solubility but degraded device performance compared to small molecule semiconductors. Fig. 2-5 depicts the molecular structures of several typical *p*-type organic semiconductors that have gained some popularity. Regioregular head-to-tail poly(3-hexylthiophene) (HT-P3HT) exhibits a mobility of 0.1 cm^2/Vs and an I_{on}/I_{off} of 10^6 under inert atmosphere [54], but suffers from poorer mobility and significantly lower I_{on}/I_{off} when the devices were characterized under ambient atmosphere [55]. HT-P3HT features a lamellar structure with all the thienylene moieties along the backbone held in coplanarity by intermolecular side-chain alignment, thereby allowing efficient charge transport by hopping. However, the highly delocalized π-conjugation system of HT-P3HT in the coplanar conformation may lead to an increased HOMO level, and a tendency to oxidative doping.

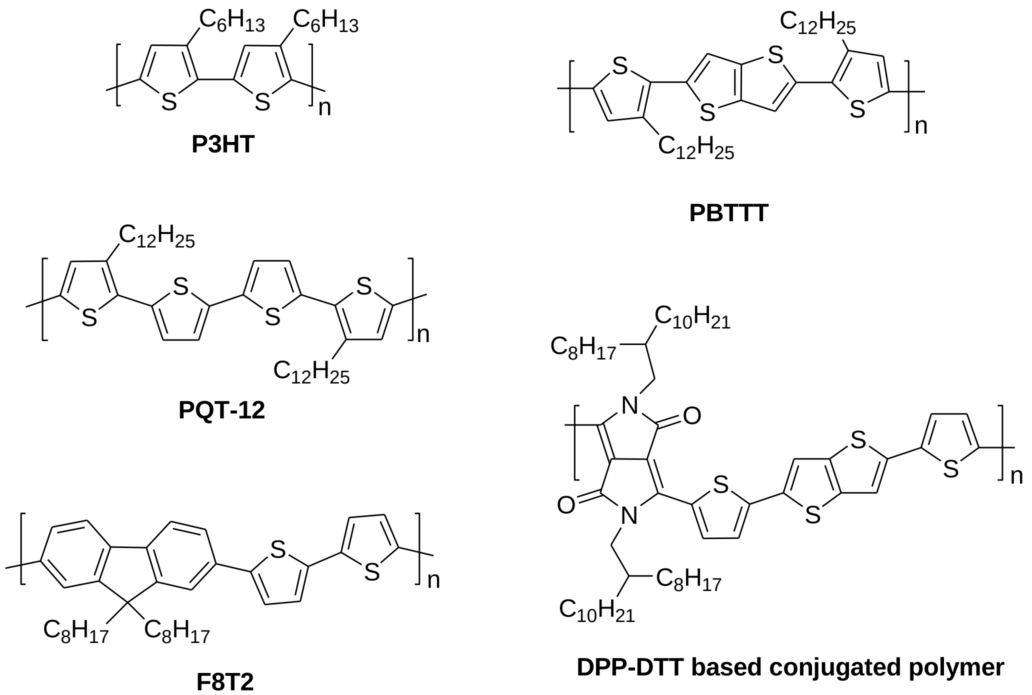

P3HT

PBTTT

PQT-12

F8T2

DPP-DTT based conjugated polymer

Fig. 2-5 Molecular structure of *p*-type polymer organic semiconductors

A problem associated with using electron-rich thiophene-based organic semiconductor is their sensitivity to atmospheric doping, which diminishes the on/off ratio and alters the threshold voltage. A strategy to decrease the environmental sensitivity is to reduce the energy of the HOMO. Poly(3,3'''-didedocyl-quaterthiophene) (PQT-12) OFETs, which were fabricated by spin coating from a hot dichlorobenzene solution under ambient conditions, feature an average mobility of 0.1 cm^2/Vs with an I_{on}/I_{off} of 10^7. This ability to achieve high mobility and high I_{on}/I_{off} in air is attributed to its good environmental stability, owing to reduced HOMO levels due to the unsubstituted thiophene affording rotational freedom along the backbone [56, 57].

In Chapter 3, we synthesize a novel *p*-type organic semiconductor by replacing thiophene moieties in PQT-12 by selenophene moieties to achieve good optical and electrical properties.

Poly(9,9'-dioctylfluorene-co-bithiophene) (F8T2) [58] is another environmentally stable, promising polymer semiconductor that is extensively explored in OFETs. Poly(2,5-bis(3-alkylthiophen-2-yl)thieno[3,2-*b*]thiophene) (PBTTT) [59-64] with fused aromatic units features reduced delocalization along the backbone, which subsequently results in a low lying HOMO level for high-mobility OFETs. As delineated earlier, a solution-processable polymer semiconductor that features stronger donor groups of dithienylthieno [3,2-b]thiophene (DTT) and weaker acceptor groups of N-alkyl diketopyrrolo-pyrrole (DPP) via D-A molecular structure achieves the highest hole mobility OFETs [65]. This stable solution-processed DPP-DTT-based polymer semiconductor for PE exhibits a drain current of the order of mA and a high transistor mobility over 10 cm^2/Vs. Table 2-1 summarizes the basic performance of OFETs made from the above reported materials.

Table 2-1 Basic parameters of OFETs based on *p*-type polymer semiconductors

Semiconductor	**μ (cm^2/Vs)**	**HOMO (eV)**	**I_{on}/I_{off}**	**Solvent**
P3HT [54]	0.10	-4.9	10^6	Chloroform
PQT-12 [56]	0.14	-5.0	10^7	Chlorobenzene
F8T2 [58]	0.015	-5.8	10^6	Xylene
PBTTT [59]	0.70	-5.1	10^6	Dichlorobenzene
PDBT-co-TT [66]	0.94	-5.2	10^6	Chloroform
DPP-DTT-based Polymer [65]	10	-5.2	10^6	Chlorobenzene

In summary, the molecular structure of the *p*-type organic semiconductors is fundamental to determine molecular ordering in solid film. Appropriately adjusted semiconductor morphology is mandatory, because a strong π-π overlap in the current direction is required to ensure efficient intermolecular charge carrier transport without substantial amount of electron traps in the transistor channel. In addition, the solvent properties, casting methods, annealing conditions in *p*-type OFETs fabrication also greatly influence the film growth and morphology, and accordingly the charge transport properties. In short, improvement in the device performance can be achieved by optimizing the semiconductor morphology through improved process parameters or adequate choice of gate dielectric. This is the approach we adopt in Chapters 3, 4 and 5 for our OFETs fabrication.

2.5 *n*-type organic semiconductors

Compared with the widely available *p*-type organic semiconductors, *n*-type organic semiconductors are substantially inferior in performance. One reason for this is that the work function of the metal electrodes, such as Au and Ag, is more appropriate for hole injections into the HOMO level of the typical organic semiconductors. Metal electrodes with a low work function, such as Al and Mg, are expected to achieve electrons injections, but they oxidize easily and readily form reactive moieties in the organic semiconductors.

The typical organic semiconductors of unsubstituted oligothiophenes and oligoacenes have low electron affinity (EA) [67], for instance for that of pentacene is low at 2.8 eV. The methodology to achieve *n*-type organic semiconductors is to incorporate electron-withdrawing groups, such as -F and -CN, to increase the EA, thereby allowing electron injection from metal electrodes with high work function such as Au. By doing so, the environmental stability of the *n*-type organic semiconductors may be improved. It is worthwhile to note that, to improve good electron injection from the electrode into the LUMO level of these *n*-type organic semiconductors, the work function engineered by self-assembled layer is needed.

The chemical structures of several typical *n*-type semiconductors are depicted in Fig. 2-6. Alternatively, organic compounds, such as C_{60}, PCBM, perylene-bis(dicarboximide) (PDI) [68, 69] or naphthalene-bis(dicarboximide) (NDI) [70, 71] that have strong electron-withdrawing groups and provide low lying LUMO levels, feature good *n*-type field-effect behaviour and environmental stability [72]. Compared to PDI monomers, the NDI core has attracted much interest within the PE community because of its stronger electron-deficient structure and highly π-conjugated microstructure. Recently, a high-mobility *n*-type NDI-based polymer semiconductor P(NDI2OD-T2) was reported [73] to exhibit good air-stability, process versatility and device performance, and is widely explored in the complementary circuits. Other factors to be considered for the design of *n*-type organic semiconductors include sufficiently high electron affinity (in the range of 3.0 to 4.0 eV) [74-76], low bandgap [77], good intermolecular electronic overlap, good film-forming properties, high purity [26], and air-stability, etc. In general, the performance of *n*-type semiconductors remains substantially inferior to *p*-type semiconductors and it is hence not unexpected that *p*-type semiconductors are dominant.

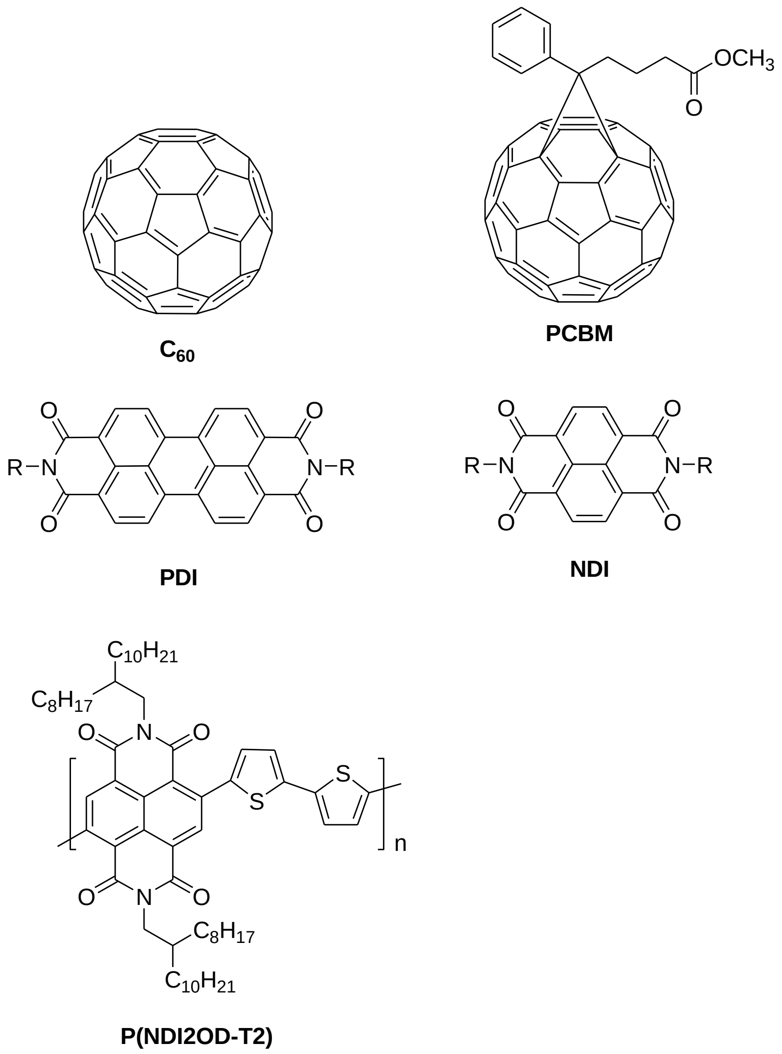

C60

PCBM

PDI

NDI

P(NDI2OD-T2)

Fig. 2-6 Molecular structure of *n*-type organic semiconductors

2.6 Gate dielectrics for OFETs

In PE, the active semiconductor and dielectric layer cannot be considered independently. In transistor devices, the dielectric is an electronic insulator to allow the carrier accumulation in the semiconductor. The insulator plays a central role in the charge transport in the transistor channel because the majority of charge carriers flows in the immediate vicinity (< 1 nm) of the insulator/organic interface and the charge transport occurs in the organic semiconductor along the semiconductor/insulator interface [41]. The gate dielectric affects the electrical characteristics of OFETs largely by its influence on the morphology of the organic semiconductor, by its dielectric properties, and by electronic states existing at the dielectric surface. Apart from the optimization of the mobility of carriers, the reduction of traps at the interface of semiconductor/dielectric is crucial to achieve stable and high-performance OFETs.

The capacitance of the gate dielectric per unit area is expressed in the equation 2.4:

$$C = \varepsilon_0 \, k/d \tag{2.4}$$

where k is the dielectric constant,

ε_0 is the vacuum permittivity, and

d is the insulator thickness.

For a given device geometry and semiconductor, and bias condition, the drain current I_D is proportional to C. Consequently, high capacitance is an important parameter for efficient device scalability, and a prerequisite to achieve high frequency and obtain low-power operation of OFETs. In general, the capacitance of the gate dielectric per unit area should be increased either by using high-k dielectric or by decreasing the dielectric layer thickness.

2.6.1 Inorganic dielectrics

Thermally grown SiO_2 on doped Si substrate is often explored as the gate dielectric for most silicon-based OFETs devices [72]. There are hydroxyl groups in the form of silanols on the surface of SiO_2, which cause charge trapping at the interface of semiconductor/dielectric, and this is depicted in Fig. 2-7. These hydroxyl groups act as electron traps hindering efficient electron transport, especially for *n*-type OFETs. It is hence necessary to treat the surface using octadecyltrichlorosilane (OTS) [78], hexadimethyldisilazane (HMDS) [79-81], or oxygen-plasma pre-treatment of SiO_2 [82, 83], etc. In addition, the sol-gel silica gate dielectric is employed to endow organic semiconductors with better molecular ordering/packing and to reduce charge trapping centers in the dielectric layer, which is better than OTS-thermally grown silica [84-86].

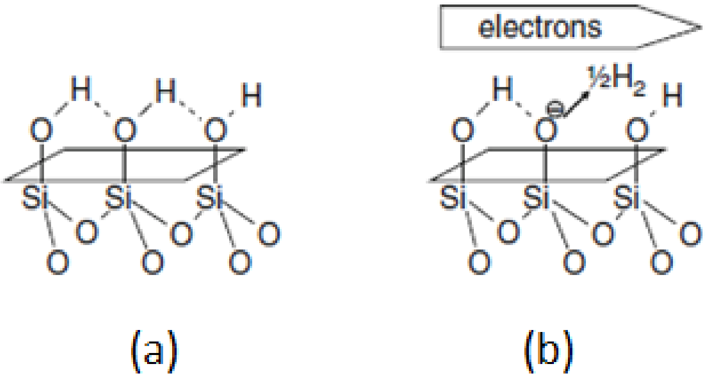

Fig. 2-7 (a) The hydroxyl groups terminating the SiO_2 surface; and (b) Proposed mechanism of electron trapping [72]

2.6.2 Polymer dielectrics

In PE, the gate dielectric materials must meet the requirements of low processing temperature, good compatibility with the flexible substrate and organic semiconductors. These requirements limit the choice of dielectric materials commonly used for silicon-based electronics. To this end, it is prudent to explore printable dielectric materials, such as hybrid dielectrics, ion-gels [26, 87-89], and self-assembled dielectrics [90], etc.

Among them, polymer gate dielectrics exhibit great potential for OFETs fabrication due to their excellent film-forming and good mechanical properties, and easy deposition from solution by spin coating, casting, or printing methods. These features correspond to great advantages of low-cost patterning techniques for dielectric materials and facilitate the deposition of other materials in the device fabrication. For fully-additive printed transistor devices, the polymer gate dielectric should also feature good compatibility with the flexible substrate and printability or solution processability. In order to avoid damage from subsequent semiconductor deposition from organic solvents, orthogonal solvent systems can be used for each layer during the deposition process [91]. Moreover, hydroxyl-free poly(methyl methacrylate) (PMMA) is usually used as the polymer gate dielectric and can be easily deposited onto large areas by spin coating and cured at temperatures of about 170 °C.

However, the resulting OFETs using PMMA as the gate dielectric operate at relatively high voltages, and the curing temperature is excessively high for the used plastic substrate in PE. Recently, cross-linked polymer gate dielectrics have attracted much interest due to their favorable insulating properties. Cross-linked PMMA (c-PMMA) exhibits unique properties, and yields robust, smooth, adherent, pinhole-free, high-capacitance, and low-leakage ultrathin layers [92, 93]. The very thin dielectric film (< 20 nm) features a low leakage current density (~10^{-8} A/cm^2) and a large *k*/*d* ratio, and achieves low-operating-voltage device (<5 V). Furthermore, the crosslinking dielectric layer is advantageous because it typically remains undissolved or undamaged from the subsequent semiconductor depositions by spin coating or printing methods. Fig. 2-8 shows the mechanism of crosslinking reaction to c-PMMA dielectric mateirals.

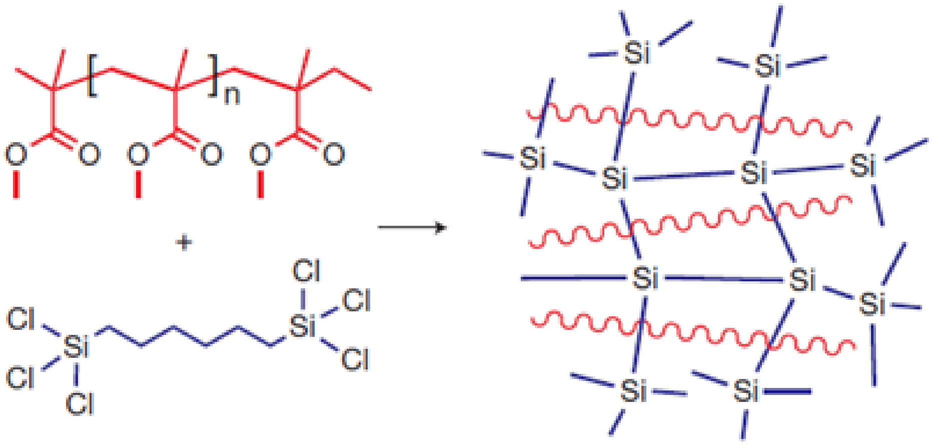

Fig. 2-8 Physical cross-linked network of c-PMMA [92]

As depicted in Section 2.3, one way to obtain balanced electron and hole mobility is to eliminate the electron traps in the dielectric layer. It is well known that the hydroxyl groups in the surface of polymer dielectric layer suppress electron transport in devices, which is unfavorable for the device performance of the *n*-type organic semiconductors. Recently, a robust cross-linkable, low-surface-energy hydroxyl-free gate dielectric divinyltetramethylsiloxane-bis(benzocyclobutene) (BCB) derivative has been reported [94, 95], where it provides a high-quality hydroxyl-free interface for the organic semiconductor/dielectric.

With regard to *p*-type OFETs with a very high mobility of 10 cm^2/Vs, a bilayer gate dielectric with a top layer of cross-linked polymethylsilsesquioxane (PMSQ) and a bottom layer of polyacrylonitrile (PAN) was reportedly [65] deposited by spin coating for the device fabrication on a flexible PET substrate. Cross-linked PMSQ prevents potential solvent attack of the subsequent semiconductor deposition and also provides a hydroxyl-functionalized surface for OTS surface treatment. The bottom dielectric layer of PAN is used due to its high dielectric constant, low leakage current density and good solution processability. Fig. 2-9 depicts the synthesis of the cross-linked PMSQ as the top dielectric layer.

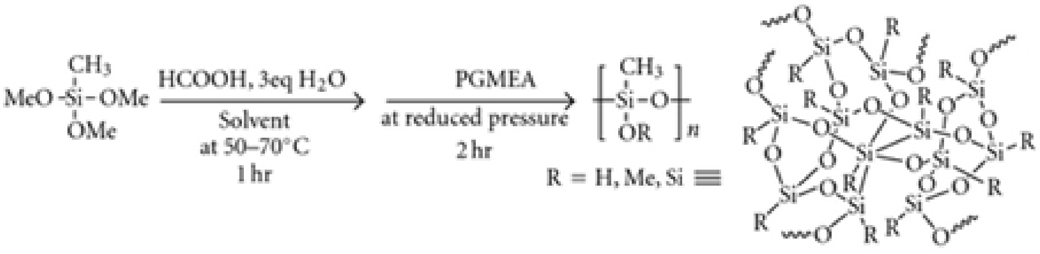

Fig. 2-9 Synthesis of PMSQ [65]

It is noteworthy that the advanced Fully-Additive process has been reported by our NTU research group, where UV cross-linked dielectric materials have been explored for OFETs in PE [15]. Moreover, the results obtained from the bilayer dielectric in Chapter 5 provide important information for printable dielectric ink formulation.

2.6.3   Polymer nanocomposite dielectrics

Printable nanocomposite materials have great potential applications in microelectronics [96], such as adhesives, interlayer dielectrics, embedded passives, and circuits, etc. Polymer nanocomposite dielectrics using nanoparticles as ceramic fillers provide a potential solution to meet present and future technological demands in terms of good processability and mechanical properties of polymers combined with the unique electrical, magnetic, or dielectric properties of nanoparticles. In addition, nanosized particles are preferred for high-*k* dielectric composite materials because thinner dielectric films can be fabricated. High-*k* polymer nanocomposite materials have been widely reported by the introduction of nanoparticles such as TiO_2 [97], $BaTiO_3$ [98-100] and $SrTiO_3$ [101], etc. The polymer matrices include polyvinylidenefluoride (PVDF)-based fluoropolymers, thermosetting polymers epoxy resin [96, 102-106] and polyimide (PI) [107], and thermoplastic PMMA [108, 109], etc.

On one hand, thermosetting resins-based polymer nanocomposites have been widely reported to achieve high-capacitance dielectric materials for PE, and they are advantageous in terms of manufacturability, low processing temperatures, low moisture absorption and high thermal stability. A reported epoxy/$BaTiO_3$ nanocomposite dielectric [102] features a capacitance in excess of 6 nF/cm^2 and a high dielectric constant of 35. A reported polytriarylamine (PTAA)-based OFETs using this nanocomposite dielectric feature a mobility of 1.2×10^{-4} cm^2/Vs, having an I_{on}/I_{off} of 10^3 with a V_T of 4 V.

On the other hand, thermoplastic PMMA hybrid dielectrics with $BaTiO_3$ can be prepared by in situ polymerization to achieve a combination of high dielectric constant and low dielectric loss for the electronic application. $BaTiO_3$ hybrid PMMA dielectric inks [110] have been reportedly deposited by gravure printing, having a dielectric constant of 13 and an average capacitance of 5 nF/cm^2.

In this PhD work, screen-printable dielectric inks based on a polymer nanocomposite have successfully been formulated for Fully-Additive printed OFETs. These will be delineated in Chapters 4 and 5 later.

2.7 Printing methods for transistors and circuits

OFETs, as the elementary electronic driving devices, can be fabricated by printing methods based on low cost processing. Table 2-2 tabulates a comparison of the reported present-day fully-additive printing technologies. The different printing techniques require different solution concentrations, ranging from highly viscous ink formulations used in flexography to more diluted inks for inkjet printing. Since the key objective of this PhD work is to apply printing methods instead of spin coating to fabricate OFET devices, there is a detailed account of the screen printing method and the slot-die coating in terms of the operating principle, advantages and the limitations of these methods.

Table 2-2 Basic parameters of common fully-additive printing technologies [16]

Printing method	**Thickness (μm)**	**Resolution (μm)**	**Viscosity (Pa.s)**	**Speed (m/min)**
Flexo	0.5-2	20-50	0.05-0.5	50-80
Gravure	0.5-2	20-50	0.05-0.2	20-100
Offset	0.5-2	15	30-100	15-100
Screen	5-25	80-100	0.5-50	10-100
Inkjet	100-500	20	0.002-0.025	n.a.

Screen printing

Screen printing is a well-established and relatively simple printing method that has been used for extensively printing T-shirts (graphic art) and printed circuits boards. Fig. 2-10 depicts screen printing process. The image is defined through an opaque mask, which is applied to a fine mesh material. The non-imaging areas are concealed by a stencil. The ink is spread over the screen with an elastic squeegee. The squeegee forces the ink through the meshes onto the substrate in the non-masked areas.

Screen printing in general is very suitable, when relatively thick and homogeneous films are required and significant volume can be achieved through rotary screen printing. Screen printing inks are viscous (0.5-50 Pa.s) and allow thick ink films (varying from 5-25μm). Inks may be dried through solvent evaporation or by UV curing. However, screen printing has the primary limitations of relatively large feature size (approximately 100 μm), and the high viscosity of available inks (difficulty of processing).

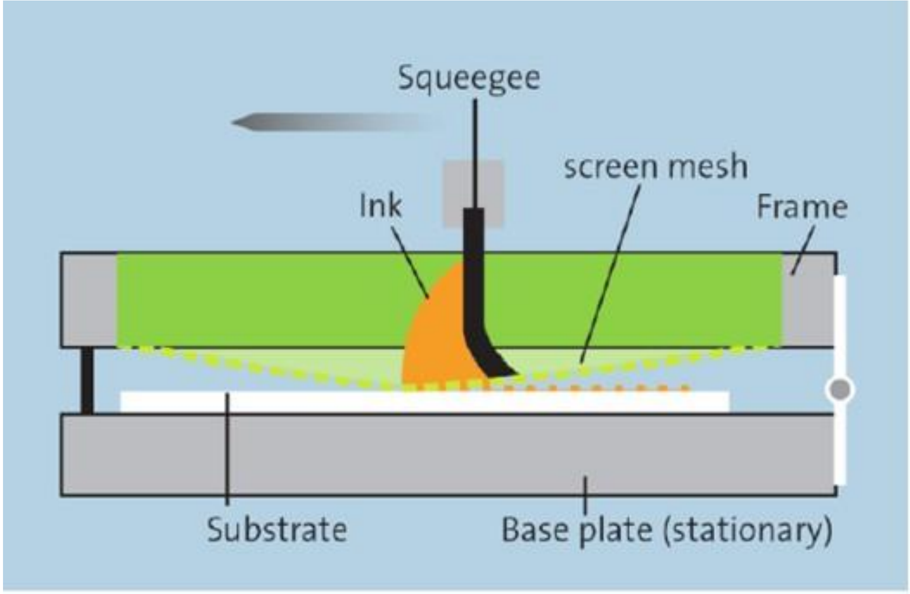

Fig. 2-10 Screen printing process [17]

The screen printing method is, arguably, the simplest and cheapest fully-additive process to deposit the electrodes and dielectrics layers in PE. It is reported that an OFET-backplane [111] has been fabricated by screen printing for its gate electrodes and inkjet printing for TIPs-pentacene semiconductor, and features an OFETs mobility of 0.3 cm^2/Vs. Screen-printed top-gate OFETs [112] based on *p*-type organic semiconductor TIPs-pentacene and *n*-type organic semiconductor exhibit hole and electron mobilities of 0.5 cm^2/Vs and 1.5 cm^2/Vs respectively. Moreover, it was reported [113] that a highly hydrophobic fluoropolymer dielectric poly(perfluorobutenylvinylether) (CYTOP) deposited by screen printing exhibits little gate bias stress effects and a very low electron trap density.

Slot die coating

Slot die coating is by far the most widely used roll-to-roll processing technique for OPVs. Fig. 2-11 depicts the slot die coating process where the ink is fed to the coating head via a pump/pressure system, and thereafter deposited to the substrate at the certain speed and direction. The use of the slot die coater is proposed to print the TIPs-pentacene semiconductor layer instead of the reported inkjet, spin coating, drop casting, etc.

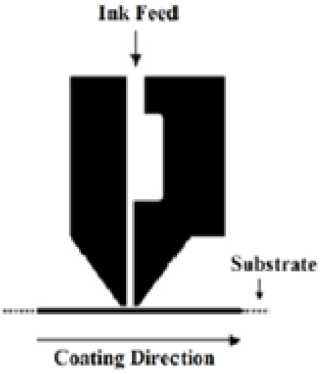

Fig. 2-11 Slot die coating process

The advantage of using a slot die coater is that the crystal formation of the TIPs-pentacene is well controlled so that the crystal grain boundaries are decreased, thereby facilitating the flow of electrons between the source and drain of the transistor. Fig. 2-

12 depicts the semiconductor crystal orientation effect of the coating direction. The coating direction across the channel will yield a substantially higher mobility as the holes will cross less grain boundaries whist transporting from source to drain. On the basis of measurement, the mobility of (a) and (b) is 0.1 cm^2/Vs and 1.5 cm^2/Vs, respectively.

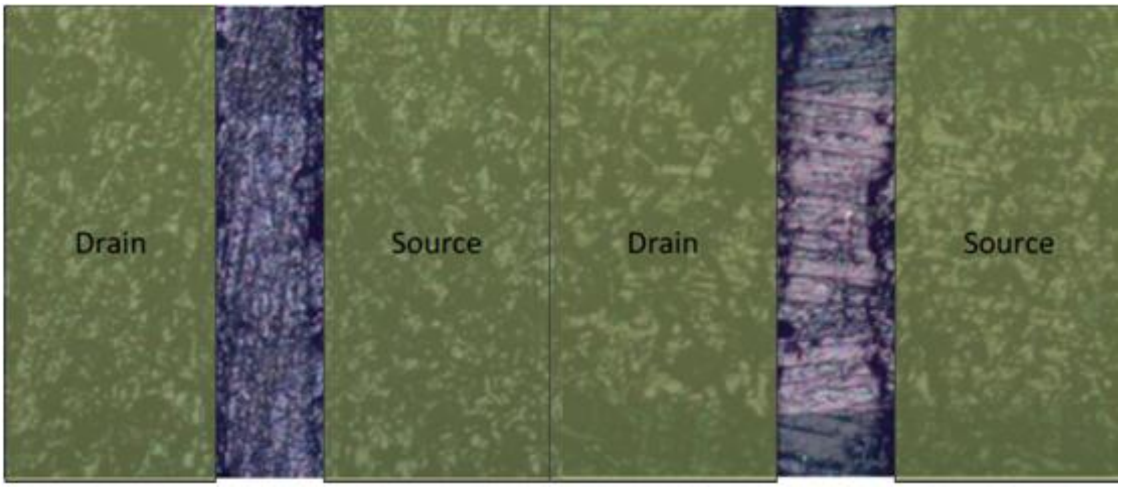

(a) (b)

Fig. 2-12 Crystal formation with coating direction of (a) Follow; and (b) Across channel

As delineated earlier, the advanced Fully-Additive process has been reported by NTU research group [15], where the author of this thesis is associated with, involves the screen printing and slot die coating methods. In this process, the bottom-gate bottom-contact OFETs are fabricated on flexible substrates by screen printing, and TIPs-pentacene as the organic semiconductor is deposited by slot die coating. The hole mobility is 1.5 cm^2/Vs - to the best of the author's knowledge, the highest carrier mobility of all Fully-Additive processes to date [15], and comparable to the substantially more complex and expensive Subtractive-based processes. Table 2-3 tabulates reported fully-additive printed OFETs and circuits with details of materials and printing processing. Some of these reported processes will now be briefly described in turn.

Table 2-3 Fully-Additive printed circuits (and systems)

Device	**Gate**		**Dielectric**		**Semiconductor**		**Source/Drain**		**Circuits and Systems**
	Material	**Deposition Method**	**Material**	**Deposition Method**	**Material**	**Deposition Method**	**Material**	**Deposition Method**	
Bottom gate PMOS [15]	Silver	Screen	UV curable dielectric	Screen	TIPs-pentacene	Slot die coating	Silver	Screen	Amplifier and DAC
Bottom gate PMOS [114]	Silver	Inkjet	PVP	Inkjet	TIPs-pentacene	Inkjet	Silver	Inkjet	Inverter
Bottom gate PMOS [115]	Silver	Flexo	Butadiene-Styrene copolymer	Gravure; Flexo	F8T2	Gravure	PEDOT: PSS	Offset	7-stage Ring Oscillator
Top gate PMOS [116]	Clevios P	Flexo	Butylenes copolymer PMMA	Gravure	F8T2	Gravure	PEDOT: PSS	Flexo; Gravure	5-stage Ring Oscillator
Top gate OFETs [27]	Silver	Gravure	$BaTiO_3$ Hybrid PMMA	Gravure	Surface modified SWCN	Gravure	SWCN	Gravure	n.a.
Antenna Diode Capacitor Resistor Bottom gate PMOS [110]	Silver	Gravure	$BaTiO_3$ Hybrid PMMA	Gravure	Surface modified SWCN	Gravure	SWCN	Inkjet	1-bit RFID Tag

Fully printed circuits

It was reported [136] that all-inkjet-printed single transistor and inverter using *p*-type OFETs have been fabricated on a flexible plastic substrate. All the layers were deposited by inkjet printing, with PVP as the gate dielectric, and TIPs-pentacene as the active semiconductor. The single OFET features a low mobility of 0.02 cm^2/Vs with an I_{on}/I_{off} of 10^4. The device variations in terms of TIPs-pentacene OFETs mobility are large due to the difficulty in controlling crystal growth when deposited from solution. In order to improve the mobility of TIPs-pentacene with deposition by inkjet printing, a mixture of small molecules with amorphous polycarbonate (PC) was explored as the active semiconductor. The PC as the polymer binder can induce good phase separation from the crystal phase of TIPs-pentacene. OFETs based on the blend of PC and TIPs-pentacene with a weight ratio of 1:4 in the mixed solvent of toluene/p-xylene exhibit a relatively high average-mobility of 0.53 cm^2/Vs.

The gravure printing additive process [115, 116] is also widely explored within the PE community. More recently, carbon nanotube FETs are particularly interesting [27] where Fully-printed, high-performance carbon nanotube thin-film transistors with a top-gated device geometry were fabricated by inverse gravure printing on flexible substrates. The top-gated transistor with 99% semiconductor-enriched nanotubes exhibits a very high hole mobility of 9.0 cm^2/Vs - probably is the highest mobility value of among fully-printed nanotube transistors in the low temperature solution-processed devices. The multistep layers of source and drain electrodes, the dielectric layer, and gate electrodes were also deposited by inverse gravure printing. The PMMA/$BaTiO_3$ hybrid dielectric ink has a high average capacitance of 10.8 nF/cm^2, and a high dielectric constant of 17.

The inverse gravure printing is an additive process appropriate for roll-to-roll process for high throughput and large area device processing. It was reported [110] that an all-printed and roll-to-roll-printable 13.56-MHz-operated 1-bit RF tag was fabricated on plastic foils. The single wall carbon nanotube (SWCNT) semiconductor, $BaTiO_3$ hybrid PMMA dielectric and electrodes were deposited by gravure printing. The fully-additive printed SWCNT OFETs featured a high mobility of 5.24 cm^2/Vs with a low (largely unacceptable) I_{on}/I_{off} of 100, but sufficient to operate 1-bit RF tags at a low switching speed of 100 Hz.

To sum up, based on the reported work for the 'Materials' and 'Process' supply chain, Fully-Additive PE can realize relatively complicated digital and analog circuits. In this study, screen printing is arguably the most promising for realizing complex circuits and systems, and this will be delineated in Chapters 4 and 5.

2.8 The operating principle of OPVs

Organic solar cells are devices that absorb light and convert it into electricity. To date, the most widely utilized device structure of an organic solar cell involves the concept of the bulk heterojunction (BHJ) [46], where the blend of donor and acceptor materials is sandwiched between indium tin oxide (ITO) and a metal electrode. Fig. 2-13 shows the simplified operation principles OPV. When photons from the sun are absorbed in the active layer, the donor is excited to create excitons (electron-hole pairs), which do not directly and quantitatively lead to free charge carriers. The excitons diffuse to the donor-acceptor interface and intramolecular charge transfers (ICT) occur from the donor to the acceptor. Fast dissociation takes place and excitons split to free charge carriers. The separated free electrons and holes will finally be transported to the electrodes due to the built-in electric field. This internal electrical field determines the open circuit voltage (V_{oc}) of a device and contributes to a field-induced drift of charge carriers.

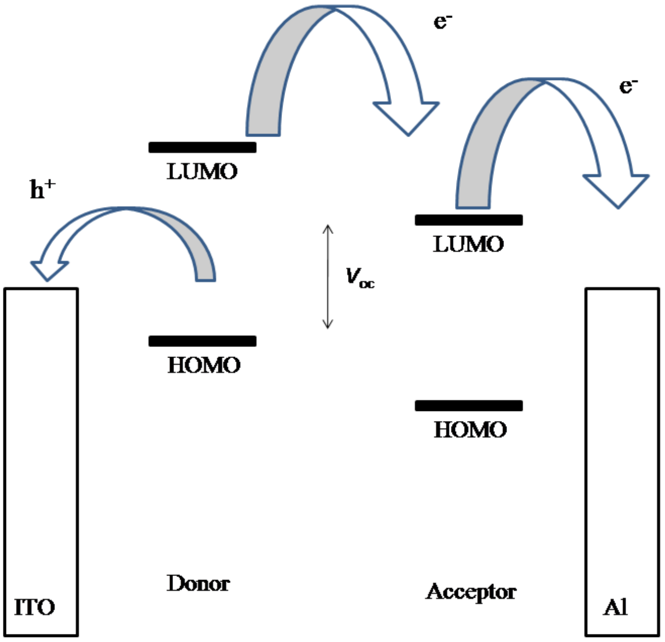

Fig. 2-13 Scheme of operation principle in OPVs

2.9 The electrical characteristics of OPVs

The power conversion efficiency (PCE) η of the organic solar cell [117] is determined by the electrical parameters including open-circuit voltage (V_{oc}), short-circuit current density (J_{sc}) and fill factor (FF). Fig. 2-14 depicts the I-V curves of OPVs in dark and under illumination conditions.

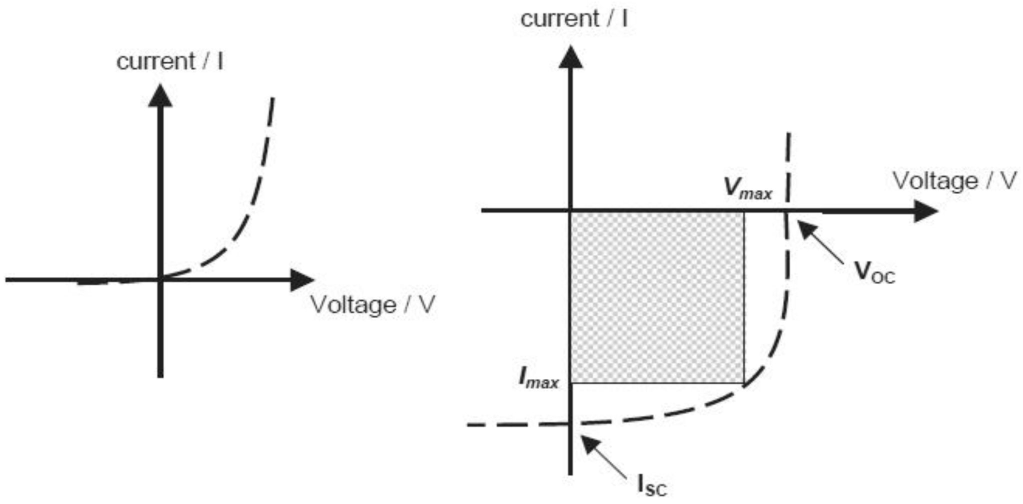

Fig. 2-14 *I-V* curves of OPV in dark (left) and under illumination (right)

In the dark, a reverse bias produces very little or negligible current. A forward bias larger than V_{oc} will produce an undesirably large current. Under illumination, the current flows in the opposite direction from the injected currents. V_{oc} and J_{sc} are illustrated in the *I-V* curve in Fig. 2-14 under illumination, and are determined from the intersections of the abscissa and the ordinate respectively. η is defined as the ratio of maximum power output (P_{out}) to power input (P_{in}), which can be expressed in the equation 2.5 [118].

$$\eta = \frac{P_{\text{out}}}{P_{\text{in}}} = \frac{V_{oc}J_{sc}FF}{P_{in}} \qquad (2.5)$$

where V_{oc} is open-circuit voltage,

J_{sc} is short-circuit current density,

FF is fill factor,

P_{out} is maximum power output, and

P_{in} is the incident light power which is standardized as 100 mW/cm^2.

2.10 Materials in OPVs

In BHJ OPVs, the donor and acceptor molecules are blended and co-deposited, giving rise to large interface between donor and acceptor. The *p*-type organic semiconductor as the donor in BHJ OPVs should possess a relative low optical bandgap to feature broad absorption in the solar spectrum, a low lying HOMO level to obtain a high V_{oc}, a large LUMO levels offset between donor and acceptor to achieve efficient charge separation, good mobility for efficient charge transport, and good solubility for solution processing [119]. One of the requirements for the *n*-type semiconductor as an acceptor is strong electron affinity to capture the electrons from the donor molecule. In order to improve the efficiency, the morphology of the active semiconductor layer must be well controlled and optimized by choosing proper casting solvent, deposition method, and annealing, etc.

In Chapter 3, promising donor and acceptor materials will be explored for application to BHJ OPVs.

2.11 Conclusions

The operating principles and essential parameters of OFETs, charge transport mechanism, development of materials (including *p*-type, *n*-type organic semiconductors and gate dielectric materials) and printing methods have been reviewed. As the charge transport occurs in the organic semiconductor along the interface of semiconductor and dielectric, OFETs characteristics are co-determined by the intrinsic molecular structure and microstructure of organic semiconductor, the morphology of organic semiconductors on the dielectric layer, and the contact barrier between metal electrodes and semiconductors, etc. To obtain good performance PE, the first chain of the PE supply chain, 'Materials', and the second chain thereof, 'Processing', must be collectively considered (or co-designed). These will be delineated in the following Chapters 4 and 5.

Moreover, the operating principle, the electrical characteristics and materials of OPVs have been reviewed. The results of OPVs device based on the synthesized materials will be delineated in Chapter 3.

Chapter 3 Synthesis and Characterization of Organic Semiconductors

3.1 Introduction

This chapter delineates the author's research work pertaining to the synthesis and characterization of a *p*-type organic semiconductor for OPVs. A large part of this chapter is extracted from the author's publication [35] in the Solar Energy Materials & Solar Cells journal.

Conjugated polymers [120] have attracted much interest in the fabrication of PE, and polythiophene is one of the most promising materials amongst them. In particular, regioregular poly(3-hexylthiophene) (P3HT) was commonly explored as an active semiconductor in organic field-effect transistors (OFETs) [121] and as a donor material in the bulk heterojunction organic photovoltaics (BHJ OPVs) [122], because of its beneficial properties such as a high hole mobility (0.1 cm^2/Vs). Although the mobility of 0.1 cm^2/Vs has been achieved in P3HT with special processing condition, in most literatures, the mobility of P3HT is ca. 100 times lower [121]. Another thiophene-based poly (3,3'''-didodecylquaterthiophene) (PQT-12) [56], with the unsubstituted thiophene affording rotational freedom along the backbone, exhibited a hole mobility of 0.18 cm^2/Vs nearly two times that of P3HT and had a particular advantage of the oxidative stability due to its larger ionization potential. As delineated in Chapter 2, organic semiconductor materials with a low bandgap should be required for trap-free high-mobility transport of both electrons and holes. Recently, oligoselenophenes [123], regioregular poly(3-hexyl)selenophene [124], and low bandgap selenophene-based conjugated polymers [125] were widely explored for efficient OPVs and OFETs. Compared to thiophene analogues, selenophene-containing polymers [126] featured larger and more polarizable selenium atoms, thereby exhibiting stronger intermolecular interaction of the polymers and affording improved optical and electrical properties.

In this chapter, a novel regioregular, selenophene and thiophene-based poly(2,5-bis(3-dodecylthiophen-2-yl)-2',2''-biselenophene) (PBTBS) was synthesized using $FeCl_3$ oxidative polymerization. The physical, optical, thermal, electrochemical properties, photovoltaic properties of PBTBS as a donor material for BHJ OPVs, and PBTBS-based OFETs characteristics were sufficiently investigated.

A novel solution-processable *n*-type organic semiconductor T3PT3 based on alkylthiophene/perylene-bis(dicarboximide) was also designed and synthesized via donor-acceptor (D-A) molecular structure. BHJ OPVs using T3PT3 as an electron acceptor and P3HT as an electron donor were fabricated to measure its photovoltaic properties.

3.2 *p*-type organic semiconductor of PBTBS

Regioregular, solution-processable PBTBS was synthesized by $FeCl_3$ oxidative polymerization, in which thiophene moieties were replaced with selenophene ones in the backbone of PQT-12, in an attempt to achieve good optical and electrochemical properties. The physical, optical, thermal and electrochemical properties of PBTBS as well as OFETs and OPVs characteristics based on PBTBS were investigated.

3.2.1 Experimental

^{1}H NMR spectra were recorded at 300 MHz, Bruker Advanced DPX 300. UV-vis absorption and photoluminescence (PL) spectra were recorded on a Shimadzu UV 3101 spectrophotometer and on a Perkin-Elmer LS-50B luminescence spectrometer, respectively. Differential scanning calorimetry (DSC) was performed under nitrogen atmosphere at a heating rate of 10 °C/min with TA 2920 analyzers. Cyclic voltammetry (CV) measurements were conducted on a three-electrode workstation in 0.1 M anhydrous acetonitrile solution of Bu_4NBF_4 at room temperature. Analytical thin layer chromatography (TLC) was performed using Merck 60 F_{254} precoated silica gel plate (0.2 mm thickness). Subsequent to elution, plates were visualized using UV radiation (254 nm). Flash chromatography was performed by using Merck silica gel 60 (230-400 mesh) with dried solvents. Columns were typically packed as slurry and equilibrated with the appropriate solvent system prior to use.

3.2.2 Synthesis of PBTBS

All commercial reagents and solvents were used without further purification unless otherwise stated. 2,2'-biselenophene [123], 5,5'-bis(tributylstannyl)-2,2'-biselenophene [124], and 2-bromo-3-dodecylthiophene [127] were synthesized according to reported methods.

2,2-bis(3-dodecylthiophen-2-yl)-2’,2’’-biselenophene (BTBS)

Add 5,5'-bis(tributylstannyl)-2,2'-biselenophene (2.6 g, 3.1 mmol), 2-bromo-3-dodecylthiophene (2.3 g, 7.0 mmol) and Pd_2dba_3/PPh_3 (46.8 mg/283 mg) into the mixed solvent of THF (3.5 mL) and DMF (3.5 mL). The mixture was ultrasonicated for 10 min, and subsequently reacted with refluxing at 95 °C under nitrogen for 2 days.

Extract the resultant solution by CH_2Cl_2 and evaporate the organic phase to get the crude product. Purify the crude product by silicon gel chromatography using hexane as eluent to get yellow solid (1.9 g, 80%). ^{1}H NMR (300 MHz, $CDCl_3$, δ): 7.21 (d, *J* = 3.9 Hz, 2H), 7.17 (d, *J* = 2.7 Hz, 2H), 7.15 (d, *J* = 1.2 Hz, 2H), 6.94 (d, *J* = 5.1 Hz, 2H), 2.78 (t, 4H), 1.65 (6H), 1.39 (30H), 0.95 (10H). ^{13}C NMR (300 MHz, $CDCl_3$, δ): 144.29, 140.07, 139.58, 132.82, 130.21, 128.56, 126.62, 123.81, 31.93, 30.69, 29.58, 29.47, 22.71, 14.14. Calcd for $C_{40}H_{58}S_2Se_2$: C, 63.14; H, 7.68; S, 8.43. Found: C, 62.36; H, 7.849; S, 8.39.

Poly (2,5-bis(3-dodecylthiophen-2-yl)-2',2''-biselenophene) (PBTBS)

Add the solution of 2,2-bis(3-dodecylthiophen-2-yl)-2',2"-biselenophene (500 mg, 0.6 mmol) in $CHCl_3$ (5 mL) dropwise into a well-stirred mixture of $FeCl_3$ (531 mg, 3.3 mmol) in $CHCl_3$ solution (10 mL) at 0 °C under nitrogen, which was subsequently warmed to RT to react overnight. Add $CHCl_3$ (15 mL) into the reaction resultant and pour into methanol (200 mL). The mixture was subsequently ultrasonicated for 20 min and stirred at RT for 1h. Filter the precipitated solid and transfer it to a mixture of methanol (200 mL) and aqueous ammonia solution (30 %, 50 mL), which was subsequently ultrasonicated for 5 min and stirred at RT for 3 days for dedoping. The crude solid was washed by methanol and hexane for 24 h sequentially, and finally extracted by chloroform through a Soxhlet apparatus. The polymer was precipitated into methanol to get purple solid residue (33%). ^{1}H NMR (300 MHz, $CDCl_3$, δ): 7.09, 6.92, 6.86, 2.65, 1.58, 1.19 and 0.80. ^{13}C NMR (300 MHz, $CDCl_3$, δ): 131.57, 129.52, 126.68, 30.93, 28.69, 28.36, 21.69, 13.11. Calcd for PBTBS: C, 63.94; H, 7.92; S, 8.13. Found: C, 60.68; H, 7.33; S, 7.39.

PBTBS was synthesized by $FeCl_3$ oxidative polymerization starting from 2,2-bis(3-dodecylthiophen-2-yl)-2',2''-biselenophene (BTBS). The synthetic routes of the monomers and the polymer are outlined in Scheme 3-1. When the concentration of $FeCl_3$ suspended chloroform solution increased from 0.3 M to 0.7 M, the yield of the polymer increased from 10% to 33%. The polymer is facilely soluble in common organic solvents, such as THF, $CHCl_3$ and 1,2-dichlorobenzene, without the tendency of gel formation under low temperature, thereby avoiding practical fabrication challenge faced by PQT-12 [128]. The number-average molecular weight (M_n) of PBTBS was 10,000 with a polydispersity of 2.4 determined by gel permeation chromatography (GPC) using THF as eluent and polystyrene as standard.

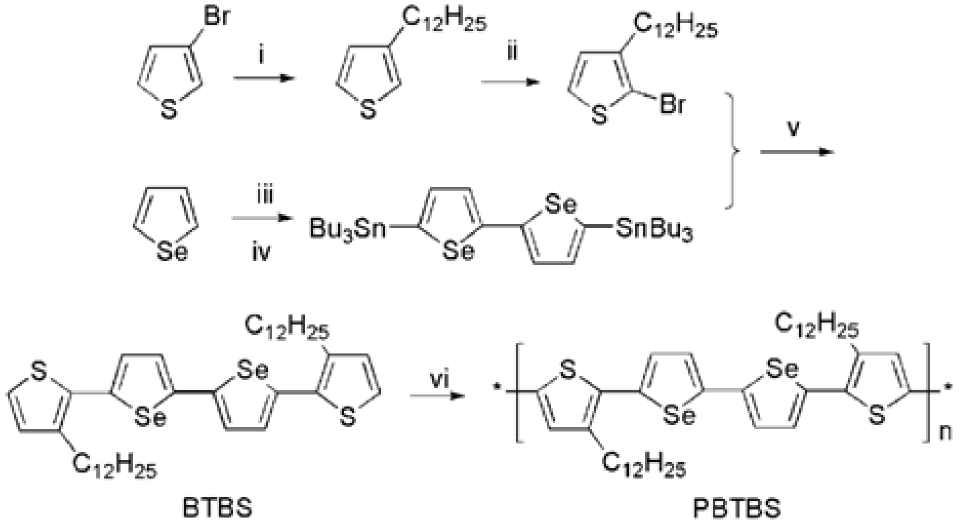

Scheme 3-1 Synthetic routes of PBTBS

(i) Mg, $C_{12}H_{25}Br$, $Ni(dppp)Cl_2$, dry ether; (ii) N-bromosuccinimide/DMF; (iii) *n*-BuLi, THF, -78 °C, $CuCl_2$; (iv) *n*-BuLi, THF, -78 °C, *n*-Bu_3SnCl; (v) Pd_2dba_3/PPh_3, THF/DMF; and (vi) $FeCl_3/CHCl_3$.

3.2.3 Optical properties of PBTBS

The optical properties of PBTBS were investigated by UV-visible (UV-vis) spectroscopy and by photoluminescence (PL) spectroscopy in the solution and the film state at RT. As depicted in Fig. 3-1, the maximum absorption of PBTBS in the thin film (λ_{max} = 558 nm) featured red shifts of 53 nm and 64 nm in comparison to that of PBTBS in the 1,2-dichlorobenzene (λ_{max} = 505 nm) and the $CHCl_3$ solution (λ_{max} = 494 nm), respectively. This red shift from the solution state to the film state was attributed to the stronger interchain interaction of the polymer in the film state. It was also observed that a pronounced shoulder peak appeared between 600 nm and 650 nm in the UV-vis spectra of PBTBS, due to the vibronic structures as in the case of P3HT film spectra [129].

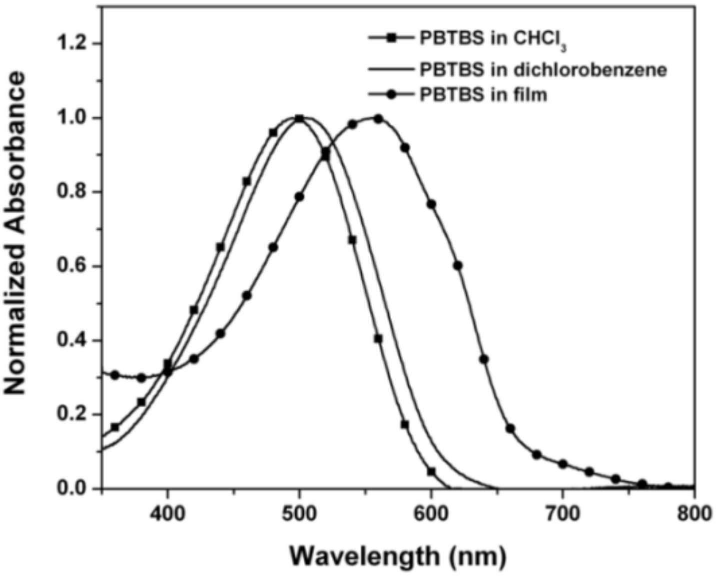

Fig. 3-1 UV-vis spectra of PBTBS in the solution and the film state

The maximum absorption of PBTBS in the dichlorobenzene solution exhibited a red shift of 24 nm in comparison to that of PQT-12 (λ_{max} = 481 nm) [56] in the dichlorobenzene solution, which arose from stronger electron-donating properties of selenophene than the thiophene analogue [124]. From the onset wavelength of the UV-vis spectra, the optical bandgap of PBTBS was 2.1 eV, slightly lower than that of PQT-12.

As depicted in Fig. 3-2, the PL spectra of PBTBS in the $CHCl_3$ and dichlorobenzene solutions (0.1 mg/ml) were obtained at the excitation of the maximum absorption of 494 nm and 505 nm, respectively. The PL spectra of PBTBS in these two solutions featured similar profiles with the maximum emission observed at 588 nm and 593 nm, respectively; shoulder peaks were observed in the range from 625 nm to 650 nm, which could be ascribed to the emission of aggregates in the dilute solutions [130].

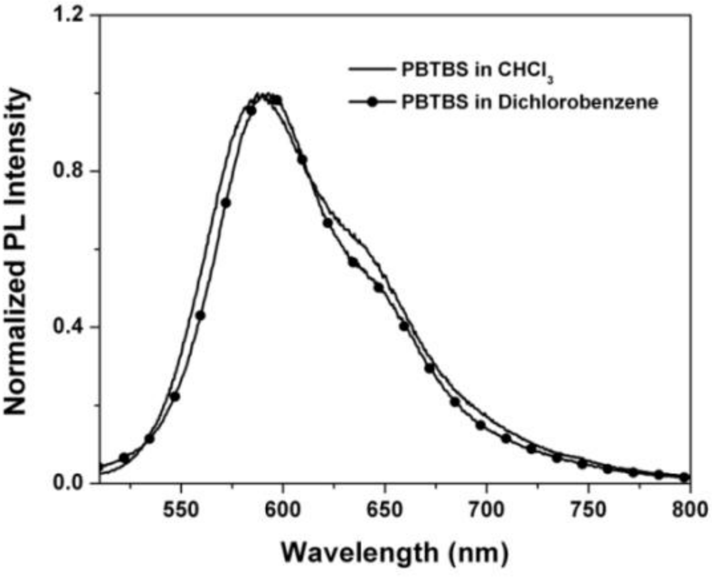

Fig. 3-2 PL spectra of PBTBS in the solutions

Moreover, in order to investigate PBTBS as a donor group in BHJ OPVs, PL spectra of the pristine PBTBS film and the blend PBTBS/PCBM film were measured at the excitation of 558 nm, which was the maximum absorption of PBTBS. Fig. 3-3 depicts the PL spectra of the pristine PBTBS film and the blend film of PBTBS/PCBM (1:1, wt%). The predominant PL emission peak of the pristine PBTBS was observed at ~650 nm, while the emission peak of the blend PBTBS/PCBM film was quenched to about 6% of that of the pristine PBTBS. It was indicated that the electron was transferred from the donor to the acceptor, which made it possible to fabricate BHJ OPVs using PBTBS/PCBM as the active semiconductor layer.

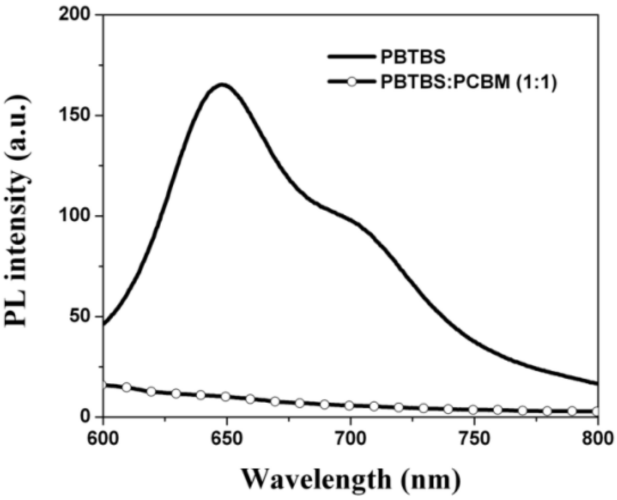

Fig. 3-3 PL spectra of the PBTBS film and PBTBS/PCBM blend film

3.2.4 Electrochemical properties of PBTBS

The electrochemical properties of PBTBS were measured by cyclic voltammetry (CV) and the CV curves was depicted in Fig. 3-4. These measurements were performed under nitrogen in anhydrous acetronitrile solution of 0.1 M Bu_4NBF_4. A glassy carbon disk coated with a thin polymer film was used as work electrode, with a silver wire as pseudo-reference electrode and a platinum wire as counter electrode. The redox potentials were calibrated using the ferrocene/ferrocenium (Fc/Fc$^+$) as reference (-4.8 eV vs. vacuum) [131]. It was observed that the oxidation (*p*-doping) of PBTBS showed excellent reversibility, and the polymer could be doped and dedoped repeatedly under inert atmosphere. With the onset of the oxidation potential of 0.7 V (2nd cycle), the HOMO level of PBTBS was calculated to be -5.04 eV, according to the following equation: ionization potential (IP) = $E_{\text{onset (ox)}} - E_{\text{FOC}} + 4.8$ ($E_{\text{FOC}} = 0.46$ V). Compared with the HOMO level of PQT (-5.2 eV), PBTBS showed a higher HOMO level and lower oxidative stability than PQT, which was attributable to its lower oxidation potential of the selenophene moiety than that of the thiophene analogue. With the onset of the reduction potential of -1.5 V, the LUMO level of PBTBS was calculated to be -2.84 eV, according to the following equation: electron affinity (EA) = $E_{\text{onset (red)}} - E_{\text{FOC}} + 4.8$. The difference of HOMO level and LUMO level is the electrical bandgap of 2.2 eV, which is comparable with the optical bandgap.

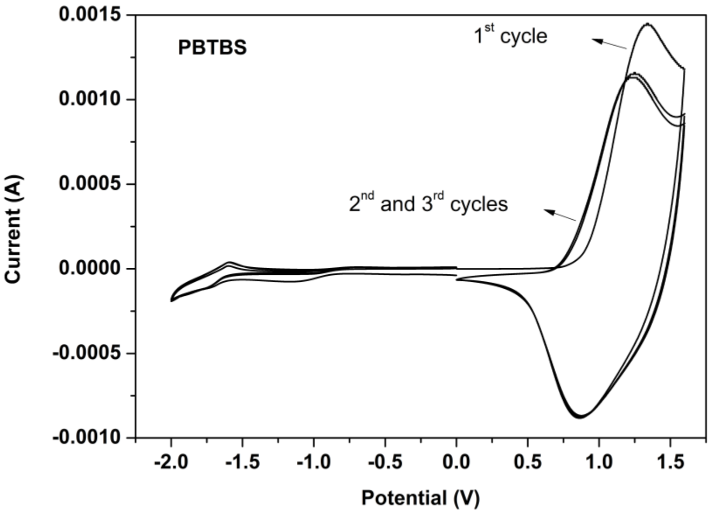

Fig. 3-4 Cyclic voltammogram of PBTBS film coated on a glass carbon electrode in

0.1 M Bu_4NBF_4/acetonitrile at scan rate of 100 mV/s (3 cycles)

Fig. 3-5 depicts the CV curves of the starting material of BTBS. With the onset of the oxidation potential of 0.9 V, the HOMO level of BTBS was calculated to be -5.1 eV, slightly lower than that of PBTBS. The oxidative doping of conjugated organic semiconductors depends on their IPs, i.e. their HOMO levels from vacuum. BTBS is expected to have better oxidative stability than PBTBS; however, as far as PE is concerned, the small molecule of BTBS deposited by vacuum evaporation has attracted less interest than the solution-processable polymer of PBTBS in this research.

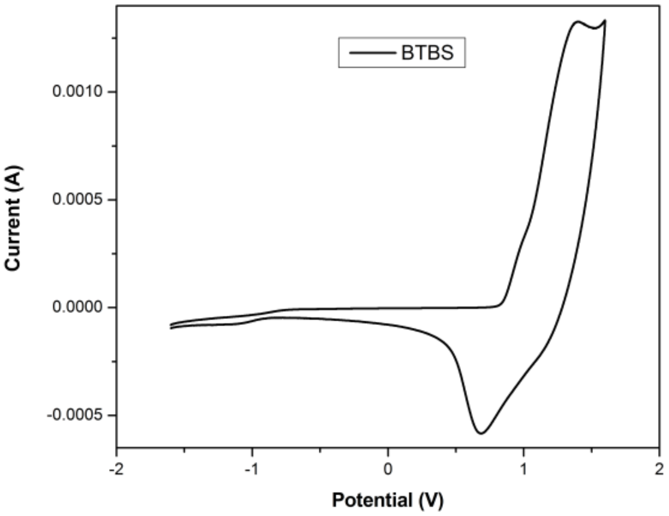

Fig. 3-5 Cyclic voltammogram of BTBS film coated on a glass carbon electrode in 0.1 M Bu_4NBF_4/acetonitrile at scan rate of 100 mV/s

3.2.5 Thermal and morphological properties of PBTBS

The thermal properties of PBTBS were evaluated by thermogravimetric analysis (TGA) and differential scanning calorimetry (DSC) under nitrogen atmosphere. As depicted in Fig. 3-6(a), there is an obvious one-step degradation arising from the cleavage of side chain groups for PBTBS with onset of degradation (a weight loss ~5%) observed at ~370 °C (decomposition temperature T_d). The incomplete decomposition of 37% at 500 °C in TGA curve under nitrogen was attributed to the main chain, whose degradation is generally observed in TGA measured in air. The color of the residue was gray.

Thermally induced phase transition behaviors of PBTBS were measured by DSC under nitrogen atmosphere at a heating rate of 10 °C/min depicted in Fig. 3-6(b). The glass transition temperature (T_g) of PBTBS was 84 °C. This thermal properties provide thermal annealing conditions for PBTBS in the ensuing device fabrication.

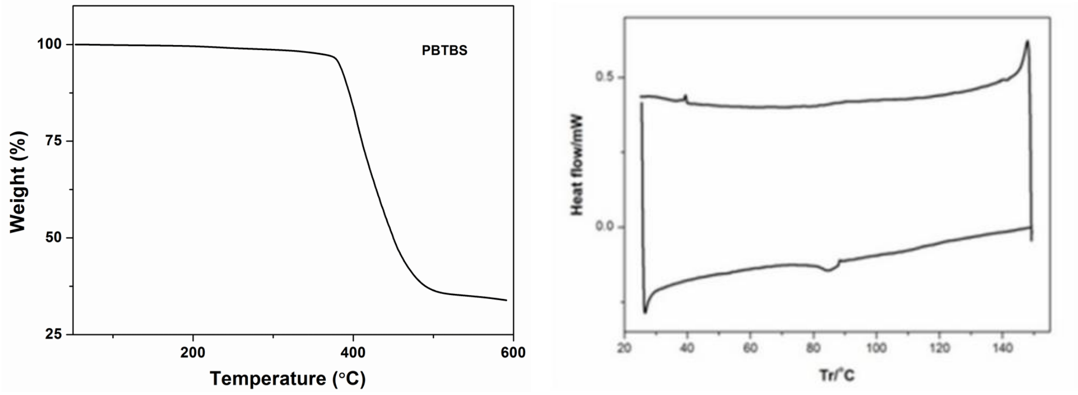

(a) (b)

Fig. 3-6 (a) TGA curve of PBTBS under N_2; and (b) DSC curves of PBTBS at 10 °C/min heating rate under N_2

Fig. 3-7 depicts the X-ray diffraction (XRD) patterns of PBTBS powder samples before annealing and with annealing at 80 °C, respectively. The XRD pattern of the sample exhibited distinctive crystalline peaks after annealing at 80 °C, indicative of lamellar π-stacking ordering. The reflection at $2\theta = 5.6°$, which corresponds to a *d*-spacing of 15.8 Å, which was attributed to the ordering of the alkyl side chain from the π-π stacking of the polymer main chain. The intermolecular spacings of the lamellar π-π stacking ordering can be deduced from the reflection at $2\theta = 3.6°$ (~24.5 Å, interchain distance); second order $2\theta = 7.8°$ (11.3 Å) and third order at $2\theta = 21.2°$ (~4.2 Å) and $2\theta = 22°$ (4 Å, π-π stacking), respectively. PBTBS showed strong π-π stacking interaction among adjacent polymer chains comparable to PQT-12 at $2\theta = 22.1°$ (4 Å, π-π stacking) [132].

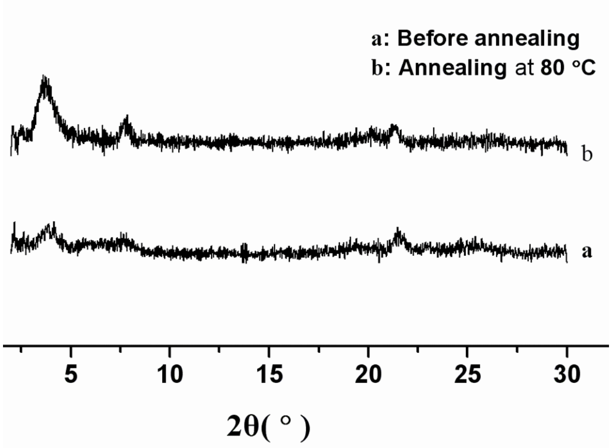

Fig. 3-7 Powder XRD patterns for PBTBS (a) before annealing; and (b) annealing at 80 °C

3.2.6 Characteristics of BHJ OPVs

Chemical Material Supply

[6,6]-phenyl-C61-butyric acid methyl ester (PCBM) (99.5% purity) obtained from Nano-C®. 1,2-dichlorobenzene (Chromasolv® HPLC grade, 99%) purchased from

Sigma Aldrich. Poly(3,4-ethylenedioxy-thiophene):poly(styrenesulfonate) (PEDOT:PSS) (P VP Al 4083) purchased from CLEVIOS™. All chemicals were used as received without further purification. Fig. 3-8 showed the energy level of material used for the solar cell devices.

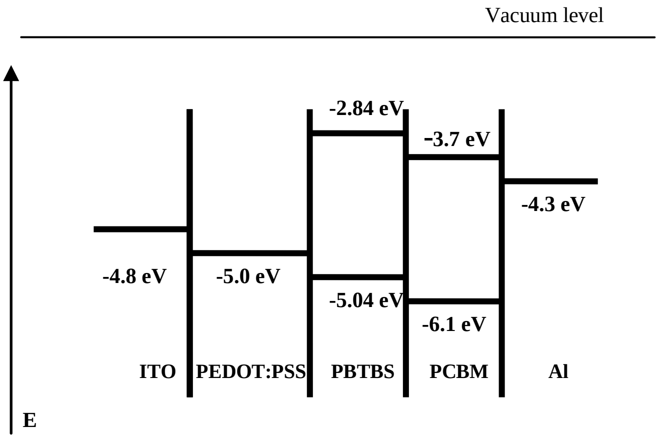

Fig. 3-8 Energy level diagram of the materials used for the solar cell devices

Device Fabrication

Organic solar cells with configuration ITO/PEDOT:PSS/PBTBS:PCBM(1:1 wt%)/Al and ITO/PEDOT:PSS/PQT-12:PCBM(1:1, wt%)/Al were fabricated. Fig. 3-9 shows the typical device structure of bulk heterojunction organic solar cell. The solar cells were fabricated by spin coating the active layers onto the indium tin oxide (ITO) coated glass substrates (7 Ω/sq, Kintec Company).

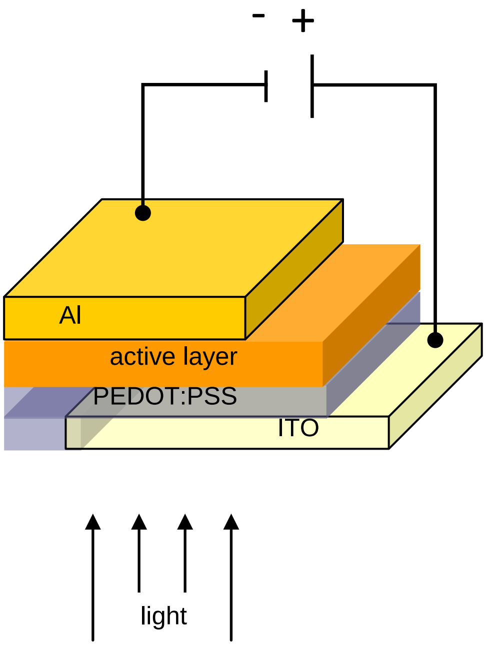

Fig. 3-9 Typical device structure of bulk heterojunction organic solar cell device

Fig. 3-10 depicts the scheme of ITO glass with the dashed area after etching. First, the ITO substrate was thoroughly cleaned by an ultrasonic treatment in acetone, ethanol and deionized water, subsequently. After drying the substrate through N_2 stream, followed by cleaning for 2 min with plasma cleaner (Harrick PDC-32G). Poly(3,4-ethylenedioxythiophene):poly(styrene sulfonate) (PEDOT:PSS) was deposited onto the ITO substrate by spin coating at 3000 rpm for 60 s, followed by heating at 140 °C for 15 min in a vacuum oven under N_2 atmosphere. The blend solutions were prepared by mixing PBTBS:PCBM and PQT:PCBM with weight ratio of 1:1 in dichlorobenzene (10 mg/ml), respectively. All solutions were filtered through 0.45 μm PTFE syringe filters prior to the deposition. Thereafter, the active layer was deposited from the dichlorobenzene solution onto the ITO coated glass substrate by spin coating at 600 rpm for 60 s in the glove box under N_2 atmosphere. Compared with the blend film of PBTBS/PCBM deposited at RT, the blend film of PQT-12/PCBM was deposited from dichlorobenzene solution by spin coating at 50˚C, due to the poor solubility of PQT-12 at RT.

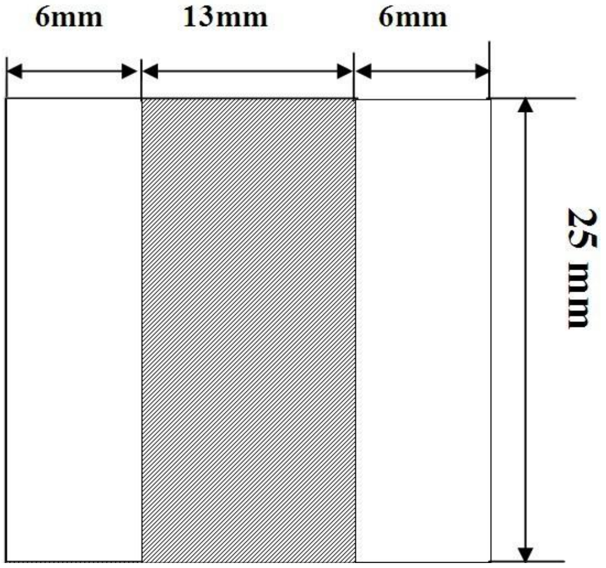

Fig. 3-10 The scheme of ITO glass after etching

Thereafter, the aluminum (Al) top electrodes (~100 nm) were evaporated onto the samples by thermal evaporation in vacuum (2×10^{-4} Pa) through a shadow mask (Fig. 3-11), resulting in devices with an active area of 0.1 cm^2. Post treatment of device annealing was carried out at 100˚C for 15 min in the glove box under N_2 atmosphere. Ten devices were fabricated in each run and all of the ten device were tested.

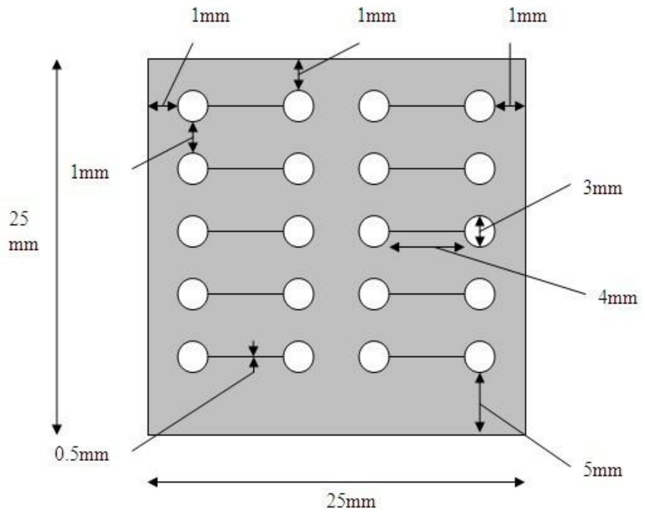

Fig. 3-11 The schematic of shadow mask with the related size

Device measurement

The current-voltage (*I*-*V*) characteristics of solar cells were measured under ambient atmosphere by a Keithley 2400 source measurement unit under a Xe lamp illumination with a power density of 100 mW/cm^2 (AM1.5). External quantum efficiency (EQE) measurements were tested by filtering the Xe lamp using a monochromator, and the signal was collected by a merlin detector and preamplifier. All electrical measurements were carried out at room temperature in air.

Fig. 3-12 depicts the *I*-*V* characteristics of PBTBS/PCBM and PQT-12/PCBM BHJ OPVs measured in dark and under illumination with an intensity of 100 mW/cm^2. The solar cells were post-annealed at 140 °C for 15 min in a vacuum oven under N_2 atmosphere. The device measurement was performed under 1 sun illumination (100 mW/cm^2). The photovoltaic properties of the solar cell using PQT-12/PCBM as the active semiconductor layer featured a J_{sc} of 1.8 mA/cm^2, a V_{oc} of 0.48 V, a *FF* of 0.40, resulting in a PCE of 0.5%.

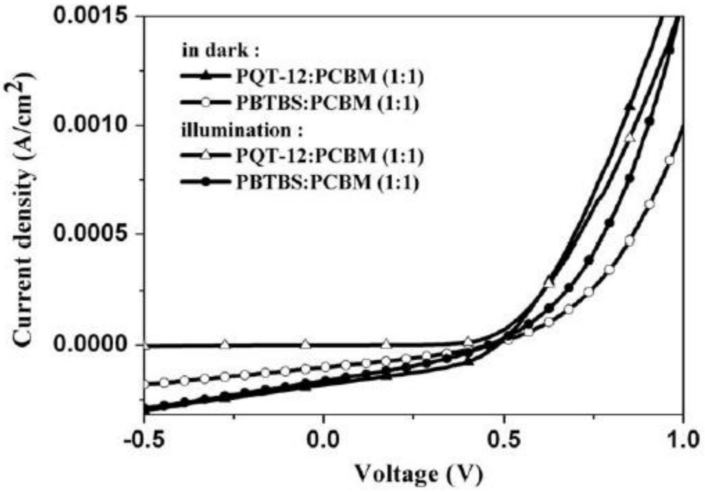

Fig. 3-12 *I-V* characteristics of solar cells based on PBTBS/PCBM and PQT-12/PCBM

In comparison, the solar cell based on the PBTBS/PCBM as the active semiconductor layer featured a PCE of 0.34%, having a J_{sc} of 1.7 mA/cm^2, a V_{oc} of 0.46 V and a FF of 0.32. Although the efficiency of solar cells based on PBTBS was lower than PQT-12, the V_{oc} and J_{sc} were comparable to that of PQT-12. The slight lowering of V_{oc} value resulted from the higher HOMO level of PBTBS compared to that of PQT-12. The much lower FF of the solar cell based on the PBTBS might be attributed to the higher contact resistance of the device than that of the PQT-12 [35].

The solar cells treated by thermal annealing show much higher PCE than the devices without annealing treatment, as shown in Fig. 3-13. Table 3-1 tabulates the photovoltaic properties of PBTBS and PQT-12 in BHJ OPVs. The annealed PBTBS: PCBM device resulted in a large increase in PCE from 0.015% to 0.34%, with J_{sc} from 0.12 mA/cm^2 to 1.7 mA/cm^2, V_{oc} from 0.33 V to 0.46 V, and FF from 0.27 to 0.32. On the other hand, devices based on PQT-12: PCBM treated by thermal annealing also showed the much higher PCE of 0.5%, compared to the 0.09% PCE of device without annealing. This might be attributable to the modified morphology in the active layer favorable for charge transfer after thermal annealing treatment.

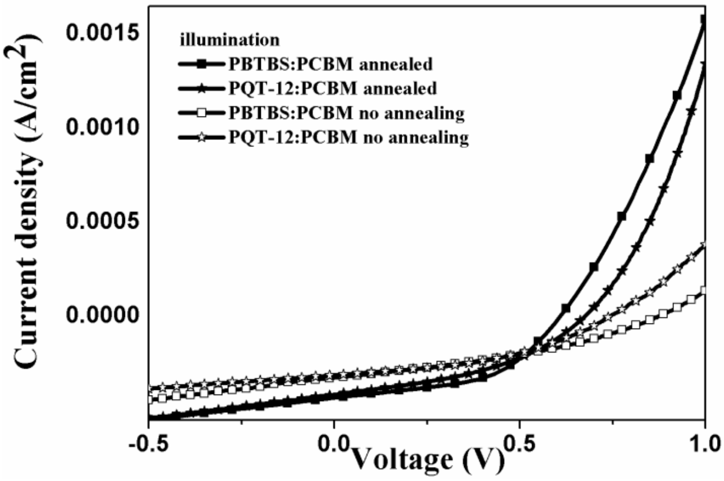

Fig. 3-13 *I-V* characteristics of solar cells based on PBTBS/PCBM and PQT-12/PCBM with and without thermal annealing treatment; respectively.

Table 3-1 Photovoltaic properties of PBTBS and PQT-12 in BHJ OPVs [a]

Active layer	**J_{sc} (mA/cm^2)**	**V_{oc} (V)**	***FF***	**PCE (%)**
PBTBS:PCBM (annealed)	1.7	0.46	0.32	0.34
PBTBS:PCBM (no annealing)	0.12	0.33	0.27	0.015
PQT-12:PCBM (annealed)	1.8	0.48	0.40	0.5
PQT-12:PCBM (no annealing)	0.006	0.35	0.29	0.09

[a] The thermal annealing was carried out at 15 min at 140 °C in a vacuum oven under N_2 atmosphere

3.2.7 External quantum efficiency of PBTBS

To understand the origin of the photocurrent in the solar cells based on PBTBS:PCBM and PQT:PCBM, external quantum efficiency (EQE) measurement was performed. As depicted in Fig. 3-14, it was observed that the wavelength range response of solar cells was similar to the broad optical absorption spectra. The blend of PBTBS/PCBM (1:1, wt%) featured the highest quantum efficiency of 3.37% at about 550 nm (about 2.25 eV), which is slightly larger than the bandgap of PBTBS (2.12 eV). While the broad spectra above 850 nm may be the fluctuation, which was caused by the whole low EQE. And the main reason may be the serious recombination in the active layer. The spectra based on PBTBS featured a slightly higher intensity response and broadened to the long wavelength than PQT-12, which were consistent with the absorption spectra measurement. Further work on processing optimization of devices are proposed to investigate in more detail.

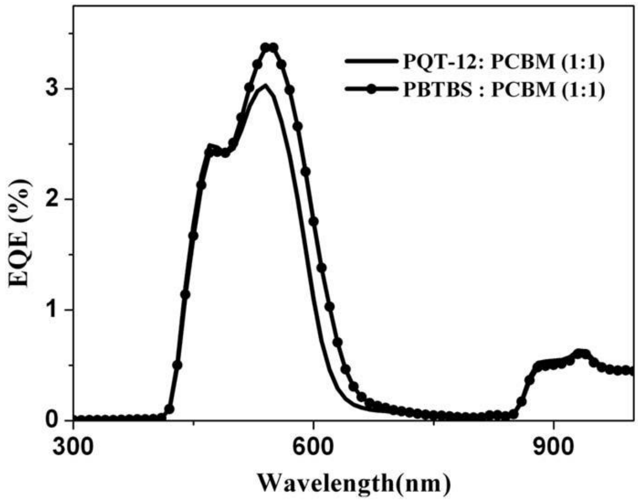

Fig. 3-14 The EQE curves of solar cells based on PBTBS/PCBM and PQT-12/PCBM

3.2.8 Characteristics of PBTBS-based OFETs

OFETs characteristics using PBTBS as an active semiconductor were also investigated. The charge carrier mobility of the OFET in the saturation region can be calculated from the gradient of the $(I_D)^{1/2}$ vs V_G line plot and the threshold voltage of the OFET can be obtained form the intercept, using the following equation: $I_D = W/(2L)C\mu(V_G-V_T)^2$. The on/off current ratio of the OFET is the ratio of current in the saturation region to the current in cut-off region, which can be obtained from $I_{on}/I_{off} = I_{max}/I_{mix}$.

The bottom-gate bottom-contact PBTBS based OFETs ($W/L = 50$) was first measured by annealing the organic semiconductors at 80 °C. However, the device shows a lower mobility of 6×10^{-5} cm^2/Vs and with an I_{on}/I_{off} ratio of 580. Moreover, the top-contact, bottom-gate OFETs were fabricated on *n*-doped silicon wafer as the gate electrode with a layer of 200 nm silicon oxide (SiO_2) as the dielectric. The semiconductor layer was deposited on top of octadecyltrichlorosilane (OTS) modified SiO_2 surface by spin coating the solution of PBTBS in chloroform (5 mg/mL) at 1500 rpm for 2 min, and then vacuum annealing at 120 °C for 1 h. The gold source and drain electrodes were subsequently deposited by thermal evaporation through a metal shadow mask.

The transfer and output characteristics of OFETs with PBTBS as the organic semiconductor were depicted in Fig. 3-15. The device showed a typical *p*-channel characteristic and featured a mobility of 1×10^{-3} cm^2/Vs and an I_{on}/I_{off} of 10^5, lower than PQT (0.14 cm^2/Vs) [56], with a V_T of -2 V. There are several factors that influence the mobility, such as molecular weight, polymer purity, morphology properties, annealing conditions and solvent effects. Therefore, it is expected that the mobility be further improved by polymer purification and device optimization.

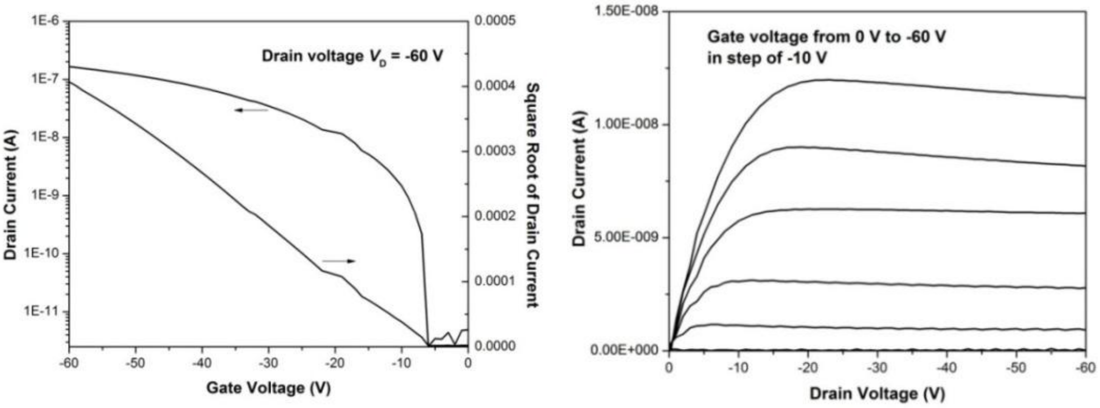

(a) (b)

Fig. 3-15 The transfer (a) and output (b) characteristics of PBTBS-based OFETs

3.3 *n*-type organic semiconductor of T3PT3

Perylenediimide derivatives feature good *n*-type field-effect behaviours under ambient atmosphere due to their low lying LUMO level [77, 133-135]. However, high perylene contents in the polymer blends may result in insufficient film thickness and poor film forming property due to low solubility. It was reported that *n*-type polymer semiconductors and dendritic molecules [133, 136-140] based on perylene-3,4:9,10-bis(dicarboximide) (PDI) or naphthalene-1,8:4,5-bis (dicarboximide) (NDI) [141] were widely explored, which provided unique electronic properties for the organic semiconductors in low-cost solution-processing device fabrication.

As discussed in Section 2.3, balanced electron and hole mobility can be achieved in low bandgap organic semiconductors. The reported highest hole mobility of N-alkyl diketopyrrolo-pyrroledithienythieno[3,2-b]thiophene (DPP-DTT)-based *p*-type organic semiconductor [65] features stronger donor to facilitate hole transport, while the *n*-type polymer semiconductor P(NDI2OD-T2) [73] has stronger acceptor to achieve good electron transporting properties.

A novel *n*-type organic semiconductor T3PT3 was designed and synthesized via donor-acceptor (D-A) molecular structure, which comprised of PDI moiety as the stronger acceptor and regioregular hexylthiophenes as the weaker donor. On one hand, the electron-deficient PDI moiety in the bulky compound lowers its LUMO level, thereby improving its ambient stability. On the other hand, the regioregular hexylthiophenes moieties endue this molecule with well ordering in the film state and good solubility for solution processing. T3PT3 is readily soluble in common organic solvents, such as chloroform and 1,2-dichlorobenzene. The optical, thermal and electrical properties of T3PT3 were preliminarily investigated.

3.3.1 Synthesis of T3PT3

Scheme 3-2 depicts the synthetic route of T3PT3 according to the reported method [142]. The starting material of 4-(4-hexyl-5-(4-hexyl-5-(4,5-dihexylthiophen-2-yl)thiophen-2-yl)thiophen-2-yl)benzenamine was synthesized according to reported methods [143-145]. In the molecular design, phenyl groups are incorporated into the bulky compound to serve as a bridge to connect the donor and acceptor moieties instead of thiophene groups, because it is more difficult to achieve nitration on the thiophene ring than on the phenyl ring.

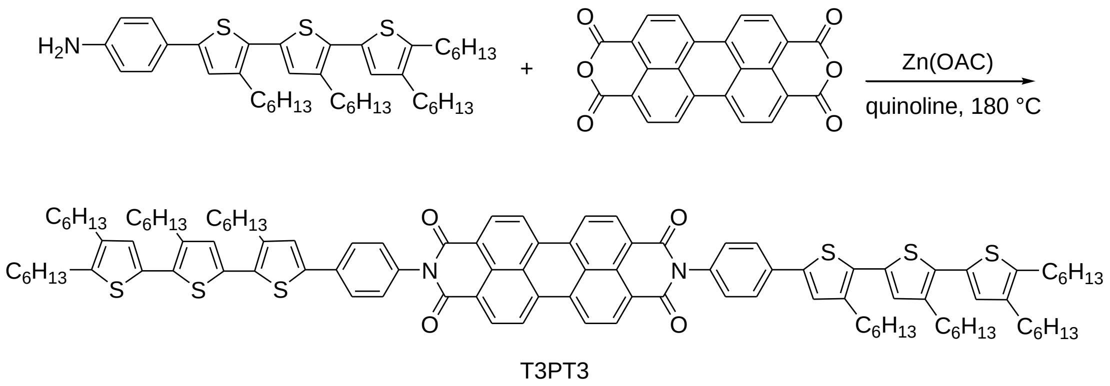

Scheme 3-2 Synthetic route of T3PT3

Target molecule ***T3PT3***

Add 4-(4-hexyl-5-(4-hexyl-5-(4,5-dihexylthiophen-2-yl)thiophen-2-yl)thiophen-2-yl)benzenamine (0.5438 g, 0.805 mmol), perylene-3,4,9,10-tetracarboxylic dianhydride (PTCDA) (0.07 mg, 0.178 mmol) and Zn(OAc) (35 g, 0.193 mmol) into quinolone (5.4 mL) and react at 180 °C under N_2 for 2 days. Treat the resultant mixture by concentrated HCl (12 M). The reaction resultant was extracted by CH_2Cl_2, and the organic phase was evaporated to get the crude product, which was purified by silicon gel chromatography. ^{1}H NMR (300 MHz, $CDCl_3$, δ): 8.74 (d, J = 7.2 Hz, 2H), 8.61 (s, 2H), 7.79 (d, J = 8.1 Hz, 2H), 7.41 (d, J = 7.8 Hz, 2H), 7.22 (s, 1H),7.0 (s, 1H), 6.93 (s, 1H), 2.8 (4H), 2.6 (4H), (24H), (12H).^{13}C NMR (300 MHz, $CDCl_3$, δ): 163.3, 143.7, 139.6, 135.5, 134.5, 133.9, 131.5, 130.9, 129.2, 127.2, 126.4, 123.3, 91.8, 67.9, 54.89, 31.7, 31.6, 30.5, 30.4, 29.6, 29.3, 29.1, 29.0, 28.9, 28.6, 25.6, 22.6, 14.1, 13.5. Calcd for $C_{108}H_{126}N_2O_4S_6$: C, 75.92; H, 7.43; N, 1.64; S, 11.26. Found: C, 74.36; H, 7.84; N, 1.59; S, 10.86.

3.3.2 Thermal properties of T3PT3

The thermal properties of T3PT3 were measured by TGA and DSC. As depicted in Fig. 3-16 (a), T3PT3 with onset of degradation (a weight loss ~5%) occurred at 389 °C (T_d), indicative of good thermal stability. The thermally induced phase transition behaviors of T3PT3 were investigated by DSC. Fig. 3-16 (b) depicts the DSC curves of T3PT3 at 10 °C/min heating rate under N_2. It was observed that an endothermic peak occurred at 168 °C for melting (T_m) during the second heating process and an exothermic peak at 125 °C for recrystallization (T_c) upon cooling, respectively. The thermal properties provide the deposition and annealing conditions for ensuing device fabrication.

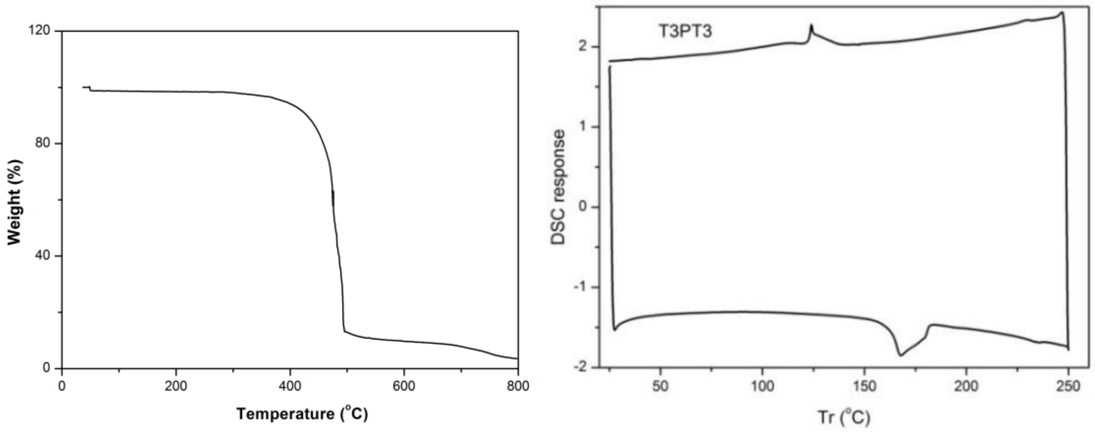

(a) (b)

Fig. 3-16 (a) TGA curve of PBTBS under N2; and (b) DSC curves of T3PT3 at 10 °C/min heating rate under N_2

3.3.3 Optical properties of T3PT3

Fig. 3-17 depicts the absorption spectra of T3PT3 in the 1,2-dichlorobenzene (DCB) solution and the film state. The absorption peaks of T3PT3 were observed at 368 nm, 460 nm, 492 nm and 529 nm in the solution. In comparison, the absorption peaks of T3PT3 in the film state exhibited a red shift to 378 nm, 475 nm, 500 nm and 544 nm, respectively. In addition, the absorption spectra of T3PT3 in the film state are broader, which was attributable to well-ordering of the hexylthiophene and PDI moieties in the condensed phase film. It is known that the commonly used acceptor molecule PCBM has no visible light absorption. PDI moiety in the bulky compound of T3PT3 features a large molecular-absorption coefficient in the visible region, and regioregular hexylthiophenes endow this novel acceptor molecule with good solubility. From the onset wavelength in the UV-vis spectra, the optical bandgap of T3PT3 film was calculated to be 1.7 eV.

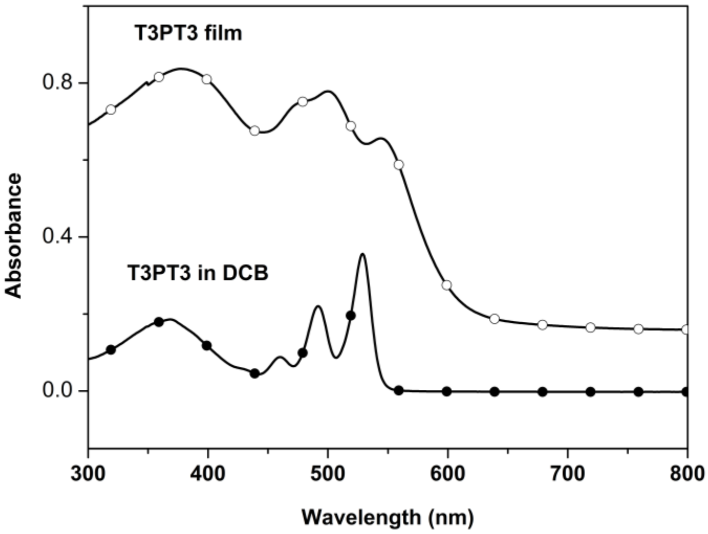

Fig. 3-17 UV spectra of T3PT3 in the solution and the film state

Fig. 3-18 depicts the UV-vis spectra of the pristine P3HT film and the blend of P3HT/T3PT3 film, respectively. The mixed solution of P3HT (5 mg) and T3PT3 (5 mg) in 1,2-dichlorobenzene (1 mL) was prepared and stirred overnight at 50 °C under nitrogen atmosphere. Subsequently, the solution was filtered through a syringe filter nylon membrane of 0.22 μm to remove the contaminants. The blend solution was spin coated at the speed of 1000 rpm for 1 min to form a smooth blend film on the ITO substrate. The maximum absorption of pristine P3HT film occurred at 553 nm, and the maximum absorption (557 nm) of P3HT/T3PT3 (1:1, wt%) blend film featured a slight red shift with a shoulder peak at 600 nm. The absorption spectra of the P3HT/T3PT3 blend film covered the visible region in the solar spectrum, which is promising for sunlight photo absorption in the BHJ OPVs.

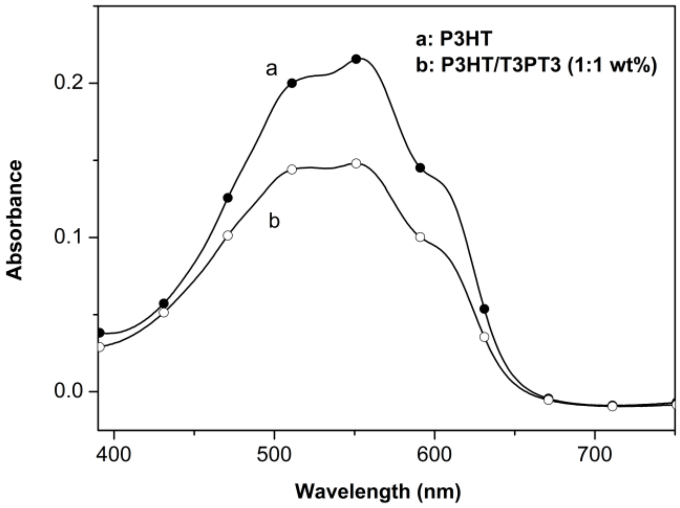

Fig. 3-18 UV spectra of the pristine P3HT film and the P3HT/T3PT3 blend film

In order to investigate T3PT3 as an acceptor group in BHJ OPVs, PL spectra of the pristine P3HT film and the blend P3HT/T3PT3 film were measured at the excitation of

553 nm, which was the maximum absorption of P3HT. Fig. 3-19 depicts the PL spectra of the pristine P3HT film and the P3HT/T3PT3 (1:1, wt%) blend film, respectively. The predominant PL emission peak of the pristine P3HT was observed at around 636 nm, while the emission peak of the blend P3HT/T3PT3 film was quenched to ~5% of that of the pristine P3HT. It was indicated that the electron was transferred from the donor to the acceptor, which makes it possible to fabricate BHJ OPVs using P3HT/T3PT3 as the active semiconductor layer.

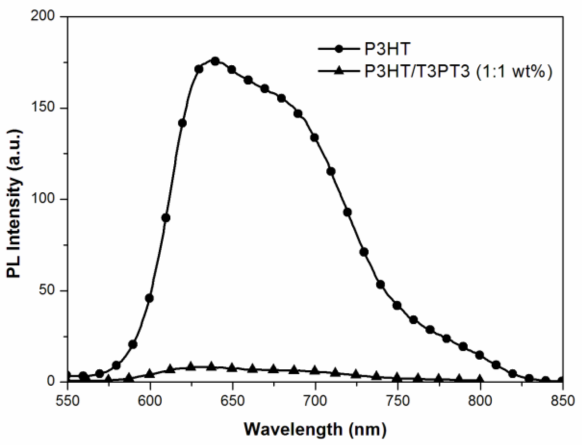

Fig. 3-19 PL spectra of the pristine P3HT film and the P3HT/T3PT3 blend film

3.3.4 Electrochemical properties of T3PT3

The electrochemical properties of T3PT3 were measured by cyclic voltammetry (CV) and the CV curves were depicted in Fig. 3-20. T3PT3 exhibited two reversible waves corresponding to successive reduction of the PDI units at -0.24 V and -0.5 V and one irreversible broad waves at 1.4 V corresponding to oxidation of the oligothiophene units. The HOMO and LUMO levels are extracted from the following equations: IP =

$E_{\text{onset (ox)}} - E_{\text{FOC}} + 4.8$ and EA = $E_{\text{onset (red)}} - E_{\text{FOC}} + 4.8$ ($E_{\text{FOC}} = 0.46$ V). From the onset of the oxidation potential of 1.4 V and the onset of the reduction potential of -0.24 V, the HOMO and LUMO levels of T3PT3 were calculated to be -5.7 eV and -4.1 eV, which was 0.4 eV higher than the HOMO level of PCBM (-6.1 eV) and 0.4 eV lower than the LUMO level of PCBM (-3.7 eV), respectively. The electrochemical gap of T3PT3 is calculated to be 1.6 eV.

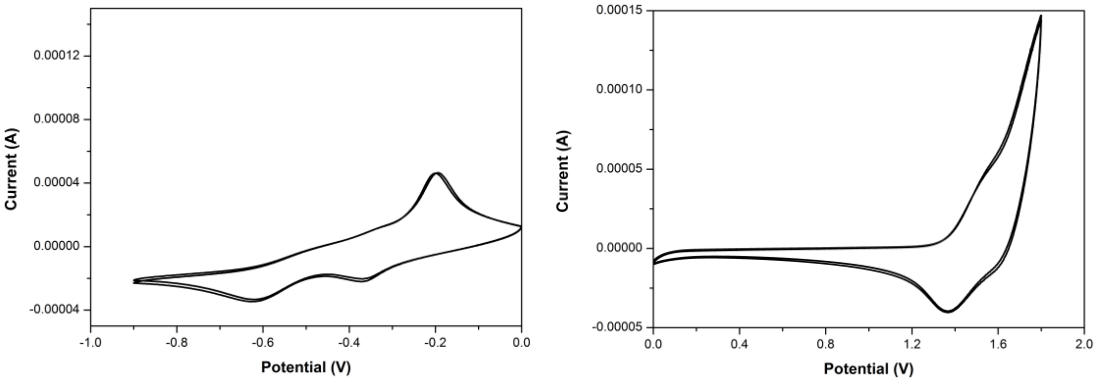

(a) (b)

Fig. 3-20 Cyclic voltammogram of T3PT3 film coated on a glass carbon electrode in 0.1 M Bu_4NBF_4/acetonitrile at scan rate of 100 mV/s: (a) cathodic scanning; and (b) anodic scanning

3.3.5 Morphology of T3PT3

The surface morphology of the pristine T3PT3 film and P3HT/T3PT3 blend film were measured using atomic force microscopy (AFM). The films were spin-coated from DCB and annealed at 170 °C for 15 min and cooled down to RT under vacuum. Fig. 3-21 depicts AFM topographic images of the pristine T3PT3 film and the P3HT/T3PT3 blend film. The pristine T3PT3 showed phase-separated domains with a root mean square roughness (R_q) of 2.34 nm. A dramatic change in the surface morphology is observed from the P3HT/T3PT3 blend film. Firstly, the surface roughness decreased from 2.34 nm to 1.65 nm. Secondly, with blending donor P3HT, the phase-separated domain sizes decreased compared to pristine T3PT3. Thirdly, the P3HT/T3PT3 blend film featured better ordering than the pristine T3PT3 film, thereby obtaining a large interface of the donor and acceptor to achieve efficient intermolecular charge transfer.

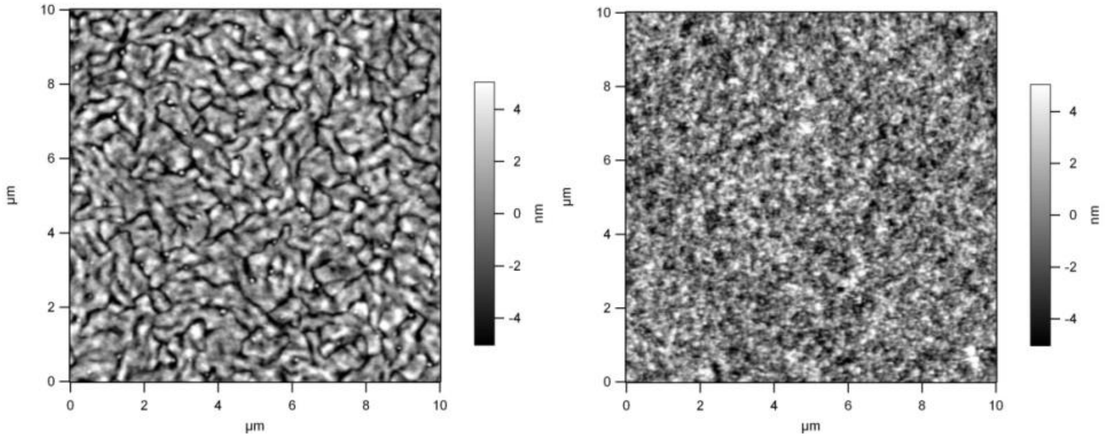

(a) (b)

Fig. 3-21 AFM topographic images of (a) T3PT3 film; and (b) P3HT/T3PT3 blend film

3.3.6 Characteristics of BHJ OPVs

The photovoltaic properties of T3PT3 as an electron material in BHJ OPVs were investigated using P3HT as an donor material. BHJ OPVs with the configuration of ITO/PEDOT:PSS/P3HT:T3PT3(1:1, wt%)/Al were fabricated. Ten devices were fabricated in each run and all of the ten device were tested. Fig. 3-22 showed the energy level of material used for the solar cell devices.

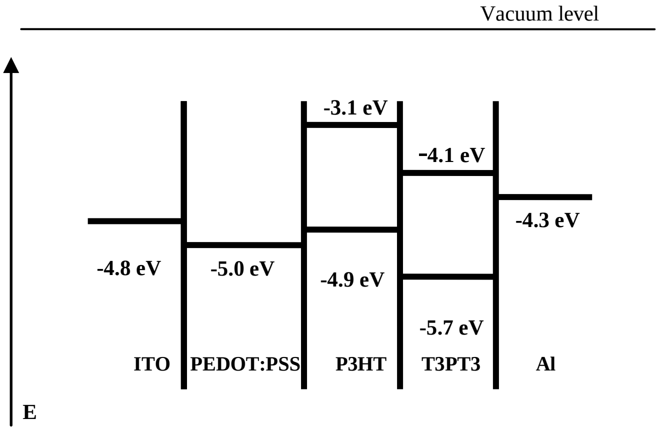

Fig. 3-22 Energy level diagram of the materials used for the solar cell devices

Fig. 3-23 depicts the *I-V* characteristics of P3HT/T3PT3 BHJ OPVs in dark and under illumination with an intensity of 100 mW/cm^2. The photovoltaic properties of the solar cell using P3HT/T3PT3 as the active layer featured a PCE of 0.041%, a J_{sc} of 0.3 mA/cm^2, a V_{oc} of 0.41 V, and a *FF* of 0.336. T3PT3 shows poor PV activity, and the bi-layer cells based on this new material deposited by the vapor deposition is to be fabricated and investigated in the future.

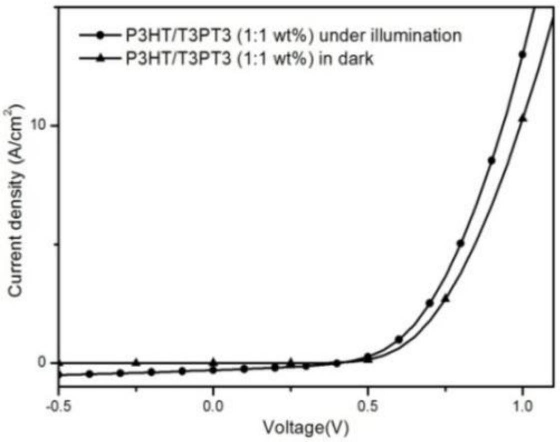

Fig. 3-23 *I-V* curves of the blend P3HT/T3PT3 solar cell device

In sum, the low efficiency of the solar cells based on T3PT3 is largely because of the less controlled morphology of the active layers deposited from solution than by the vapor deposition process. Moreover, it is observed that the solubility and film-forming properties of this *n*-type organic semiconductor are not good, thus causing short circuits of the ensuing solar cell devices.

3.4 Conclusions

Bulk heterojunction organic solar cells based on a novel regioregular selenophene and thiophene-based polymer PBTBS as the electron donor material blended with PCBM have been fabricated and characterized. The photovoltaic properties of solar cells based on PBTBS are comparable to that of PQT-12. The EQE measurements indicate that the cell based on the PBTBS showed much better performance with ~3.37% at 550 nm compared to PQT-12. In addition, PBTBS-based OFETs featured *p*-channel characteristics and exhibited a hole mobility of 1×10^{-3} cm^2/Vs.

A novel solution-processable *n*-type organic semiconductor T3PT3 based on PDI and alkylthiophene has also been successfully synthesized. Its photovoltaic properties applied as the electron acceptor material in BHJ OPVs were preliminarily investigated.

Chapter 4 Fluoropolymers for Polymer Nanocomposite Dielectrics

4.1 Introduction

This chapter delineates the author's research work pertaining to the formulation of a polymer nanocomposite dielectric for OFETs on Al foils. A large part of this chapter is extracted from the author's publication [36] in the Organic Electronics journal.

To achieve high performance OFETs, it is imperative to develop solution-processable high-mobility organic semiconductors and high-capacitance dielectric materials. For low-voltage operation, the capacitance should be high, either by increasing the dielectric constant (*k*) or decreasing the thickness (*d*) of the gate dielectric. In PE, high-*k* polymer nanocomposite dielectric materials [146] have attracted much interest largely because they are able to meet the requirements of good solution processability and feature mechanical properties of polymers combined with unique electrical properties of nanoparticles. Selected ceramic nanoparticles increase the capacitance not only through its high intrinsic dielectric constant, but also through the ability to fabricate thin dielectric layer. Thus far, high-*k* polymer nanocomposite materials have been widely explored by incorporating nanoparticles such as TiO_2 [97, 147] and $BaTiO_3$ [98, 100]. The polymer matrices included thermosetting epoxy resin and polyimide (PI), thermoplastic poly(methyl methacrylate) (PMMA) and polyvinylidenefluoride (PVDF)-based fluoropolymers. The epoxy/$BaTiO_3$ nanocomposite dielectric [102] was reported with a capacitance in excess of 6 nF/cm^2 and a high dielectric constant of 35. $BaTiO_3$ hybrid PMMA dielectric was deposited by gravure printing, having a dielectric constant of 13 and an average capacitance of 5 nF/cm^2 [25]. Among all the polymer matrices, PVDF-based fluoropolymers have attracted much attention due to their advantages of high capacitance, high thermal stability, high chemical stability and good water repellency. By increasing loading of nanopowders in poly(vinylidenefluoride-co-trifluoroethylene) (P(VDF-TrFE)), the nanocomposites exhibited a dielectric constant up to 51.5 [148]. Low-voltage, high-speed flexible complementary polymers electronic circuit [19, 149] was achieved using the PVDF-based blend dielectric film.

In this part, P(VDF-TrFE) blending PMMA was chosen as the polymer matrix for polymer nanocomposite dielectric, with an optimum blending concentration of 30 wt%. High-*k* $BaTiO_3$ was incorporated into the blend polymer matrix of P(VDF-TrFE)/PMMA to improve the electrical properties. In order to achieve fully-additive printed OFETs fabrication, screen-printable dielectric materials of P(VDF-TrFE)/PMMA/Silica (PPS) and P(VDF-TrFE)/PMMA/$BaTiO_3$/Silica (PPBS) were formulated, which are promising for the fabrication of fully-additive PE.

4.2 Fluoropolymer dielectrics

All the traditional polymer dielectrics, such as PMMA, can be deposited to cover a large substrate by spin coating or other casting methods, but the annealing temperature is so high and unfavorable for low-temperature processing required by PE. Fluoropolymers have attracted much interest due to their advantages of high capacitance, high thermal stability, high chemical stability and good water repellency. One of the disadvantages is the leakage current and the ferroelectric loss under a high electric field due to low volume resistivity. This problem can be overcome by control of fluoropolymer chain conformation or by blending polymers with high volume resistivity into the fluoropolymers. Fig. 4-1 depicts the molecular structure of two fluoropolymers of poly(vinylidene fluoride-co-hexafluoropropylene) (P(VDF-HFP)) and P(VDF-TrFE).

P(VDF-HFP) P(VDF-TrFE)

Fig. 4-1 Molecular structure of two fluoropolymers

Two PVDF-based fluoropolymers of P(VDF-HFP) and P(VDF-TrFE) were applied as the gate dielectrics for bis(triisopropylsilylethynyl) pentacene (TIPs-pentacene) OFETs fabricated on a plastic substrate. The contact angles of P(VDF-HFP) and P(VDF-TrFE) dielectric films are ~100^{o} and 105^{o}, respectively. Due to its good solvency properties, 1-methyl-2-pyrrolidinone (NMP) solvent was used to dissolve the fluoropolymers, thereby inducing the dipolar interaction between fluoropolymers and NMP. In addition, NMP belongs to the class of environmentally friendly solvents, and its possessing properties, such as low volatility, low flammability and relatively low toxicity, are favorable for the formulation of dielectric inks for printing under ambient atmosphere.

As discussed in Section 2.4, TIPs-pentacene is chosen as the active semiconductor for OFETs fabrication in PE due to its ease of the morphology control when deposited from solution. TIPs-pentacene OFETs were fabricated on Al foils, with the dielectric layer deposited by spin coating, and subsequently the source and drain electrodes deposited by screen printing, with the active semiconductor layer deposited by slot die coating. TIPs-pentacene, having a HOMO level of -5.3 eV, fails to match the work function of Ag (-4.7 eV) and increases the hole injection barrier. Self-assembled monolayers of pentafluorobenzenethiol (PFBT) were used to modify Ag electrodes [50]. PFBT-treated Ag electrode possesses a work function of -5.35 eV and a water contact angle of 86^{o}.

Fig. 4-2 shows the molecular structure of TIPs-pentacene and PFBT. The hydrophobic property of metal electrodes is favorable for better molecular ordering of TIPs-pentacene along the contact edge. Slot die coating was applied to deposit organic semiconductor layer on the spin-coated dielectric layer, and the crystallization of TIPs-pentacene was directional across the transistor channel.

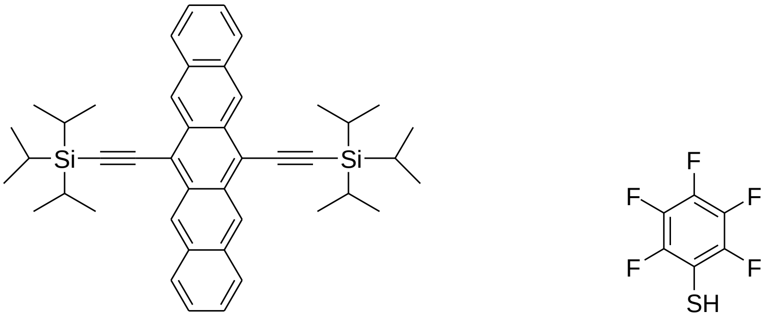

(a) (b)

Fig. 4-2 Molecular structure of (a) TIPs-pentacene; and (b) PFBT

4.2.1 Experimental

Chemicals

P(VDF-HFP) and P(VDF-TrFE) (70/30, mol%) procured from Info Piezotech. 3-glycidoxypropyltrimethoxysilane (GPTMS) from Gelest. PMMA (M_w = 120,000), TIPs-pentacene, PFBT, and NMP (anhydrous, 99.5%) obtained from Sigma-Aldrich. DuPont 5028 Ag paste for screen printing purchased from DuPont. All the commercial reagents and solvents were used without further purification unless otherwise noted.

Equipments

AFM was measured by Bruker Dimension Icon Microscope System. Cross section specimens for SEM were prepared by cross section polisher JEOL IB-09010CP. SEM micrographs were observed by Scan Gen B for JSM 5600. The silver source and drain electrodes of the transistor device were deposited by Dek 265 Horizon Auto Stencil Printer. TIPs-pentacene as the active semiconductor was deposited by Model Coatmaster 510 Film Applicator & Dying Time. The transfer and output characteristics of the OFETs were measured by Semiconductor Characterization System 4200-SCS.

Device Fabrication and characterization

As depicted in Fig. 4-3, the bottom-gate bottom-contact (BGBC) OFETs were fabricated on an Al foil (40 nm Al on 120 μm PET). Flexible substrate was cleaned by isopropanol and deionized water sequentially. The polymer dielectric dissolved in NMP (15 wt%) was spin coated at 1800 rpm for 1 min on the Al foil and cured at 120 °C for 1 h without further surface treatment. The silver source and drain electrodes were deposited on the dielectric layer by screen printing, with a thickness of 30 μm.

The transistor devices were cleaned by isopropanol and deionized water and dried at 50 °C for 15 min under vacuum followed by immersing in PFBT/ethanol (1.4 μL/1 mL) solution for 1 h to treat the Ag electrodes. TIPs-pentacene (3 wt%) was dissolved in a mixed solvent of toluene/anisole (4:1). This solution was subsequently deposited upon the Ag electrodes and the dielectric layer by slot die coating at the substrate temperature of 70 °C and annealed at 90 °C for 30 min on a hotplate. The OFETs characteristics were measured under ambient condition. All OFETs have an aspect width/length ratio of 40,000 μm:100 μm.

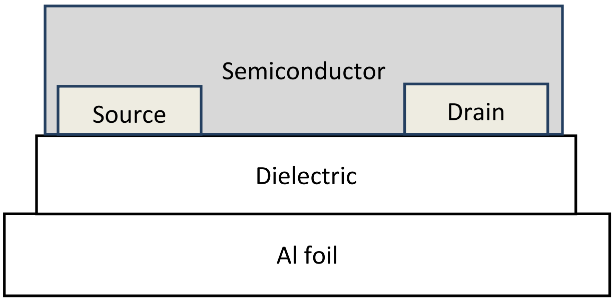

Fig. 4-3 Schematic cross section of BGBC OFETs

Deposition methods

Apart from slot die coating, other deposition methods were also explored to deposit TIPs-pentacene on the transistor channel. Drop cast film shows a visibly non-uniform film and improved the molecular ordering, while spin coating procedure is hardly continuous and controllable in the case of TIPs-pentacene. High boiling solvent encourages slow solvent evaporation and slow film formation speed that facilitates the growth of highly ordered crystal structures, so a mixture solvent of toluene and anisole (4:1) was used to dissolve TIPs-pentacene. The substrate temperature for slot die coating also greatly influences the crystallization of TIPs-pentacene. With the substrate temperature at RT, the nucleation rate of the crystal is high, but the crystal growth rate is low and a small grain size is formed. By increasing the substrate temperature, the average sizes of the crystal tend to grow, but the amount of the nucleation drops. A point to note is that the semiconductor deposited from the solution may destroy the flexible substrate at high substrate temperature. In this research, the suitable substrate temperature for the organic semiconductor layer by slot die coating is deemed to 70 °C.

4.2.2 P(VDF-HFP) as the gate dielectric

The dielectrics P(VDF-HFP) blended PMMA with concentrations of 10 wt%, 20 wt%, and 30 wt% were formulated, and subsequently deposited on Al foils by spin coating. Fig. 4-4 depicts the AFM topographical and phase images of pristine P(VDF-HFP) and P(VDF-HFP) blended PMMA concentrations of 10 wt%, 20 wt%, and 30 wt%, respectively. The dielectric films featured amorphous phase with cotton-like structure, which was unfavorable for the crystal growth of TIPs-pentacene on the dielectric layer. With blending PMMA of 30 wt%, the surface roughness was 31.2 nm and the optimized ratio of P(VDF-HFP) to PMMA is 7:3. Fig. 4-5 depicts the cross section SEM micrograph of P(VDF-HFP)/PMMA (30 wt%). Cross section specimens for SEM measurement were prepared by cross section polisher to investigate the morphology of bulk dielectric film. Moreover, the dielectric thickness was directly determined from the cross-section SEM images. Consistent with the surface morphology, the amorphous phase was also observed from the SEM image in the bulky polymer dielectric. The dielectric thickness deposited by spin coating was 3 μm.

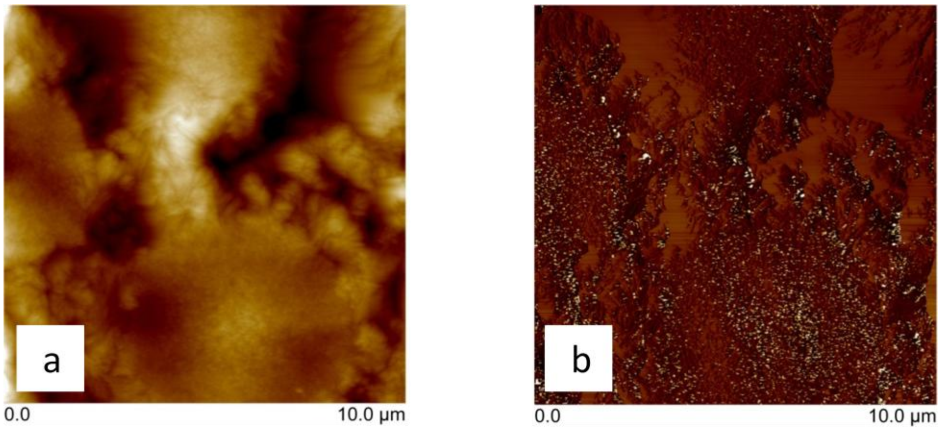

(i)

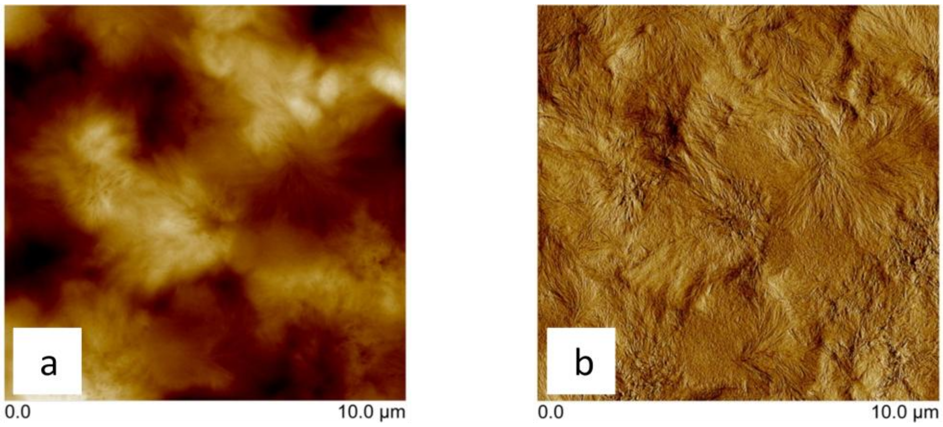

(ii)

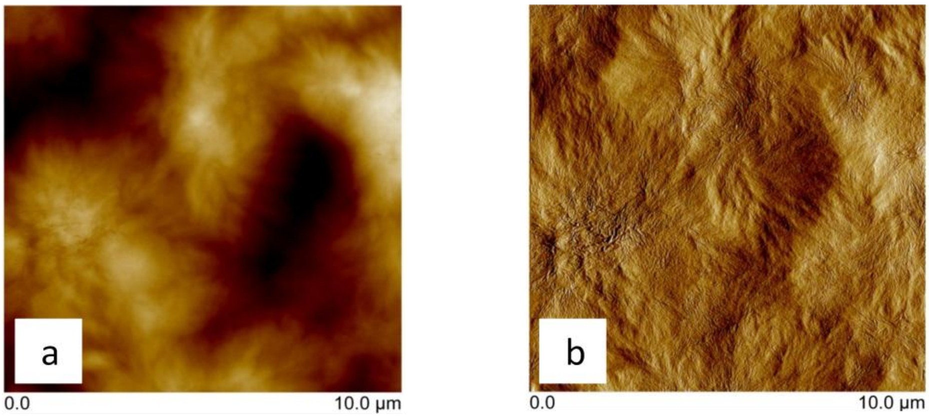

(iii)

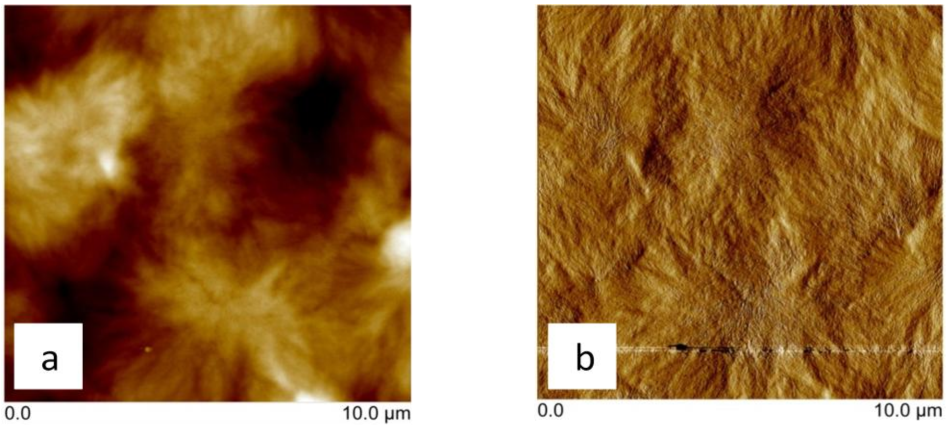

(iv)

Fig. 4-4 AFM topographical (a) and phase (b) images of (i) pristine P(VDF-HFP) and P(VDF-HFP) blending PMMA concentrations of (ii) 10 wt%, (iii) 20 wt%, and (iv) 30 wt%

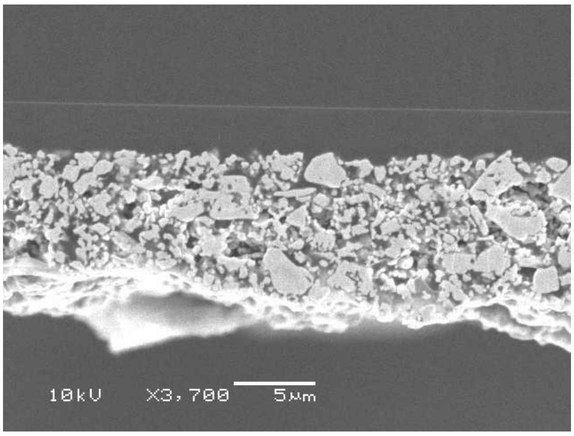

Fig. 4-5 Cross section SEM micrograph of P(VDF-HFP)/PMMA (30 wt%)

All the OFETs were fabricated on Al foils, with the dielectric layer deposited by spin coating and with source and drain electrodes by screen printing. The active semiconductor layer of TIPs-pentacene was deposited by slot die coating. TIPs-pentacene OFETs using pristine P(VDF-HFP) as the gate dielectric featured a small I_{on}/I_{off} and a large leakage current of 10^{-8} A, which can be increased under a high electric field. Blending PMMA with the fluoropolymer adjusted the electrical properties of the resultant polymer dielectric, thereby inhibiting the gate leakage current and increasing the I_{on}/I_{off}. By blending PMMA of 10 wt%, the leakage current of the transistor was reduced to 10^{-9} A.

Fig. 4-6 depicts the transfer and output characteristics of TIPs-pentacene OFETs with P(VDF-HFP)/PMMA (10 wt%), P(VDF-HFP)/PMMA (20 wt%), and P(VDF-HFP)/PMMA (30 wt%) as the gate dielectrics, respectively. As depicted in Fig. 4-6(iii), TIPs-pentacene OFETs using P(VDF-HFP)/PMMA (30 wt%) as the gate dielectric featured a mobility of 0.01 cm^2/Vs with an I_{on}/I_{off} of 10^4. Fig. 4-7 depicts the *I*-*V* characteristics of TIPs-pentacene OFETs using P(VDF-HFP)/PMMA (30 wt%) under dual bias sweeping. It was observed that the transistor using this dielectric exhibited a small hysteresis, since the surface of the polymer blend contained a low density of electron traps such as hydroxyl groups.

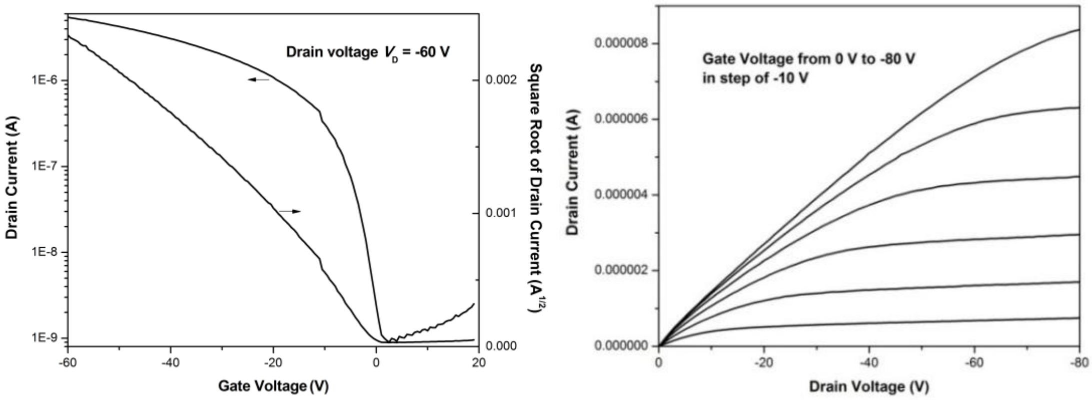

(a) (b)

(i)

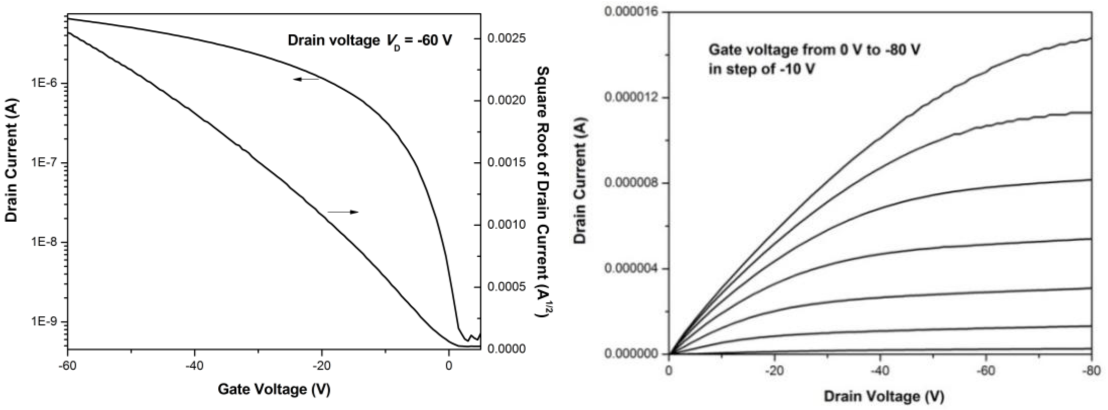

(a) (b)

(ii)

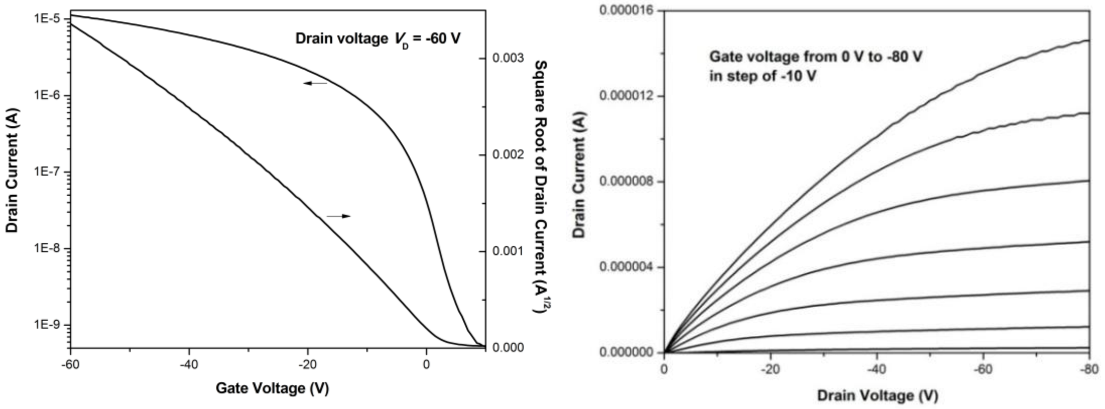

(a) (b)

(iii)

Fig. 4-6 The transfer (a) and output (b) characteristics of TIPs-pentacene OFETs with (i) P(VDF-HFP)/PMMA (10 wt%)**,** (ii) P(VDF-HFP)/PMMA (20 wt%), and (iii) P(VDF-HFP)/PMMA (30 wt%) as gate dielectrics

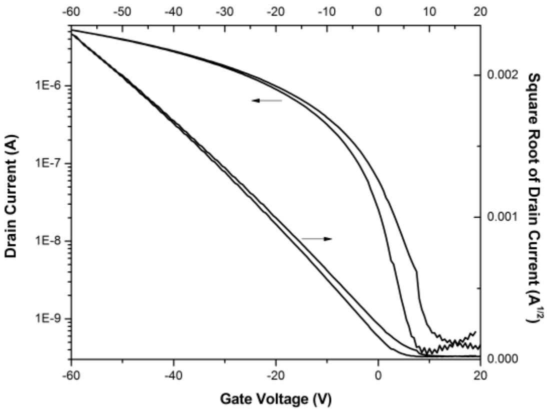

Fig. 4-7 The *I*-*V* characteristics of TIPs-pentacene OFETs with P(VDF-HFP)/PMMA (30 wt%) as the gate dielectric under dual bias sweeping

Table 4-1 tabulates the dielectric properties of P(VDF-HFP)/PMMA and the electrical characteristics of TIPs-pentacene OFETs. When PMMA concentration increased from 10 wt% to 30 wt%, the dielectric constant was decreased by 16% from 4.4 to 3.7, and the V_T increased from 0.3 V to 3.0 V. In Table 4-1, the capacitance per unit area of the dielectric was obtained from the capacitance-voltage curve with a capacitor area of 1×1 cm^2.

Table 4-1 Properties of P(VDF-HFP)/PMMA and TIPs-pentacene OFETs with P(VDF-HFP)/PMMA as gate dielectrics

PMMA (wt%)	**C (nF/cm^2)**	***k***	**V_T (V)**	**R_q (nm)**	**μ (cm^2/Vs)**
10	1.3	4.4	0.3	51.6	0.006
20	1.2	4.0	2.0	63.8	0.01
30	1.1	3.7	3.0	31.2	0.01

Ultimately, P(VDF-HFP) was not chosen as the polymer matrix for ensuing polymer nanocomposite dielectric ink formulation because of its amorphous surface morphology unfavorable for the crystallization of the organic semiconductor.

4.2.3 P(VDF-TrFE) as the gate dielectric

High-k fluoropolymer P(VDF-TrFE) exhibits ferroelectric properties due to strong dipolar polarization in the crystalline β-phase of the polymer film. Amorphous PMMA was blended to fill the space among the crystal grains, thus reducing the amount of ferroelectric crystalline and avoiding hysteresis. Moreover, the surface of the polymer blend contains a low density of electron traps such as hydroxyl groups, so little charge trapping was observed at the interface of the dielectric/semiconductor and in the bulk dielectric. Pristine P(VDF-TrFE) (70/30, mol%) has a curie temperature (T_c) of 112 °C, so the thermal curing temperature of the dielectric film is 120 °C above the curie temperature, thereby maintaining randomly aligned in a paramagnet. P(VDF-TrFE)/PMMA dielectric films were deposited by spin coating on Al foils.

The surface morphology of P(VDF-TrFE)/PMMA films was measured by the tapping mode AFM. The surface morphology and the crystallinity of P(VDF-TrFE)/PMMA film greatly varied with the blending concentration of amorphous PMMA. As depicted in Fig. 4-8(i), pristine P(VDF-TrFE) featured long and flexible fiber-like crystals, which are typical of β-phase crystals, with tens of nanometers in diameter [150]. P(VDF-TrFE)/PMMA (20 wt%) dielectric film depicted in Fig. 4-8(iii) exhibited short and flexible fiber-like crystals compared to pristine P(VDF-TrFE). Therefore, the surface morphology of the dielectric film not only depended on the amount of the amorphous PMMA, but also on other significant factors such as solution concentrations, coating speeds, annealing conditions. P(VDF-TrFE)/PMMA (10 wt%) dielectric film depicted in Fig. 4-8(ii) featured rigid rod-like crystal structure, and P(VDF-TrFE)/PMMA (30 wt%) depicted in Fig. 4-8(iv) exhibited similar crystal structure with a slightly larger diameter of about 280 nm. It was expected that the rod-like crystal structure of the dielectric layer could facilitate the crystallization of TIPs-pentacene and improve the device performance.

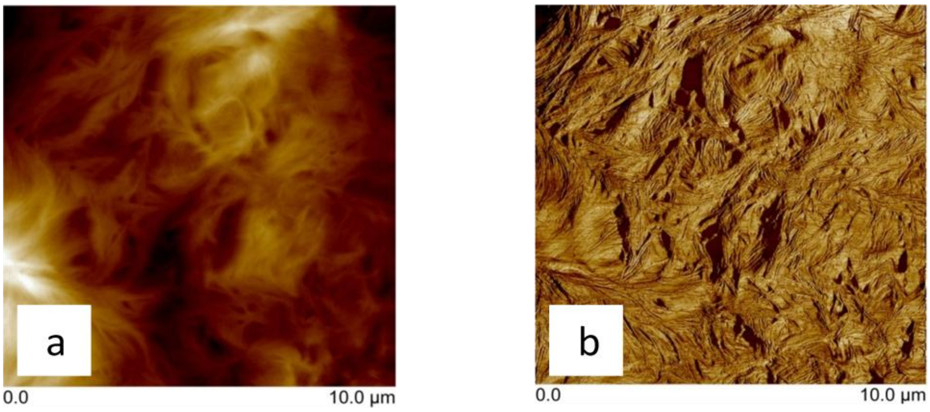

(i)

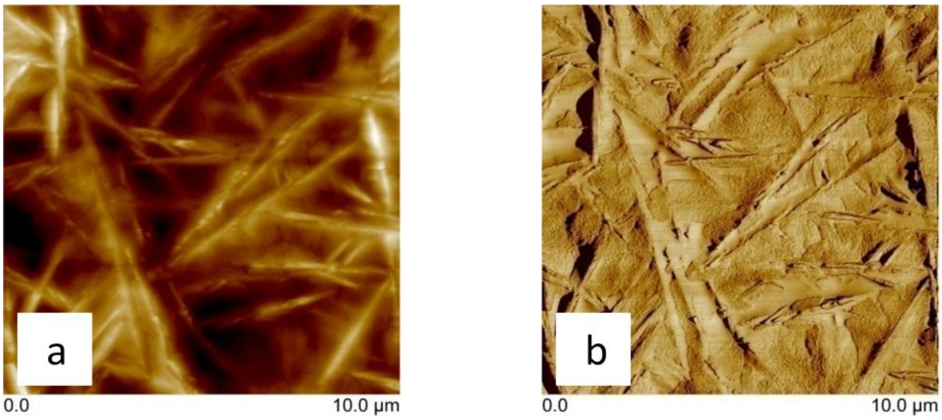

(ii)

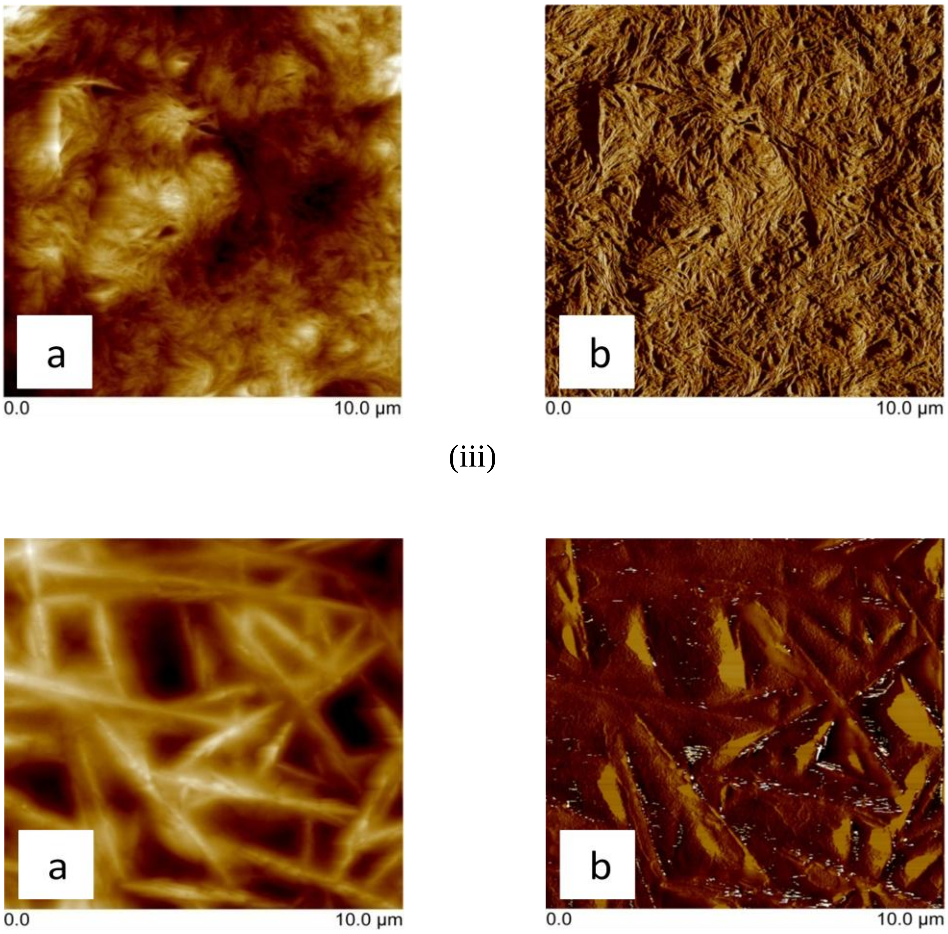

(iii)

(iv)

Fig. 4-8 AFM topographical (a) and phase (b) images of (i) pristine P(VDF-TrFE) and P(VDF-TrFE) blended with PMMA concentrations of (ii) 10 wt%, (iii) 20 wt%, and (iv) 30 wt%

The dielectric layers were deposited from different solution concentrations by spin coating at different speeds on Al foils, so the resultant films have different thicknesses, with the dielectric P(VDF-TrFE)/PMMA (30 wt%) in the thickness of 4 μm. Fig. 4-9 depicts a cross section SEM micrograph of P(VDF-TrFE)/PMMA (30 wt%) by spin coating on the Al foil. The rigid rod-like crystal structure was observed in the blend polymer dielectric film from the cross-sectional micrograph.

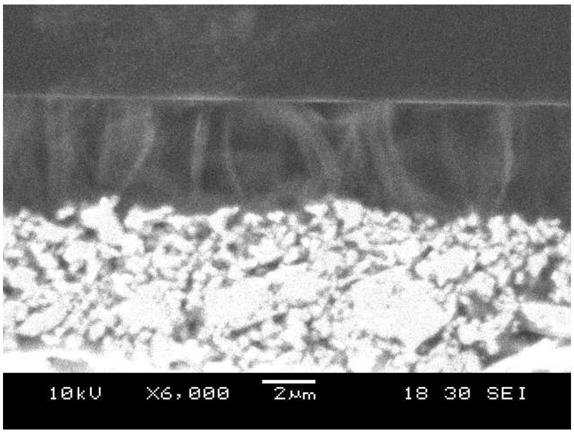

Fig. 4-9 Cross section SEM micrograph of P(VDF-TrFE)/PMMA (30 wt%)

Fig. 4-10 depicts the transfer and output characteristics of TIPs-pentacene OFETs using P(VDF-TrFE)/PMMA (10 wt%), P(VDF-TrFE)/PMMA (20 wt%), and P(VDF-TrFE)/PMMA (30 wt%) as the gate dielectrics, respectively. The device using P(VDF-TrFE)/PMMA (20 wt%) dielectric exhibited a mobility of 0.01 cm^2/Vs, comparable to that of pristine P(VDF-TrFE), which was ascribed to the similar surface morphology. As depicted in Fig. 4-10(i), TIPs-pentacene OFETs using P(VDF-TrFE)/PMMA (10 wt%) dielectric featured a mobility of 0.03 cm^2/Vs, slightly higher than that of P(VDF-TrFE)/PMMA (30 wt%), but having a larger V_T of 15 V. Fig. 4-10(iii) depicts I-V characteristics of TIPs-pentacene OFETs using P(VDF-TrFE)/PMMA (30 wt%) as the gate dielectric. The transistor exhibited a mobility of 0.02 cm^2/Vs, having an I_{on}/I_{off} of 10^4 with a V_T of 12 V. Therefore, there was a tradeoff that blending PMMA reduced the leakage current but increased the V_T, which was unfavorable for low-voltage operation.

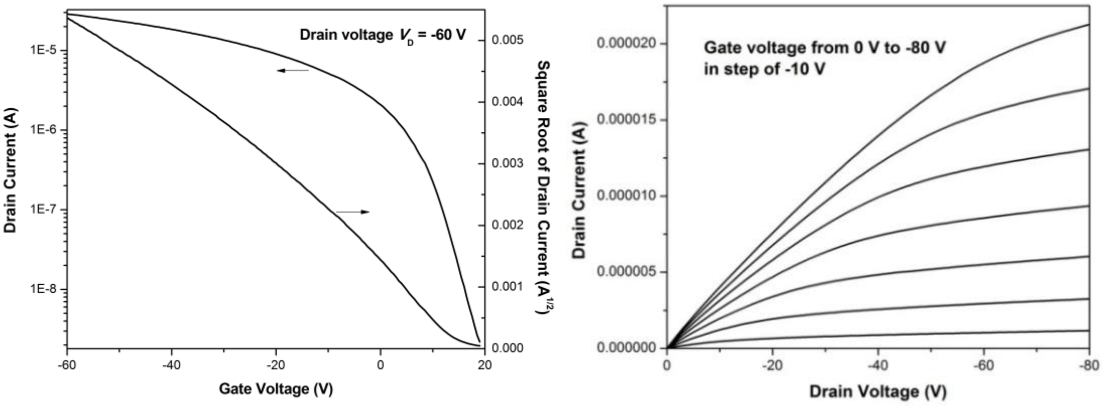
Drain voltage V_D = -60 V
Drain Current (A)
1E-5
1E-6
1E-7
1E-8
Square Root of Drain Current ($A^{1/2}$)
0.005
0.004
0.003
0.002
0.001
0.000
-60
-40
-20
0
20
Gate Voltage (V)
Gate voltage from 0 V to -80 V
in step of -10 V
Drain Current (A)
0.000020
0.000015
0.000010
0.000005
0.000000
0
-20
-40
-60
-80
Drain Voltage (V)

(a) (b)

(i)

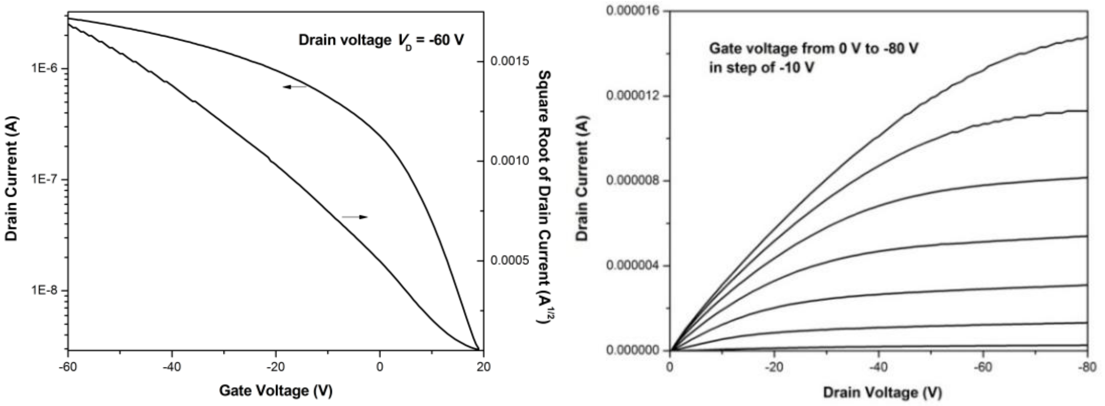
Drain voltage V_D = -60 V
Drain Current (A)
1E-6
1E-7
1E-8
Square Root of Drain Current ($A^{1/2}$)
0.0015
0.0010
0.0005
-60
-40
-20
0
20
Gate Voltage (V)
Gate voltage from 0 V to -80 V
in step of -10 V
Drain Current (A)
0.000016
0.000012
0.000008
0.000004
0.000000
0
-20
-40
-60
-80
Drain Voltage (V)

(a) (b)

(ii)

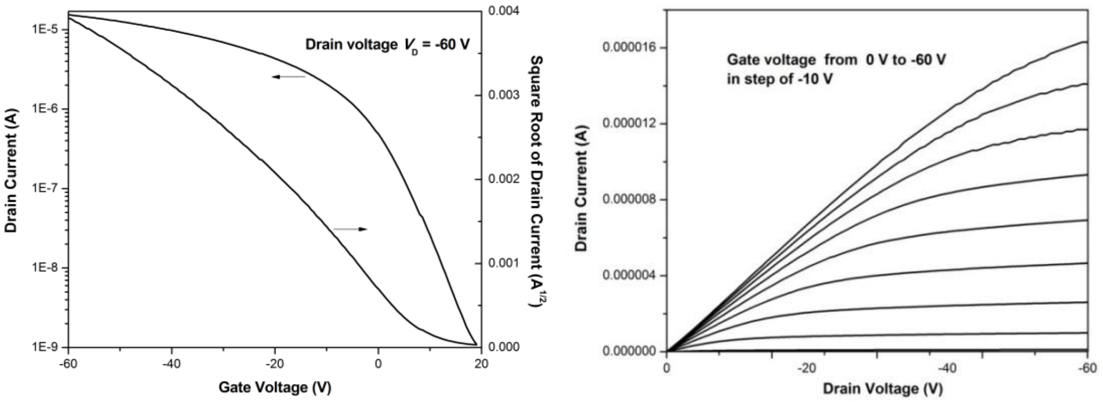

(a)

(b)

(iii)

Fig. 4-10 The transfer (a) and output (b) characteristics of TIPs-pentacene OFETs with (i) P(VDF-TrFE)/PMMA (10 wt%), (ii) P(VDF-TrFE)/PMMA (20 wt%), and (iii) PVDF-TrFE/PMMA (30 wt%) as gate dielectrics

Table 4-2 tabulates the properties of P(VDF-TrFE) blended with different concentrations of PMMA. Different dielectric layers had different dielectric thickness deposited from the solution, and the thickness of dielectric P(VDF-TrFE)/PMMA (30 wt%) was 4 μm. Pristine P(VDF-TrFE) has a dielectric constant of 8, and PMMA has a dielectric constant of 3.9. The blend polymer P(VDF-TrFE)/PMMA has a dielectric constant in between. TIPs-pentacene OFETs using P(VDF-TrFE) dielectric featured a mobility of 0.001 cm^2/Vs, having a leakage current of 10^{-8} A with an I_{on}/I_{off} of 10^3. With blending 30 wt% of PMMA, the dielectric constant was reduced by 37% to 5.0 and the leakage current of TIPs-pentacene using P(VDF-TrFE)/PMMA dielectric was reduced to 10^{-9} A, but the threshold voltage of TIPs-pentacene OFETs was enhanced. Pristine P(VDF-TrFE) has a roughness of 94.8 nm and P(VDF-TrFE)/PMMA (30 wt%) has a roughness of 54.4 nm. However, there is no direct relationship between the dielectric roughness and the mobility.

Table 4-2 Properties of P(VDF-TrFE)/PMMA and TIPs-pentacene OFETs with P(VDF-TrFE)/PMMA as gate dielectrics

PMMA (wt%)	**C (nF/cm^2)**	**R_q (nm)**	**V_T (V)**	**I_{on}/I_{off}**	**μ (cm^2/Vs)**
0	1.4	94.8	4	10^3	0.001
10	0.8	42.7	15	10^4	0.03
20	1.4	25.5	17	10^3	0.002
30	1.1	54.4	12	10^4	0.02

4.3 Polymer nanocomposite dielectric

In order to achieve high-capacitance dielectric for low-voltage operation, $BaTiO_3$ nanoparticles were dispersed into the polymer matrix of P(VDF-TrFE)/PMMA (30 wt%). The free hydroxyl groups on the surface of nanoparticles $BaTiO_3$ can form strong O-H…F-C hydrogen bonds with P(VDF-TrFE) in the blend polymer due to the high polarity, thereby inducing β-phase crystalline in the polymer matrix [151], which is unfavorable for insulating properties. $BaTiO_3$ powder (Sigma-Aldrich) was first broken by Ball Mill before use, due to high surface energy and tendency for agglomeration. In order to facilitate well dispersion of nanoparticles into the polymer matrix, silane coupling agent 3-glycidoxypropyltrimethoxysilane (GPTMS) was used for the surface modification of $BaTiO_3$ [103].

Fig. 4-11 depicts the molecular structure of GPTMS as the silane coupling agent. The alkoxysilanes react with water to be hydrolyzed and turn to silanol groups, which can bind covalently to the free –OH groups on the surface of the $BaTiO_3$ nanoparticles [105]. The organic head group of 3-glycidoxypropyl group endows functionalized nanoparticles with good thermal curability [152, 153]. Well-dispersion of $BaTiO_3$ into the polymer matrix is crucial to achieve uniformly thin polymer dielectric films. The effects of various $BaTiO_3$ loadings on the morphology and insulating properties of polymer nanocomposite dielectrics were investigated. The curie point of $BaTiO_3$ is 120 °C, which is the transition temperature between the ferroelectric and the non-ferroelectric structures, so the thermal curing temperature of polymer nanocomposite dielectric films is 120 °C, similar to that of polymer dielectric films.

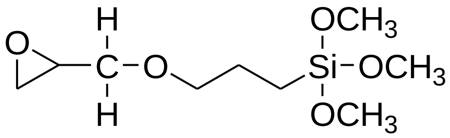

Fig. 4-11 Molecular structure of GPTMS

4.3.1 Experimental

Chemicals

Barium titanate (IV) nanopowder ($BaTiO_3$, < 100 nm particle size), and Fumed Silica powder purchased from Sigma-Aldrich.

Equipments

$BaTiO_3$ powder was broken by Ball Mill, JAR Mill 230 V YJB-10.

Surface treatment of $BaTiO_3$

First, the agglomerates of $BaTiO_3$ powder in ethanol were first broken by Ball Mill overnight. $BaTiO_3$ (1g) and GPTMS (2.325 mL) reacted in a mixture solution of ethanol (2 mL), deionized water (0.3 mL) and, HCl (0.3 mL, 0.1 M) at 80 °C overnight in the dark. The modified $BaTiO_3$ nanoparticles were subsequently collected by centrifugation at 8000 rpm for 30 min, and the resultant solid was washed by ethanol and DI water by centrifugation at 8000 rpm for 30 min, respectively. Finally, the white $BaTiO_3$ nanoparticles were dried at 40 °C overnight under vacuum.

4.3.2 Morphology of P(VDF-TrFE)/PMMA/$BaTiO_3$ dielectrics

In order to further increase the capacitance of polymer dielectrics, high-*k* $BaTiO_3$ nanoparticles modified by silane coupling agent GPTMS were dispersed into the polymer matrix P(VDF-TrFE)/PMMA (30 wt%). Table 4-3 tabulates the compositions of polymer nanocomposite dielectrics of P(VDF-TrFE)/PMMA (30 wt%) with $BaTiO_3$ loadings of 9 wt%, 16 wt%, 23 wt%, 28 wt%, and 33 wt%, respectively.

Table 4-3 Compositions of polymer nanocomposite dielectrics of P(VDF-TrFE)/PMMA/$BaTiO_3$

$BaTiO_3$ (wt%)	**P(VDF-TrFE) (g)**	**PMMA (g)**	**$BaTiO_3$ (mg)**	**NMP (mL)**
9	0.308	0.132	44	2.4
16	0.308	0.132	88	2.4
23	0.308	0.132	132	2.4
28	0.308	0.132	176	2.4
33	0.308	0.132	220	2.4

Fig. 4-12 depicts AFM topographical and phase images of P(VDF-TrFE)/PMMA with $BaTiO_3$ loadings of 9 wt%, 16 wt%, 23 wt%, 28 wt%, and 33 wt% by spin coating on the flexible substrate, respectively. The surface morphology of polymer nanocomposite dielectric films greatly varied with increased $BaTiO_3$ loadings. Compared to the blend polymer of P(VDF-TrFE)/PMMA, polymer nanocomposite dielectric films featured more compact crystal structure with a decreased diameter, because GPTMS-modified $BaTiO_3$ exhibited good miscibility with the blend polymer matrix of P(VDF-TrFE)/PMMA. As depicted in Fig. 4-12(iii), the dielectric of P(VDF-TrFE)/PMMA/$BaTiO_3$ (23 wt%) featured rigid rod-like crystal with a roughness of 94.9 nm. With addition of a high $BaTiO_3$ loading of 33 wt% depicted in Fig. 4-12(v), this typical rigid rod-like crystal structure disappeared.

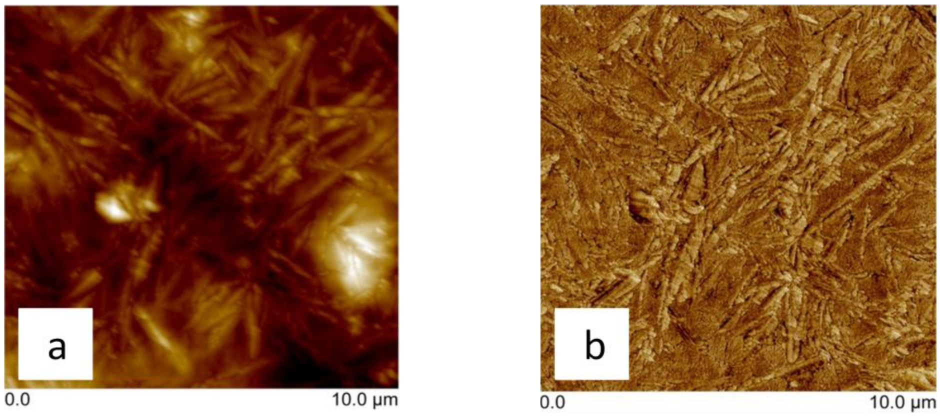

(i)

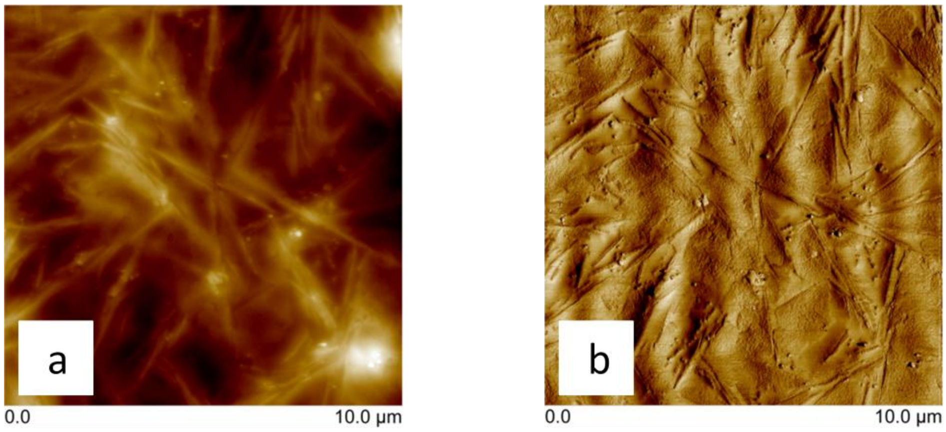

(ii)

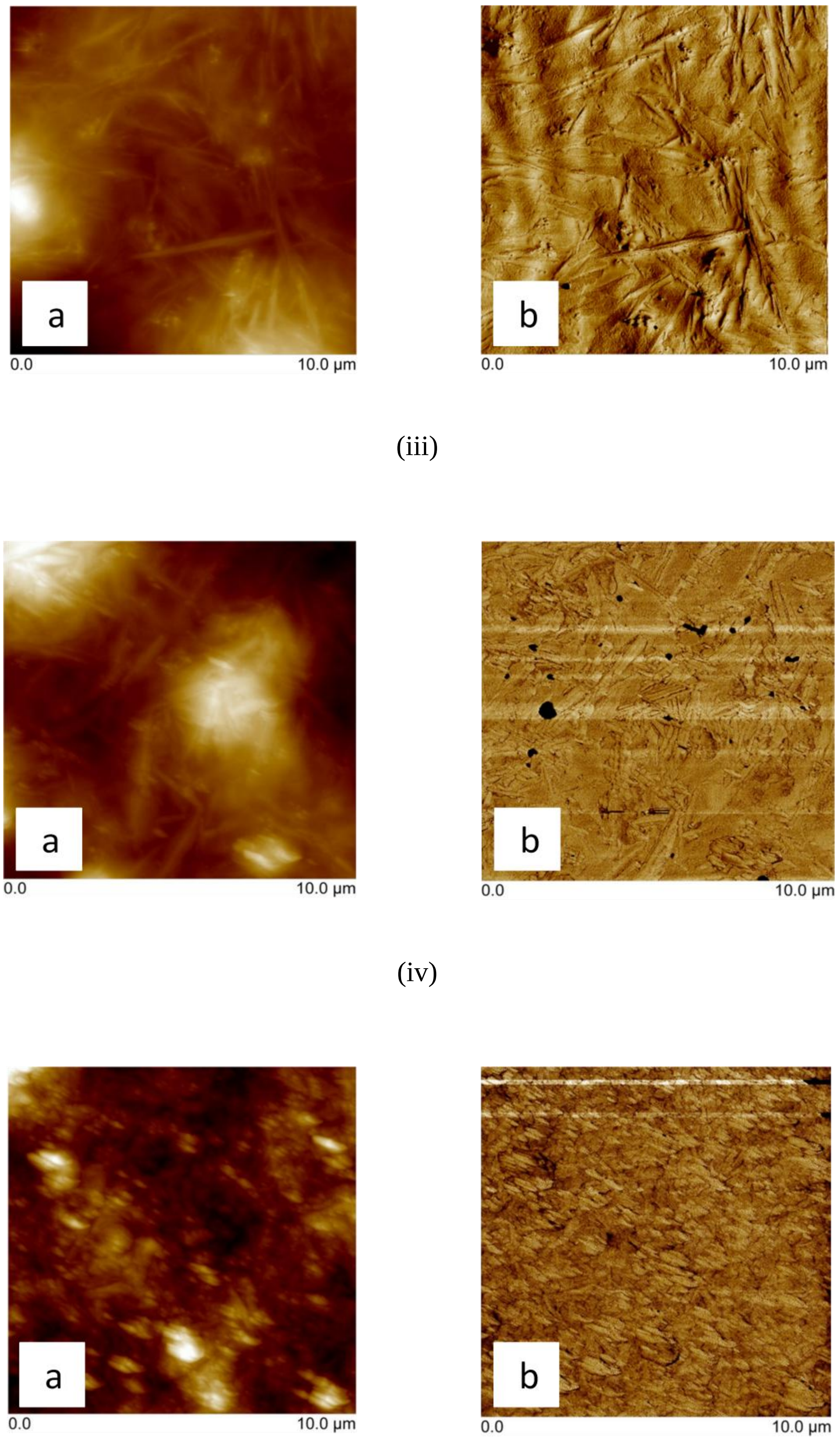

(iii)

(iv)

(v)

Fig. 4-12 AFM topographical (a) and phase (b) images of P(VDF-TrFE)/PMMA with $BaTiO_3$ loadings of (i) 9 wt%, (ii)16 wt%, (iii) 23 wt%, (iv) 28 wt%, and (v) 33 wt%

Fig. 4-13 depicts a cross section SEM micrograph of P(VDF-TrFE)/PMMA/$BaTiO_3$ (23 wt%) film by spin coating on an Al foil. It was observed that GPTMS-modified $BaTiO_3$ nanoparticles were well dispersed into the polymer matrix with a mean size of 125 nm. The thickness of the dielectric film was 6 μm and the fiber-like crystal was clearly observed from the cross-sectional micrograph of the polymer dielectric film.

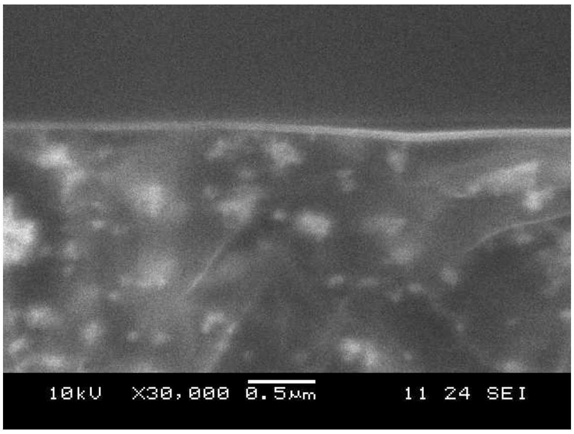

Fig. 4-13 Cross section SEM micrograph of P(VDF-TrFE)/PMMA/$BaTiO_3$ (23 wt%)

4.3.3 OFETs using P(VDF-TrFE)/PMMA/$BaTiO_3$ as gate dielectrics

Fig. 4-14 depicts the *I-V* characteristics of TIPs-pentacene OFETs with P(VDF-TrFE)/PMMA/$BaTiO_3$ as the gate dielectrics. With 23 wt% $BaTiO_3$ loading, the dielectric constant of polymer nanocomposite was increased by 86% to 9.3, compared to P(VDF-TrFE)/PMMA. As depicted in Fig. 4-14(iii), TIPs-pentacene OFETs with P(VDF-TrFE)/PMMA/$BaTiO_3$ (23 wt%) featured a mobility of 0.01 cm^2/Vs, having an I_{on}/I_{off} of 10^4 (comparable to P(VDF-TrFE)/PMMA), but having a much smaller V_T of 8.5 V.

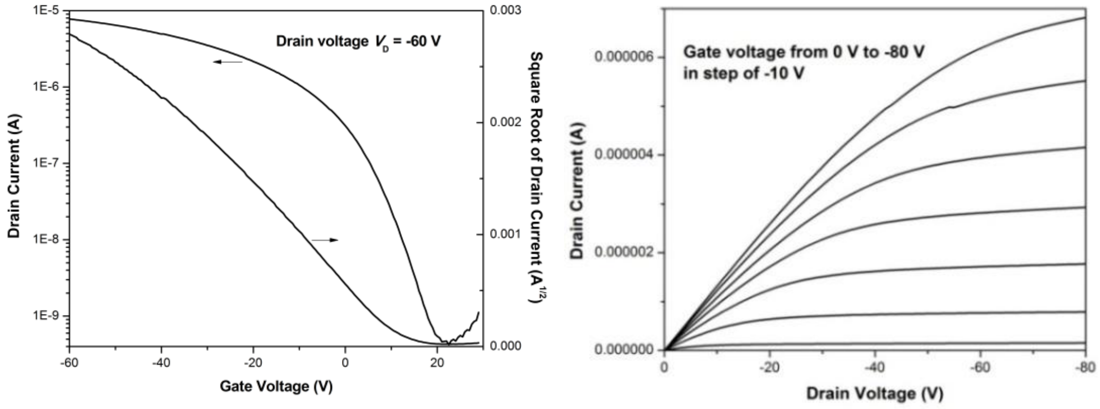

(a) (b)

(i)

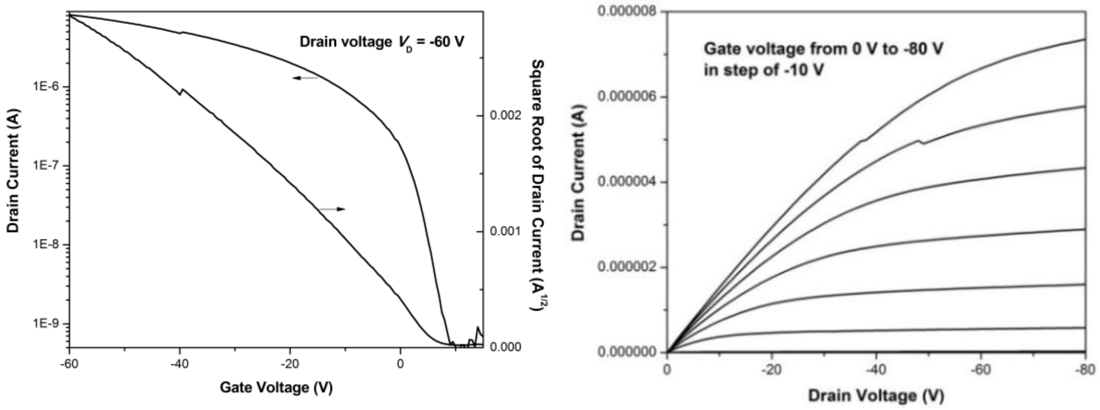

(a) (b)

(ii)

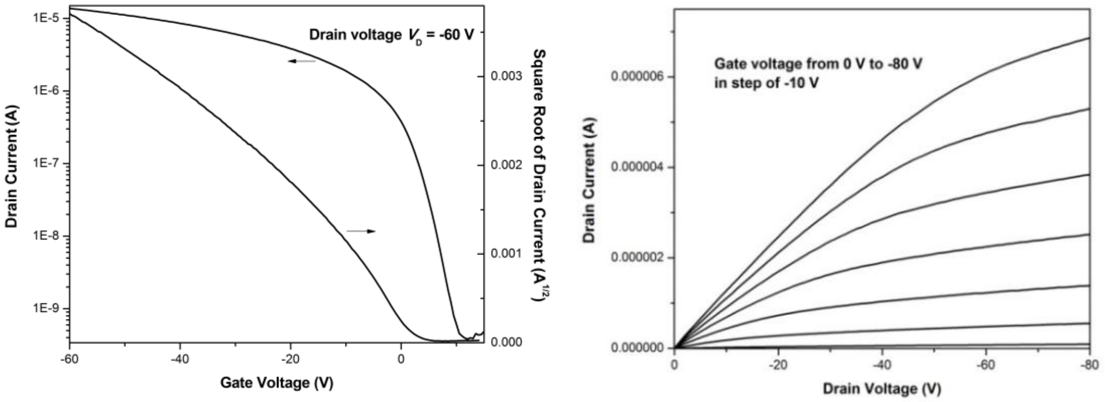

(a) (b)

(iii)

Fig. 4-14 The transfer (a) and output (b) characteristics of TIPs-pentacene OFETs with (i) P(VDF-TrFE)/PMMA/$BaTiO_3$ (9 wt%), (ii) P(VDF-TrFE)/PMMA/$BaTiO_3$ (16 wt%), and (iii) P(VDF-TrFE)/PMMA/$BaTiO_3$ (23 wt%) as gate dielectrics

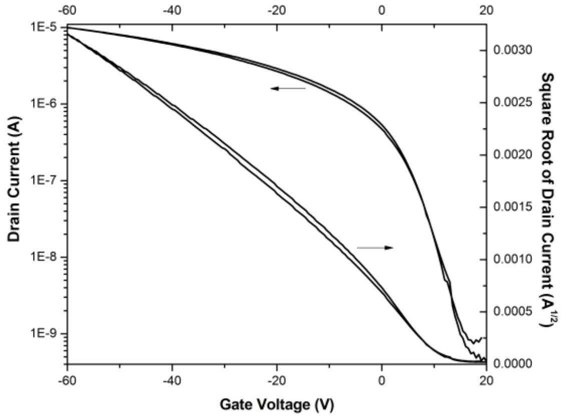

Fig. 4-15 The transfer characteristics of TIPs-pentacene OFETs with P(VDF-TrFE)/PMMA/$BaTiO_3$ (23 wt%) as the gate dielectric under dual bias sweeping

The organic semiconductor features a unique hysteresis in the *I-V* characteristics, which indicates that there is a minor influence of trapping and charging effects above the threshold voltage. As depicted in Fig. 4-15, it was observed that TIPs-pentacene OFETs with P(VDF-TrFE)/PMMA/$BaTiO_3$ (23 wt%) as the gate dielectric featured a small hysteresis under the dual bias sweeping, which could be attributed to the favorable properties of the polymer nanocomposite dielectric. First of all, the hydrophobic surface of the fluoropolymer contained a low density of electron traps such as hydroxyl groups, so little charge trapping was observed at the interface of the dielectric/semiconductor as well as in the bulk dielectric. Secondly, GPTMS-modified $BaTiO_3$ nanoparticles had a mean particle size of 125 nm, so the degree of ferroelectricity was likely to be too small to bring about the strong *I-V* hysteresis [154]. Therefore, the good electrical properties make sure that P(VDF-TrFE)-based polymer nanocomposite dielectrics are suitable for the ink formulation for PE.

With a high $BaTiO_3$ loadings of 28 wt% and 33 wt%, as depicted in Fig. 4-16 and 4-17, the transistors exhibited a comparable mobility of 0.002 cm^2/Vs, which was 10 times smaller than that of P(VDF-TrFE)/PMMA/$BaTiO_3$ (23 wt%), having a smaller I_{on}/I_{off} of 10^3. Moreover, the contact resistance was not observed in the output characteristics of OFETs, indicative of good electron injection from the PFBT-treated Ag electrodes into the active semiconductor layer.

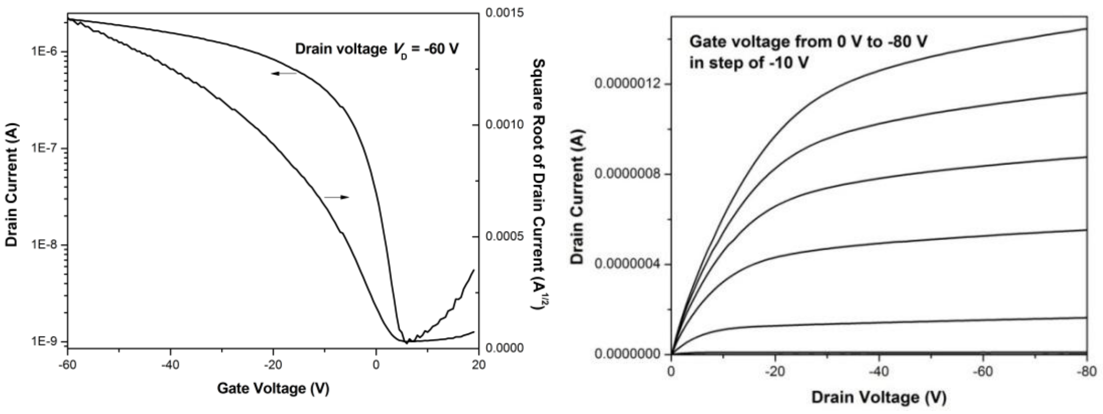

(a) (b)

Fig. 4-16 The transfer (a) and output (b) characteristics of TIPs-pentacene OFETs with P(VDF-TrFE)/PMMA/$BaTiO_3$ (28 wt%) as the gate dielectric

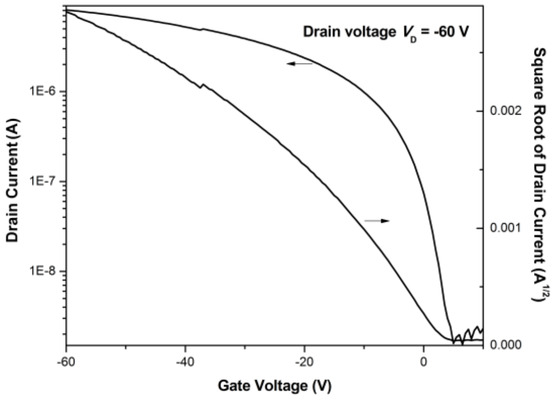

Fig. 4-17 The transfer characteristics of TIPs-pentacene OFETs with P(VDF-TrFE)/PMMA/$BaTiO_3$ (33 wt%) as the gate dielectric

Table 4-4 tabulates the properties of P(VDF-TrFE)/PMMA blended with various loadings of $BaTiO_3$ and TIPs-pentacene OFETs using P(VDF-TrFE)/PMMA/$BaTiO_3$ as the gate dielectric. As discussed in Section 4.2.3, P(VDF-TrFE)/PMMA (30 wt%) had a capacitance of 1.1 nF/cm^2, a dielectric constant of 5.0, and a V_T of 12 V. With an increase in $BaTiO_3$ loading from 9 wt% to 33 wt%, the dielectric constant of P(VDF-TrFE)/PMMA/$BaTiO_3$ dielectric film increased from 7.7 to 21, and the threshold voltage V_T decreased from 8.4 V to 3.9 V. The surface roughness increased systematically with an increase of $BaTiO_3$ loading from 9 wt% to 28 wt%, while the surface roughness decreased to 40.9 nm for the dielectric with $BaTiO_3$ loading of 33 wt%.

Table 4-4 Properties of P(VDF-TrFE)/PMMA/$BaTiO_3$ and TIPs-pentacene OFETs with P(VDF-TrFE)/PMMA/$BaTiO_3$ as gate dielectrics

$BaTiO_3$ (wt%)	**C (nF/cm^2)**	***k***	**R_q (nm)**	**V_T (V)**	**I_{on}/I_{off}**	**μ (cm^2/Vs)**
9	1.37	7.7	27.2	8.4	10^4	0.004
16	1.25	8.4	44.3	6.8	10^4	0.007
23	1.38	9.3	94.9	8.5	10^4	0.01
28	1.52	10.3	99.4	4.4	10^3	0.002
33	3.8	21	40.9	3.9	10^3	0.002

4.4 OFETs using printable dielectrics on an Al foil

Screen printable dielectric materials of P(VDF-TrFE)/PMMA/Silica (PPS) and P(VDF-TrFE)/PMMA/$BaTiO_3$/Silica (PPBS) were first formulated for fully-additive printed TIPs-pentacene OFETs fabrication on Al foils. In the ink composition, fumed silica as the viscosity modifier is crucial for the printability and flowing property of the dielectric ink, but the optimum concentration remains unclear at the beginning.

Fumed silica, or called fumed silicon dioxide, is composed of submicron-sized sphere, which are 40-60% fused into short chains, very highly branched, 0.1-0.2 microns. Fumed silica will form dispersions in water, glycerine, butyl alcohol, mineral oil and a variety of other liquids, causing the them to thicken or form gels. Moreover, dispersions formed with fumed silica are quite stable, remaining unchanged for weeks to months.

Table 4-5 tabulates the compositions of polymer nanocomposite dielectric inks for spin coating and screen printing. The two screen-printable dielectric inks of PPS and PPBS were formulated by adding the fumed silica with concentration of 23 wt% and 18 wt% into P(VDF-TrFE)/PMMA (7:3) and P(VDF-TrFE)/PMMA/$BaTiO_3$ (23 wt%), respectively.

Table 4-5 Compositions of polymer nanocomposite dielectrics on an Al foil

Dielectric	**P(VDF-TrFE) (g)**	**PMMA (g)**	**$BaTiO_3$ (g)**	**Silica (g)**	**NMP (mL)**
P(VDF-TrFE)/PMMA (7:3)	0.308	0.132			2.4
P(VDF-TrFE)/PMMA/$BaTiO_3$	0.308	0.132	0.132		2.4
PPS	0.308	0.132		0.132	2.4
PPBS	0.308	0.132	0.132	0.132	2.4

The surface morphology of screen-printed dielectric films on Al foils was measured by the tapping mode AFM. Fig. 4-18 depicts the AFM topographical and phase images of the dielectric films of PPS and PPBS deposited by screen printing on Al foils, respectively. The surface morphology of screen-printed dielectric films was dramatically different from that of the spin-coated ones, because the spherical structure were preferentially formed instead of the rod-like crystal structure due to the patterns on the mask used for screen printing.

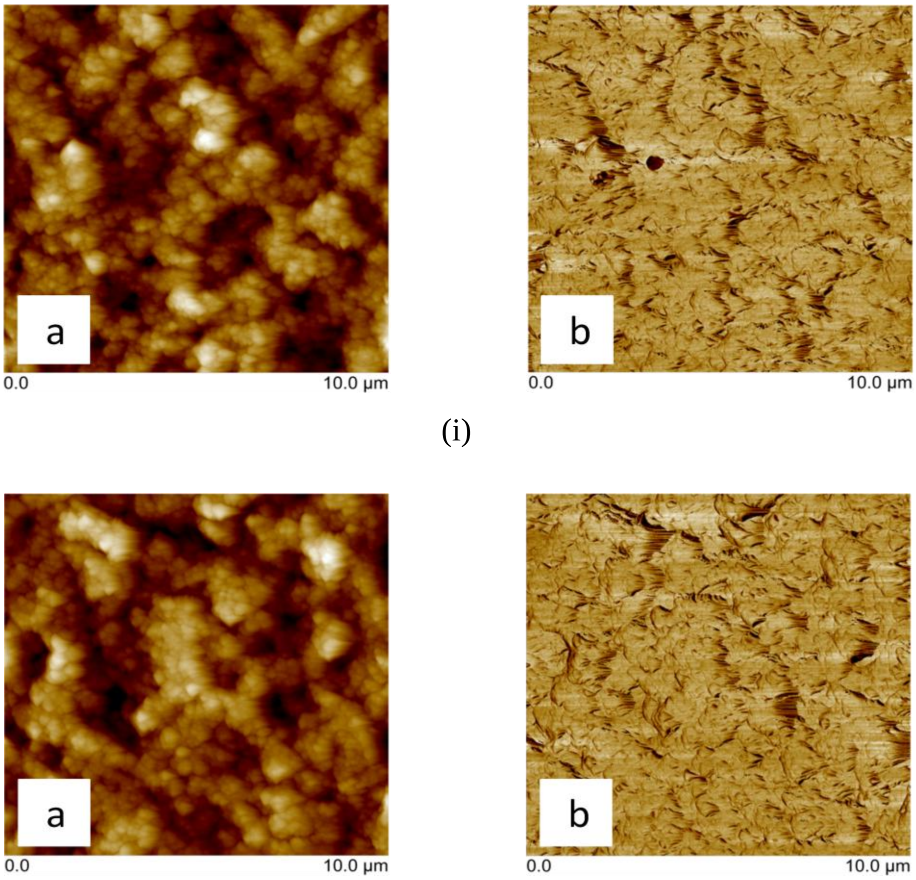

(i)

(ii)

Fig. 4-18 AFM topographical (a) and phase (b) images of the dielectrics of (i) PPS, and (ii) PPBS

Fig. 4-19 depicts the cross section SEM micrograph of the dielectric PPBS by screen printing on an Al foil. It was observed that $BaTiO_3$ nanoparticles with a mean size of 125 nm, were well dispersed into the polymer matrix. The thickness of the screen-printed dielectric film was 3.5 μm, thinner than spin-coated ones. The thickness of the source and drain electrodes was 6 μm, which was deposited by screen printing on the dielectric layer.

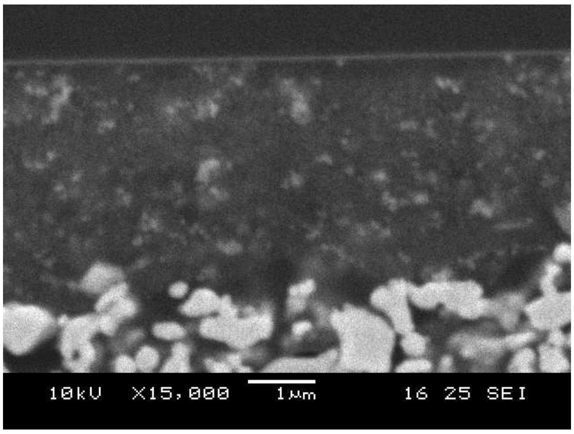

Fig. 4-19 Cross section SEM micrograph of the dielectric PPBS on an Al foil

Fig. 4-20 depicts the transfer and output characteristics of TIPs-pentacene OFETs using PPS and PPBS as the gate dielectrics, respectively. Although the dielectric PPS could be deposited by screen printing, the gate leakage current of TIPs-pentacene OFETs using dielectric PPS was increased to 10^{-8} A under a high gate bias. The transistor using dielectric PPS featured a mobility of 0.006 cm^2/Vs, having a V_T of 3 V and a I_{on}/I_{off} of 10^3. In comparison, the transistor using dielectric PPBS exhibited not only a slightly higher mobility of 0.01 cm^2/Vs, but also having larger I_{on}/I_{off} of 10^4 and a smaller V_T of 2 V. The gate leakage current of the transistor using the dielectric PPBS was reduced and remained at 10^{-9} A even under a high gate bias. Moreover, the threshold voltage of the transistor using screen-printed dielectric ink was reduced compared to that of the spin-coated counterpart. Consequently, this screen-printable, high-capacitance dielectric ink is promising for low-operating-voltage fully-additive printed OFETs.

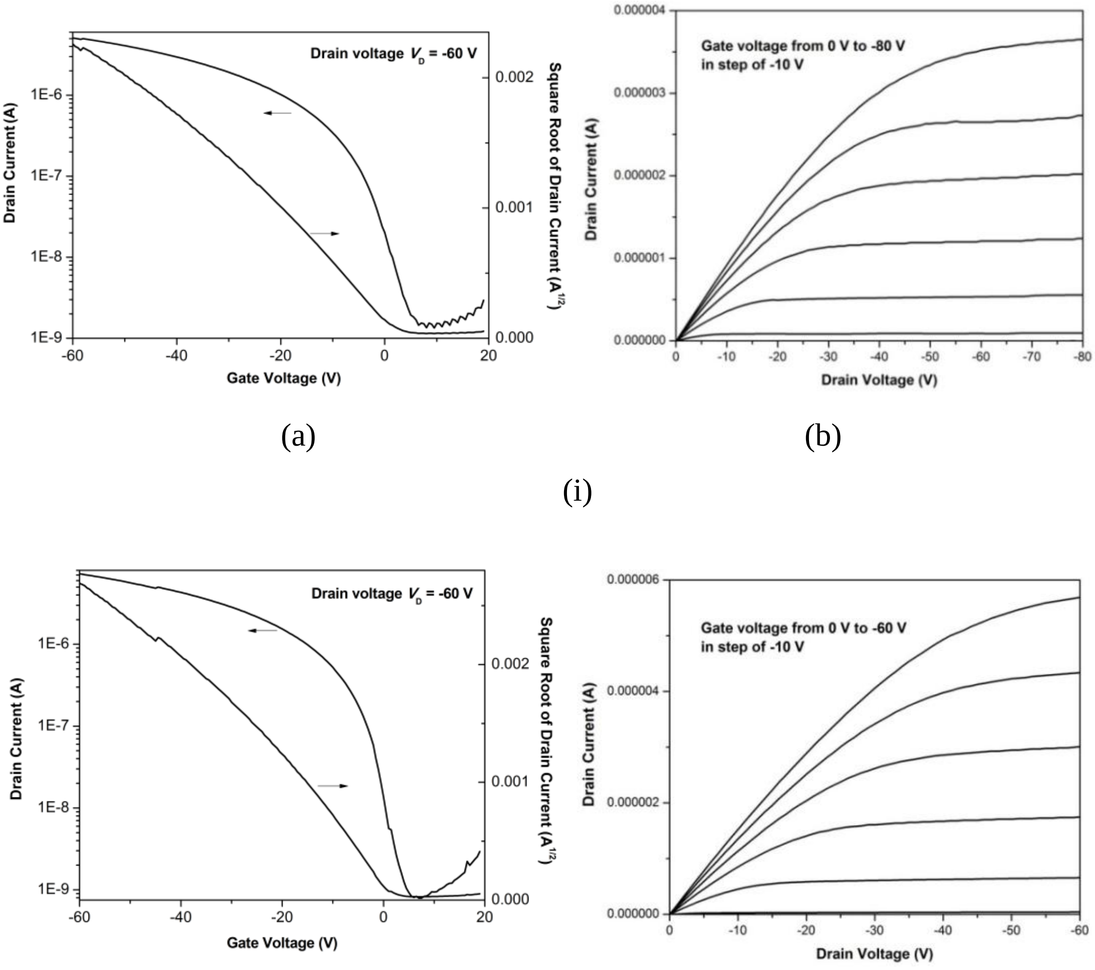

(a) (b)

(i)

(a) (b)

(ii)

Fig. 4-20 The transfer (a) and output (b) characteristics of TIPs-pentacene OFETs using (i) the dielectric PPS, and (ii) the dielectric PPBS

Table 4-6 tabulates the properties of dielectric films deposited from PPS and PPBS and TIPs-pentacene OFETs with PPS and PPBS as the gate dielectrics. Fumed Silica as the viscosity modifier was crucial for the printability of the dielectric ink, but the dielectric constant might be slightly reduced. As discussed in Section 4.3.3, P(VDF-TrFE)/PMMA/$BaTiO_3$ (23 wt%) deposited by spin coating exhibited a dielectric constant of 9.3, having a capacitance of 1.38 nF/cm^2, with a film thickness of 6 μm. Compared to the spin-coated dielectric, the dielectric constant of PPBS was slightly reduced by 6% to 8.7, the capacitance was conversely substantially increased by 59% to 2.2 nF/cm^2. This can be attributed to the much thinner dielectric film of 3.5 μm by screen printing.

Eventually, the dielectric PPS is screen printable on an Al foil having a dielectric constant of 6.7. With the addition of $BaTiO_3$, the dielectric constant of the dielectric PPBS was increased to 8.7. The roughness of screen-printed dielectric films was typically higher than that of the spin-coated ones, with the dielectric PPS of 122 nm and the dielectric PPBS of 140 nm. The dielectric PPS and dielectric PPBS featured small positive threshold voltages of 3 V and 2 V, respectively.

Table 4-6 Properties of dielectrics of PPS and PPBS and TIPs-pentacene OFETs using dielectrics of PPS and PPBS

Ink	C (nF/cm^2)	k	R_q (nm)	V_T (V)	I_{on}/I_{off}	μ (cm^2/Vs)
PPS	1.7	6.7	122	3	10^3	0.006
PPBS	2.2	8.7	140	2	10^4	0.01

4.5 Conclusions

In the polymer nanocomposite dielectric, the amorphous PMMA has been blended into P(VDF-TrFE) to tune the morphology of the surface and bulk dielectric film, thereby reducing the amount of ferroelectric crystalline to avoid hysteresis. As a tradeoff, low-*k* PMMA reduced the capacitance that was unfavorable for low-voltage operation. Modified nanoparticles $BaTiO_3$ have been incorporated into the polymer binder as the ceramic filler. Due to its small particle size, there was a small degree of ferroelectric properties of $BaTiO_3$ to cause hysteresis. With high loading of $BaTiO_3$, the leakage current of OFETs was low even under high bias operating condition. Compared to OFETs using the spin-coated dielectrics, the screen-printed transistors exhibited a comparable mobility of 0.01 cm^2/Vs, but featured a substantially smaller positive V_T of 2 V, which was attributed to higher capacitance resulting from a much thinner dielectric film. The device performance can be improved by optimization of the ink formulation and device fabrication.

Chapter 5 Formulation of Printable Dielectrics for Fully-Additive PE

5.1 Introduction

This chapter delineates the author's research work pertaining to the formulation of printable dielectrics for fully-additive PE on plastic substrates; in Chapter 4, the dielectric was partially printable and limited to application to Al foils. A large part of this chapter is extracted from the author's publication [37] published in the Royal Society of Chemistry (RSC) Advances journal.

Fully-additive (vis-à-vis subtractive) printed electronics (PE) [15] have attracted much interest within the PE community. The device mobility of fully-additive printed transistors is in the range which is automatically lower than that of silicon-based transistors [26, 65]. Whilst low mobility is a limitation of PE, it is largely complementary to silicon-based electronics, because of its advantages such as low-cost and solution-processable device fabrication. Being able to obtain high capacitance for organic field-effect transistors (OFETs) is important to achieve improving frequency, low operating voltage, and efficient device scalability. The high capacitance can be achieved by using high permittivity dielectric insulator or thin dielectric films. In PE, polymer nanocomposite dielectric materials [102] have attracted much attention because they can meet the requirements of good solution processability and mechanical properties of polymers combined with unique electrical properties of nanoparticles. Among all the polymer matrices, PVDF-based fluoropolymers have the advantages of high capacitance, high stability, and good water repellency. However, they have the disadvantages of the leakage current and ferroelectric loss under a high electric field due to low volume resistivity. This problem can be overcome by control of fluoropolymer chain conformation or by blending polymers with high volume resistivity into the fluoropolymer.

A novel screen-printable polymer nanocomposite dielectric ink was successfully formulated for fully-additive printed OFETs fabrication. This dielectric ink was composed of poly(vinylidenefluoride-co-trifluoroethylene) (P(VDF-TrFE)) and poly(methyl methacrylate) (PMMA) blend as the polymer binder, $BaTiO_3$ as the ceramic fillers and fumed silica as the viscosity modifier. The surface of the blend polymer contained low density electron traps such as hydroxyl groups, so little charge trapping was observed at the interface of the dielectric/semiconductor as well as in the bulk dielectric. High-*k* $BaTiO_3$ nanoparticles was incorporated into the polymer matrix in order to achieve high capacitance. Moreover, the contribution of the ferroelectric nature of the $BaTO_3$ to hysteresis is negligible due to its small particle size.

5.2 Experimental

Chemicals

Fumed Silica powder (0.007 μm) procured from Sigma-Aldrich.

Equipments

The viscosity was measured by Brookfield Viscometer DV-II+ Pro, Spindle CPE-40, 0.3 rpm, 25 °C. The silver source and drain electrodes of transistor device were deposited by Dek 265 Horizon Auto Stencil Printer. The screen printing masks were fabricated by SCREENTEC, with the mesh No. SS400, mesh angle of 45° and mesh tension of 23’’, and emulsion thickness of 30 μm.

Device Fabrication by Screen Printing

Fully-additive printed devices were fabricated on PET substrates. Silver paste (DuPont 5028) was screen printed on PET substrates with a speed of 100 mm/s and a pressure of 12 kg, and was subsequently cured at 120 °C for 10 min. The formulated dielectric ink was deposited by screen printing with a printing speed of 60 mm/s and a pressure of 8.0 kg for the first time, and cured at 120 °C for 30 min, and then printed under the same condition for the second time and cured at 120 °C for 2 h.

The source and drain electrodes were screen printed on the dielectric layer with a speed of 90 mm/s and a pressure of 11 kg, and subsequently cured at 120 °C for 10 min. All the printed transistors were cleaned by isopropanol (IPA) and deionized water to remove the contaminants, which were dried at 50 °C for 30 min under vacuum. Subsequently, the transistors were treated by PFBT in ethanol solution (1.4 μL in 1 mL) for 1 h, cleaned with ethanol and then dried at 50 °C for 30 min under vacuum. TIPs-pentacene in a mixture of toluene and anisole solution (80 mg in 2.4 mL/0.6 mL) was deposited by slot die coating, with a speed of 0.3 mm/s at a substrate temperature of 70 °C, and subsequently annealed at 90 °C for 30 min on a hot plate. All the OFETs characteristics were measured under ambient conditions. All OFETs have an aspect width/length ratio of 40,000 μm:100 μm.

5.3 OFETs using bilayer gate dielectrics

One of the requirements of dielectric materials in PE is the compatibility with the flexible substrates. As discussed in Section 4.4, TIPs-pentacene OFETs using P(VDF-TrFE)/PMMA/BaTiO$_3$/Silica (PPBS) as the gate dielectric on Al foils featured good device performance with a small positive threshold voltage. However, the dielectric film cracked on the polyethylene terephthalate (PET) substrate after the thermal curing, as depicted in Fig. 5-1. Preliminarily, the crystal structure of the polymer matrix was considered as the reason for the dielectric film cracking. In order to solve this problem, the alternative was to explore a buffer layer based on amorphous polymer nanocomposite of PMMA/$BaTiO_3$/Silica using amorphous PMMA as the polymer matrix. To simplify the device fabrication, the electrical properties of the bilayer polymer nanocomposite dielectrics were measured on the Al foil instead of on the PET substrate.

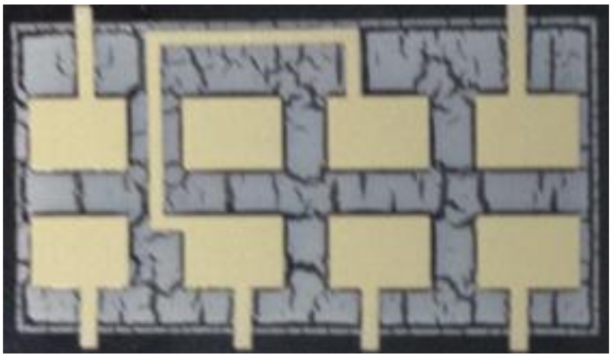

Fig. 5-1 Cracked dielectric film on PET after thermal curing

Fig. 5-2 depicts the cross section of bottom-gate bottom-contact OFETs using the bilayer dielectrics, which consist of the buffer layer of polymer nanocomposite PMMA/$BaTiO_3$/Silica and the top layer of the dielectric PPBS. The buffer layer of polymer nanocomposite PMMA/$BaTiO_3$/Silica was first deposited on an Al foil by screen printing, followed by the dielectric layer PPBS. DuPont 5028 Ag paste was deposited as source and drain electrodes by screen printing. In the case of ink formulation, the effects of the concentration of fumed silica and the loading of $BaTiO_3$ on the bilayer dielectric properties and OFETs characteristics were investigated.

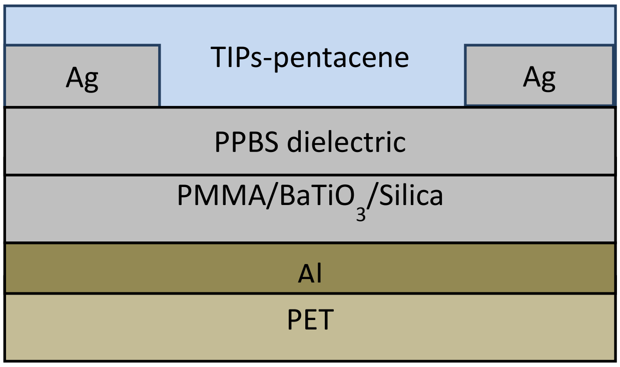

Fig. 5-2 Schematic cross section of BGBC OFETs using the bilayer dielectric

Table 5-1 tabulates the composition of the buffer dielectric ink of PMMA/$BaTiO_3$/Silica with different concentrations of $BaTiO_3$ and fumed silica. The composition of P(VDF-TrFE)/PMMA/$BaTiO_3$/Silica (PPBS) and the modification of $BaTiO_3$ nanoparticles by the silane coupling agent GPTMS were delineated in Chapter 4, and the fumed silica was used without any treatment. When a large amount of fumed silica (21 wt%) was added to the dielectric B2, the screen-printed dielectric film cracked on the PET substrate. The optimized dielectric B4 has the highest loading of $BaTiO_3$ (23 wt%) and the lowest concentration of fumed silica (7 wt%). Eventually, the dielectric B4 can form smooth and pinhole-free dielectric films both on the PET substrate and the Al foil substrate without cracking.

Table 5-1 Compositions of the buffer dielectric layers of PMMA/$BaTiO_3$/Silica

Ink	**PMMA (g)**	**Silica (mg)**	**$BaTiO_3$ (mg)**	**NMP (mL)**
B1	0.51	52	24	1.2
B2	0.51	156	72	1.2
B3	0.51	104	120	1.2
B4	0.51	52	168	1.2

With an increase of $BaTiO_3$ loading, the capacitance of dielectric films was increased and the operating voltage and the threshold voltage of OFETs were likely to be reduced. On one hand, the viscosity of dielectric ink was reduced by the addition of $BaTiO_3$, because the surface modifier of GPTMS on $BaTiO_3$ enhanced the miscibility with the polymer matrix. On the other hand, fumed silica endowed the dielectric ink with good viscosity and printability, but there was a tradeoff that the capacitance of dielectric films was slightly reduced. Moreover, too high concentration of fumed silica in the dielectric ink destroyed the compatibility of dielectric films with the plastic substrate. Consequently, the loading of $BaTiO_3$ and the concentration of fumed silica should be optimized to achieve good electrical properties and printability, which are crucial for the ink formulation of polymer nanocomposite dielectric.

Fig. 5-3 depicts the I-V characteristics of TIPs-pentacene OFETs using the bilayer dielectric films as the gate dielectric. The transistors featured a mobility of 0.01 cm^2/Vs comparable to that of the device using dielectric PPBS, except the device using the bilayer dielectric of PPBS on B1. As depicted in Fig. 5-3(iv), TIPs-pentacene OFETs using the bilayer dielectric of PPBS on B4 as the gate dielectric featured a mobility of 0.01 cm^2/Vs, having a V_T of 3 V.

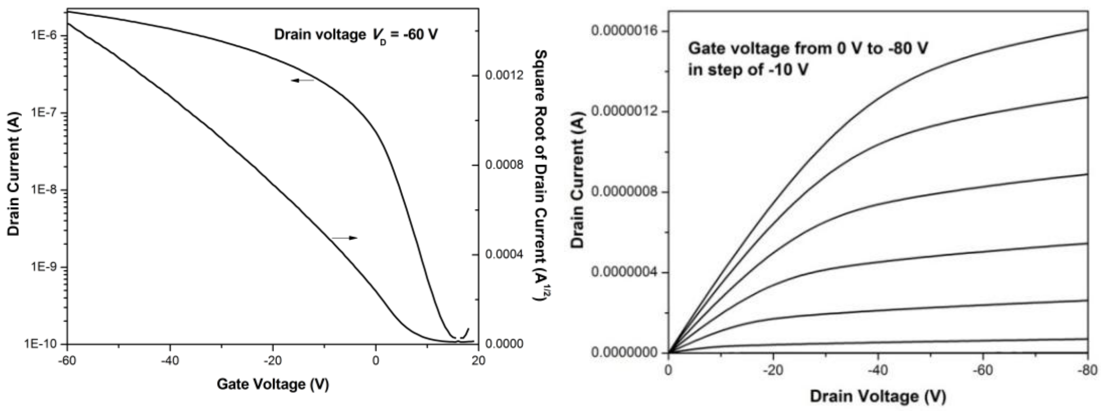
Drain voltage V_D = -60 V
Drain Current (A)
Square Root of Drain Current ($A^{1/2}$)
Gate Voltage (V)
1E-6
1E-7
1E-8
1E-9
1E-10
0.0012
0.0008
0.0004
0.0000
-60
-40
-20
0
20
Gate voltage from 0 V to -80 V
in step of -10 V
Drain Current (A)
Drain Voltage (V)
0.0000016
0.0000012
0.0000008
0.0000004
0.0000000
0
-20
-40
-60
-80

(a) (b)

(i)

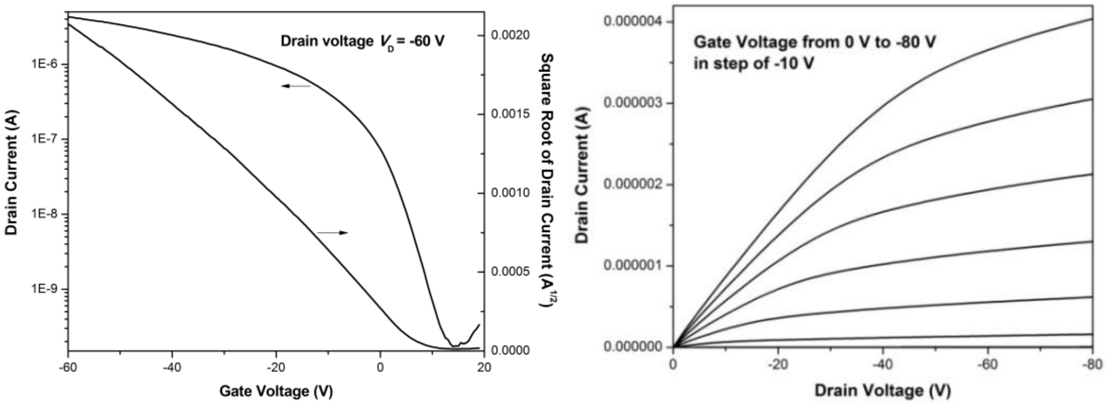
Drain voltage V_D = -60 V
Drain Current (A)
Square Root of Drain Current ($A^{1/2}$)
Gate Voltage (V)
1E-6
1E-7
1E-8
1E-9
0.0020
0.0015
0.0010
0.0005
0.0000
-60
-40
-20
0
20
Gate Voltage from 0 V to -80 V
in step of -10 V
Drain Current (A)
Drain Voltage (V)
0.000004
0.000003
0.000002
0.000001
0.000000
0
-20
-40
-60
-80

(a) (b)

(ii)

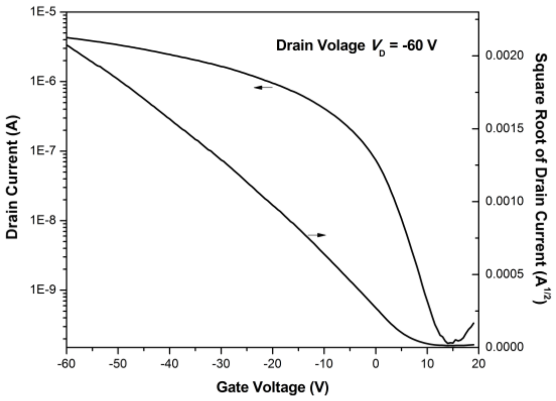
Drain Volage V_D = -60 V
Drain Current (A)
Square Root of Drain Current ($A^{1/2}$)
Gate Voltage (V)
1E-5
1E-6
1E-7
1E-8
1E-9
0.0020
0.0015
0.0010
0.0005
0.0000
-60
-50
-40
-30
-20
-10
0
10
20

(iii)

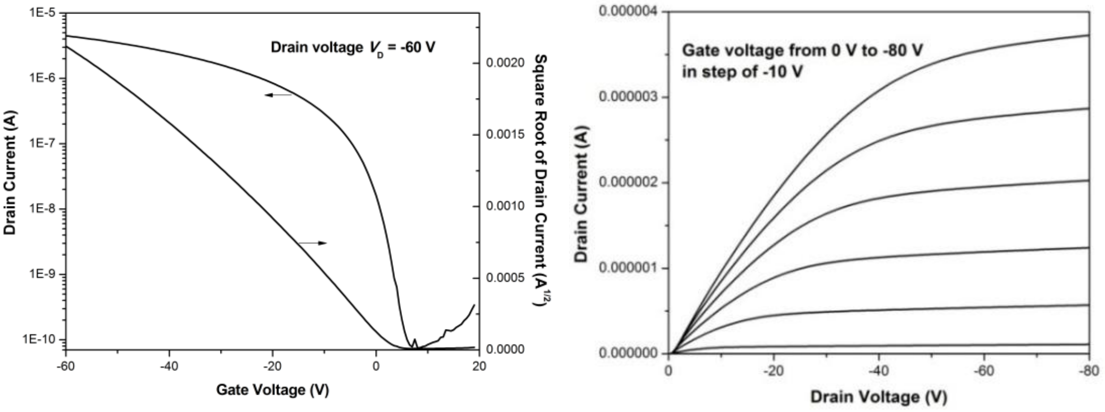

(a) (b)

(iv)

Fig. 5-3 The transfer (a) and output (b) characteristics of TIPs-pentacene OFETs using the bilayer dielectrics of (i) PPBS on B1, (ii) PPBS on B2, (iii) PPBS on B3, and (iv) PPBS on B4

Table 5-2 tabulates the properties of screen-printed bilayer dielectric materials and TIPs-pentacene OFETs. The buffer dielectric layer comprised of the amorphous low-*k* polymer nanocomposite of PMMA/$BaTiO_3$/Silica (B1, B2, B3 and B4), and the top dielectric layer was the high-*k* polymer nanocomposite based on PPBS. Compared to the capacitance of the single dielectric layer of PPBS (2.2 nF/cm^2), the capacitance of bilayer dielectric PPBS on B1 was dramatically reduced to 0.5 nF/cm^2 due to low-*k* buffer dielectric layer. However, with an increase in the loading of $BaTiO_3$ in buffer layers from B1 (4 wt%) to B4 (23 wt%), the capacitance of bilayer dielectric was slightly increased from 0.5 nF/cm^2 to 0.61 nF/cm^2, and the threshold voltage of the transistor was decreased from 9 V to 3 V. Consequently, the polymer matrix played a significant role in the insulating properties of the polymer nanocomposite dielectric.

Table 5-2 Properties of TIPs-pentacene OFETs using the bilayer dielectrics

Dielectric	***C* (nF/cm^2)**	***μ* (cm^2/Vs)**	**V_T (V)**
PPBS	2.2	0.01	2
PPBS on B1	0.5	0.003	9
PPBS on B2	0.5	0.01	7
PPBS on B3	0.58	0.01	8
PPBS on B4	0.61	0.01	3

As depicted in Fig. 5-4, with an increase in $BaTiO_3$ loading from B1 to B4 in the buffer dielectric layer, there was a simultaneous increase in the *I-V* hysteresis. With high $BaTiO_3$ loading of 23 wt% in B4, the transistor featured a severe anticlockwise hysteresis under dual bias sweeping, which was attributed to strong charge injection and trapping in the bulk dielectric. As previously discussed in Chapter 4, the contribution of the ferroelectric nature of the $BaTiO_3$ to the hysteresis should not be considered, due to the small mean particle size of $BaTiO_3$ [154]. Consequently, the origin of the hysteresis might be attributed to the dipole groups of free hydroxyl groups in a much thicker bilayer dielectric film, which can be slowly reoriented by an applied electric field [155].

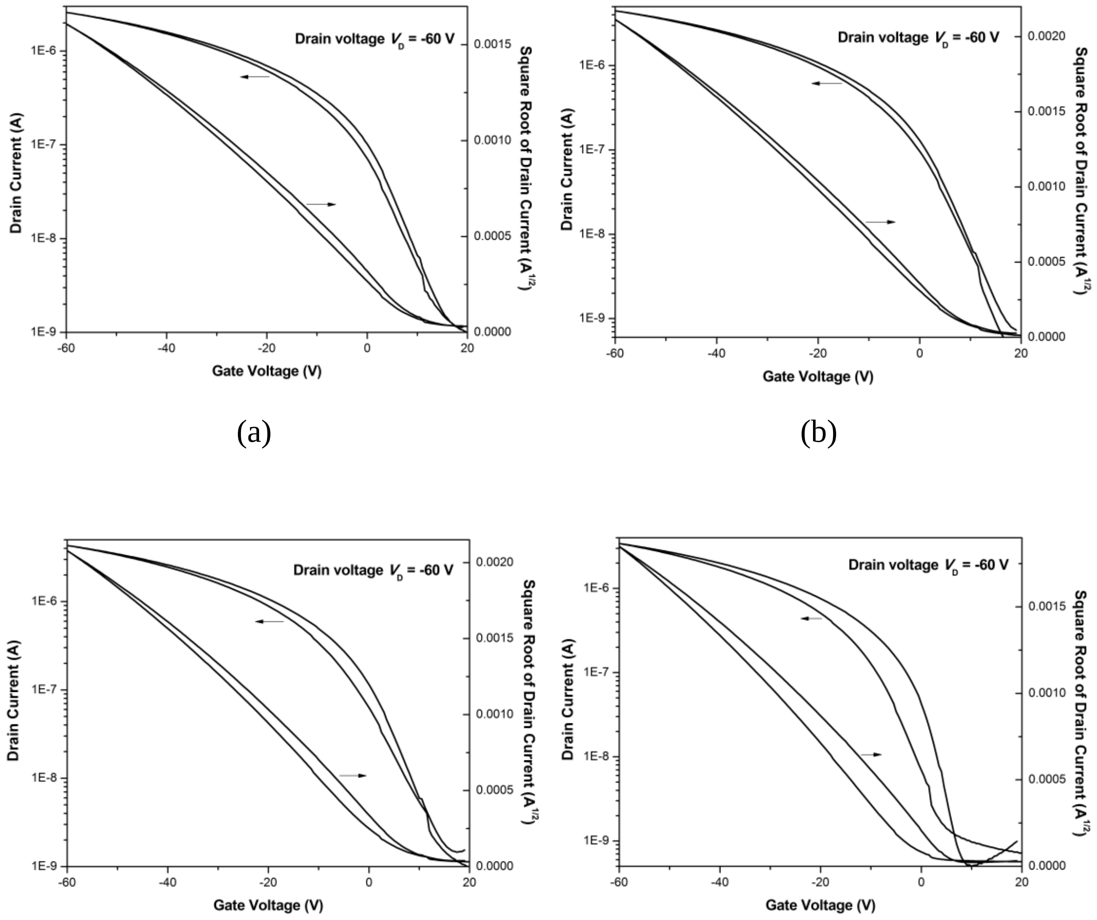

(a) (b)

(c) (d)

Fig. 5-4 The transfer characteristics of TIPs-pentacene OFETs using the bilayer dielectrics of (a) PPBS on B1, (b) PPBS on B2, (c) PPBS on B3, and (d) PPBS on B4 under dual bias sweeping

In conclusion, the bilayer gate dielectrics have been explored to investigate the effects of the buffer layer and the top layer dielectric on dielectric properties and on TIPs-pentacene OFETs characteristics. The transistor mobility greatly depended on the top dielectric layer, whereas the buffer layer slightly influenced the mobility of the TIPs-pentacene OFETs, because the charge transport occurred at the interface of the top dielectric layer and the semiconductor layer. The low-*k* buffer layer dramatically influenced the threshold voltage and the operating voltage of the transistors, which was unfavorable for the fabrication of low-operating-voltage OFETs. In addition, the concentration of the viscosity modifier should be optimized to make good compatibility between the dielectric layer and the PET substrate, and to achieve appropriate ink viscosity for screen printing.

5.4 Fully-additive printed OFETs

Fully-additive printed bottom-gate bottom-contact (BGBC) OFETs were fabricated by screen printing on the PET substrate, as depicted in Fig. 5-5. We also explored the top-gate devices, in which the molecular ordering of TIPs-pentacene on the surface of the PET substrate was dramatically different from that on the dielectric layer in the BGBC devices. PFBT-treated Ag electrodes in the BGBC devices could induce the crystal growths of TIPs-pentacene across the transistor channel, thereby improving the device performance. From the perspective of processing, the BGBC devices are much easier to be fulfilled, whereby the gate electrodes, the dielectric layer and the source/drain electrodes were deposited by screen printing, with the semiconductor layer deposited by slot die coating. In order to protect the active semiconductor layer from being exposed to air, we usually exploit an encapsulation layer to cover the fulfilled devices. As a matter of fact, the mechanical flexibility of fully-additive printed OFETs needs to be measured under different bending conditions. Due to the limitations of equipments in this research work, all the electrical measurements of fully-additive printed OFETs were measured on the flat, flexible substrate with an infinite bending radius of curvature.

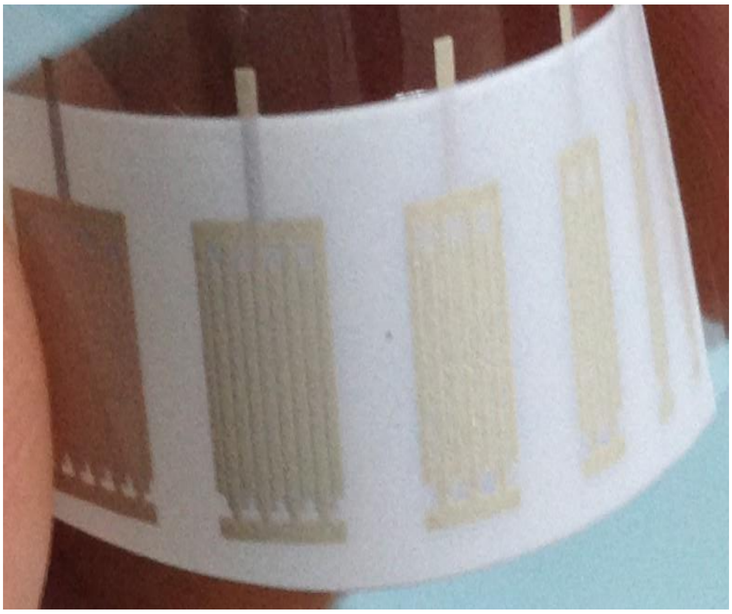

Fig. 5-5 Photo of fully-additive printed OFETs on a PET substrate

Based on the results delineated in Section 4.4 and Section 5.3, the composition of printable dielectric inks was optimized for screen printing on a PET substrate. Table 5-3 tabulates the optimized ink formulation of polymer nanocomposite dielectrics of P(VDF-TrFE)/PMMA/Silica (S1) and P(VDF-TrFE)/PMMA/$BaTiO_3$/Silica with $BaTiO_3$ loadings of 22 wt% (S2), 36 wt% (S3), and 52 wt% (S4), respectively. Pristine P(VDF-TrFE) (0.308 g) blended with PMMA (0.132 g) was dissolved in the solvent of NMP (1 mL). Surface-modified $BaTiO_3$ (22 wt%, 36 wt%, and 52 wt%) was separately suspended in NMP (0.6 mL). Following that, the two solutions were sufficiently mixed and stirred overnight. The viscosity modifier of fumed silica (3-8 wt%) was subsequently added to increase the viscosity and endow good flowing properties of the dielectric ink. It was noted that the concentration of fumed silica in the dielectric ink was reduced from PPS (23 wt%) and PPBS (18 wt%) to S1 (8 wt%)

and S2 (5 wt%), S3 (4 wt%), and S4 (3 wt%). The optimized dielectric ink could form good smooth and pinhole free films on a PET substrate deposited by screen printing. The viscosity of dielectric S1, S2, S3, and S4 was 11 Pa.s, 11 Pa.s, 14 Pa.s, and 15 Pa.s, respectively. Moreover, the dispersions formed with fumed silica were quite stable, remaining unchanged for months.

Table 5-3 Compositions of screen printable polymer nanocomposite dielectrics

Ink	P(VDF-TrFE) (g)	P(MMA) (g)	$BaTiO_3$ (g)	Silica (mg)	NMP (mL)	Viscosity (Pa.s)
S1	0.308	0.132		40	1.6	11
S2	0.308	0.132	0.132	30	1.6	11
S3	0.308	0.132	0.263	28	1.7	14
S4	0.308	0.132	0.5	30	1.6	15

In order to get insight into the effect of $BaTiO_3$ loading on the dielectric films, the surface morphology of screen-printed dielectric film was measured by the tapping mode AFM. Fig. 5-6 depicts AFM topographical and phase images of P(VDF-TrFE)/PMMA/Silica and P(VDF-TrFE)/PMMA/$BaTiO_3$/Silica with $BaTiO_3$ loadings of 22 wt%, 36 wt%, and 52 wt%. It was observed that the dielectric S1 exhibited rigid rod-like crystal structure of the blend polymer matrix without loading $BaTiO_3$ into the polymer matrix. With the incorporation of $BaTiO_3$, the color of the dielectric films changed from transparent to white with the addition of the $BaTiO_3$ nanoparticles in the dielectric ink. It was observed that the modified nanoparitcles were well dispersed in the crystal grains on the surface of the dielectric films of S2 and S3, having an average particle size of 125 nm, which was indicative of good miscibility of GPTMS-modified $BaTiO_3$ with the polymer matrix. For S4 with high loading of 52 wt% $BaTiO_3$, the nanocomposite film still presented good miscibility with no sign of phase separation between nanoparticles and polymer binder. In addition, the surface roughness of the dielectric films increased from 51 nm (0 wt%) to 81 nm (52 wt%), but there was no direct relationship between the surface roughness and the mobility.

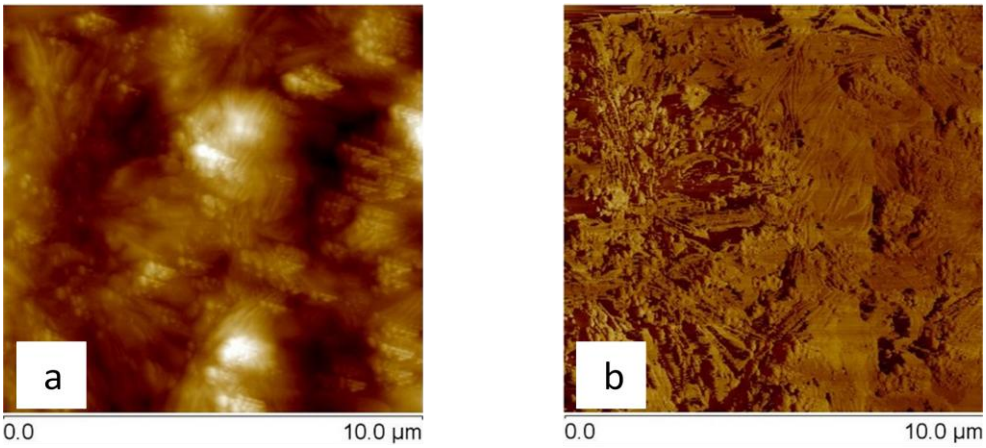

(i)

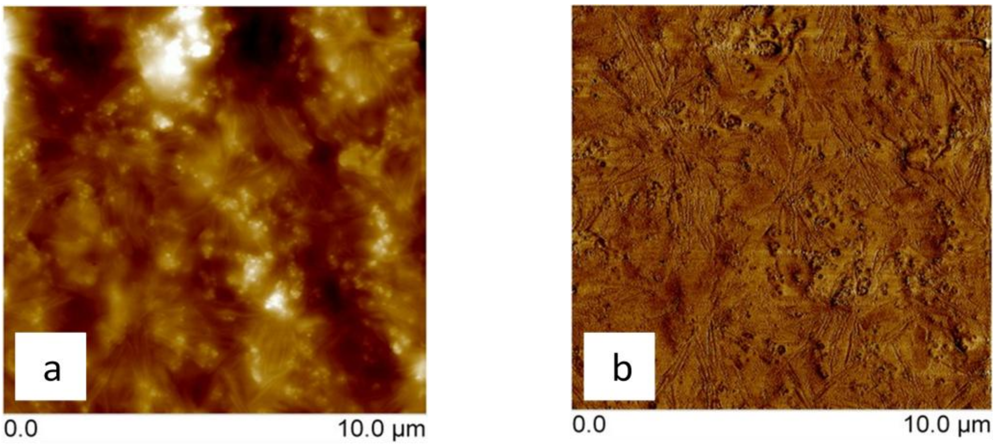

(ii)

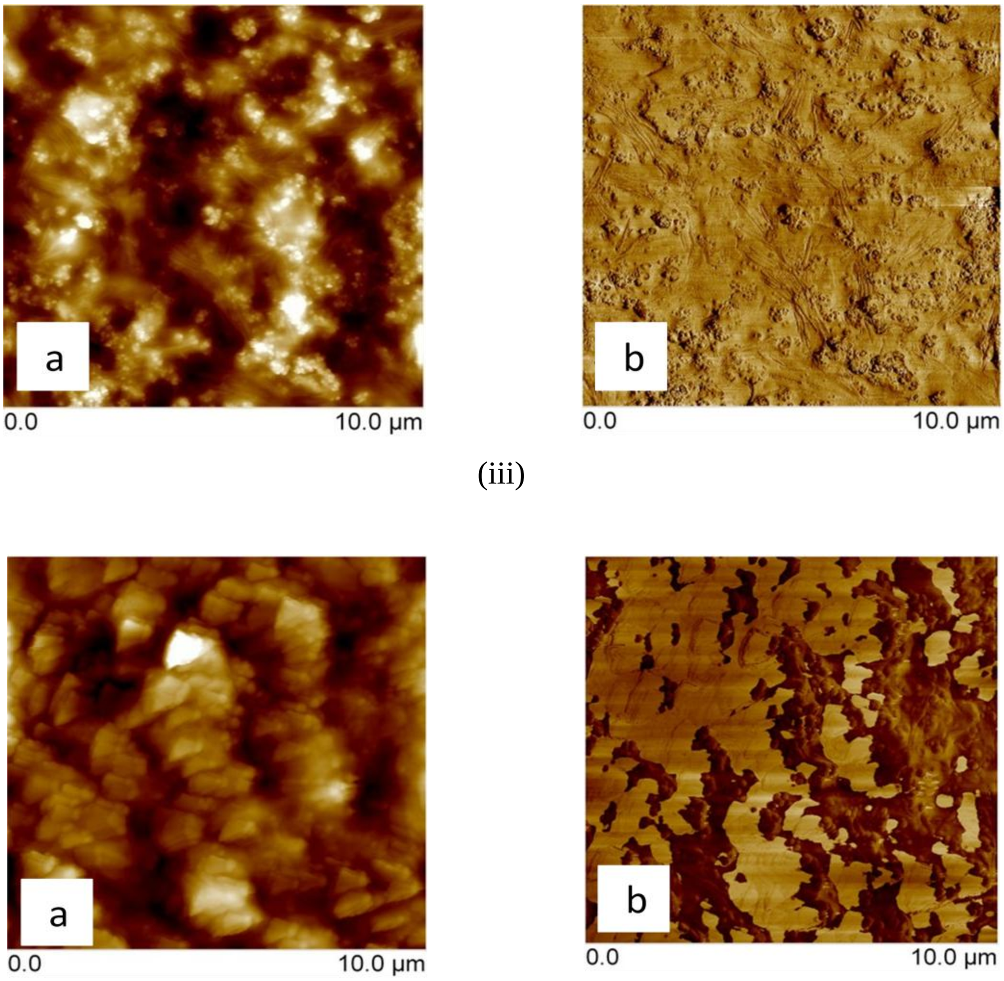

(iii)

(iv)

Fig. 5-6 AFM topographical (a) and phase (b) images of the dielectrics of (i) S1, (ii) S2, (iii) S3, and (iv) S4

Cross section specimens for SEM measurement were prepared to investigate the morphology of bulk dielectric films deposited by screen printing. Fig. 5-7 depicts the cross section SEM micrograph of P(VDF-TrFE)/PMMA/Silica and P(VDF-TrFE)/PMMA/$BaTiO_3$/Silica with $BaTiO_3$ loadings of 22 wt%, 36 wt%, and 52 wt%, respectively. The morphology of the bulk dielectric was consistent through the dielectric thickness, which was in agreement with the surface morphology measured by AFM. With blending amorphous PMMA, the dielectric S1 featured typical rigid rod-like crystal structure with an average diameter of 280 nm. With the increase in $BaTiO_3$, the rigid rod-like crystal structure of polymer matrix disappeared in the bulk dielectric film which is typical of the nanocomposite films.

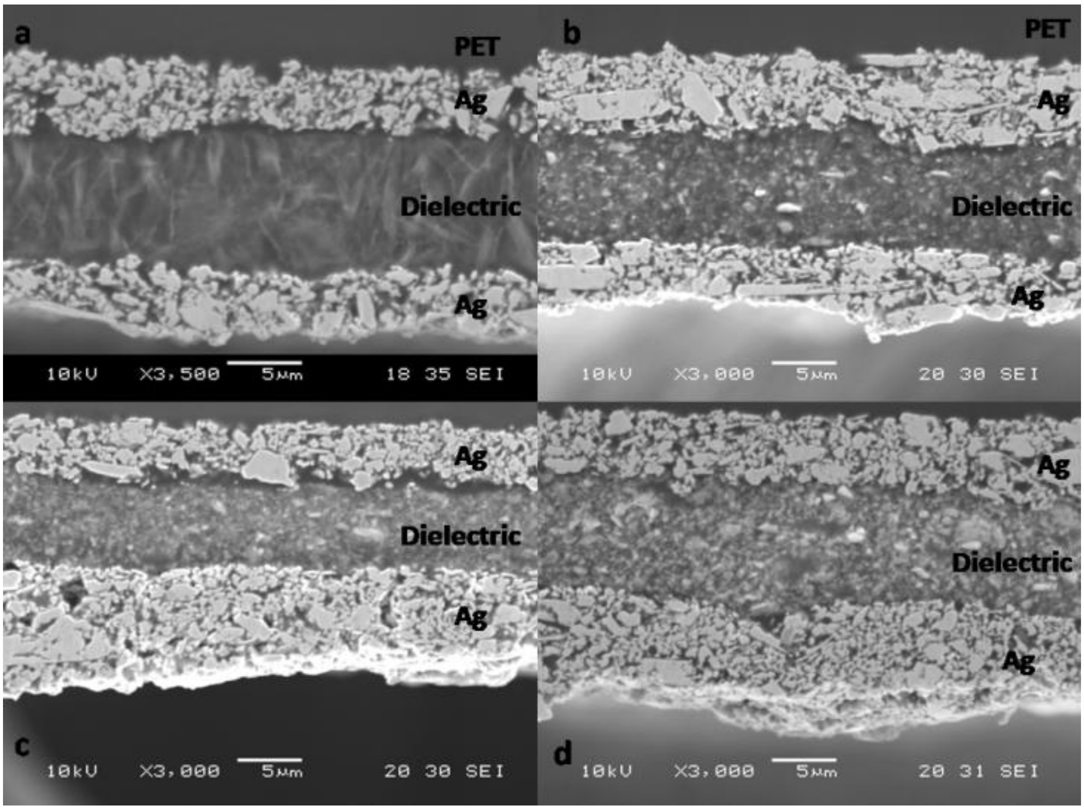

Fig. 5-7 Cross section SEM micrographs (a) dielectric S1, (b) S2, (c) S3, and (d) S4

As discussed in Section 4.4, the transistors were fabricated on the thin, smooth Al foil as the common gate, so thin dielectric film layer (3 μm) could be sufficient for the insulating function between Al electrode and the source/drain electrodes. As for fully-additive printed devices on the PET substrate, the thickness of dielectric film should be increased to maintain the insulating properties between the gate electrode layer (5 μm) and source/drain electrode layer (6 μm). Compared to dielectric films with a thickness of 3.5 μm on the Al foil, the thicknesses of screen-printed dielectric film deposited from the inks of S1, S2, S3, and S4 were 9 μm, 9 μm, 7 μm, and 9 μm, respectively. The electrical characteristics of TIPs-pentacene OFETs using P(VDF-TrFE)/PMMA/BaTiO$_3$/Silica as the gate dielectric were measured using Keithley 4200-SCS under ambient atmosphere.

The comparison of the gate leakage current of OFETs using S1 and S2 as gate dielectrics was depicted in Fig. 5-8. The OFETs using the dielectric S1 without BaTiO$_3$ exhibited an order of magnitude higher leakage current (10^{-8} A at -60 V gate bias), comparing to the leakage current (10^{-9} A) obtained from OFETs using the dielectric S2 at similar operating conditions. The low leakage current obtained from OFETs using dielectric S2 was attributed to the good miscibility between modified BaTiO$_3$ and polymer binder.

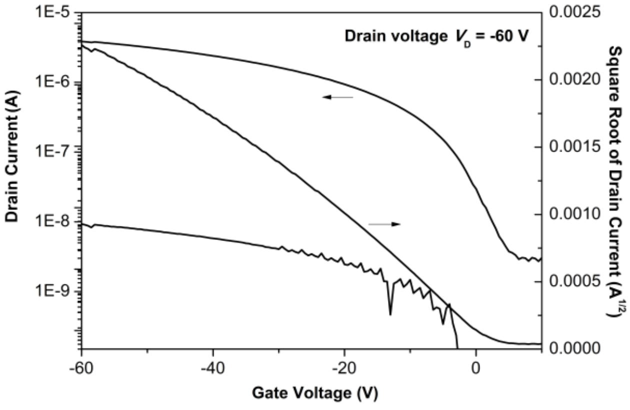

(a)

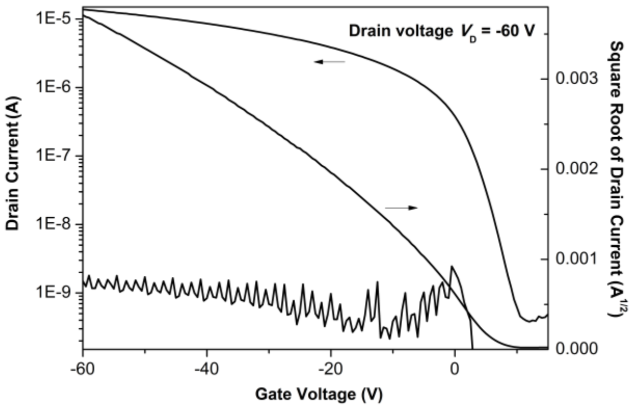

(b)

Fig. 5-8 The comparison of leakage current of OFETs using S1 (a) and S2 (b) as gate dielectrics

It was observed that TIPs-pentacene OFETs with S2 and S3 as the gate dielectrics had a small hysteresis under multiple bias sweeping. First of all, the hydrophobic surface of the fluoropolymer contained a low density of electron traps such as hydroxyl groups, so little charge trapping was observed at the interface of the dielectric/semiconductor as well as in the bulk dielectric. Secondly, GPTMS-modified $BaTiO_3$ nanoparticles had small particle size, so the degree of ferroelectricity was likely to be too small to carry out the strong *I*-*V* hysteresis. Therefore, the good electrical properties make sure that P(VDF-TrFE)-based polymer nanocomposite dielectrics are suitable for ink formulation in PE.

Fig. 5-9, 5-10, 5-11, and 5-12 depict the transfer characteristics of TIPs-pentacene OFETs using S1, S2, S3, and S4 as the gate dielectrics at V_D of -20 V, -40 V, and -60 V and the output characteristics, respectively. TIPs-pentacene using the dielectrics S1, S2, and S3 featured a comparable mobility and an I_{on}/I_{off} of 10^4 at a high V_D of -60 V.

All the transistors could be switched on at a low V_D of -20 V, but having a low I_{on}/I_{off} of 10^3. TIPs-pentacene OFETs using the dielectric S4 could be switched on at a V_D of -20 V, having a mobility of 0.2 cm^2/Vs with an I_{on}/I_{off} of 10^4, comparable to that at V_D of -40 V and -60 V. Thence, high-*k* polymer nanocomposite with sufficient $BaTiO_3$ loading could achieve low-operating-voltage fully-additive printed OFETs. It is unlikely to further increase the $BaTiO_3$ loading, because higher amount of nanoparticles might destroy the flexibility of the polymer matrix, thereby resulting in more defects in the dielectric films. In order to further improve the capacitance, the size of the nanoparticle should be reduced via direct synthetic methods instead of the commercially available powders with one specific nanoparticle size.

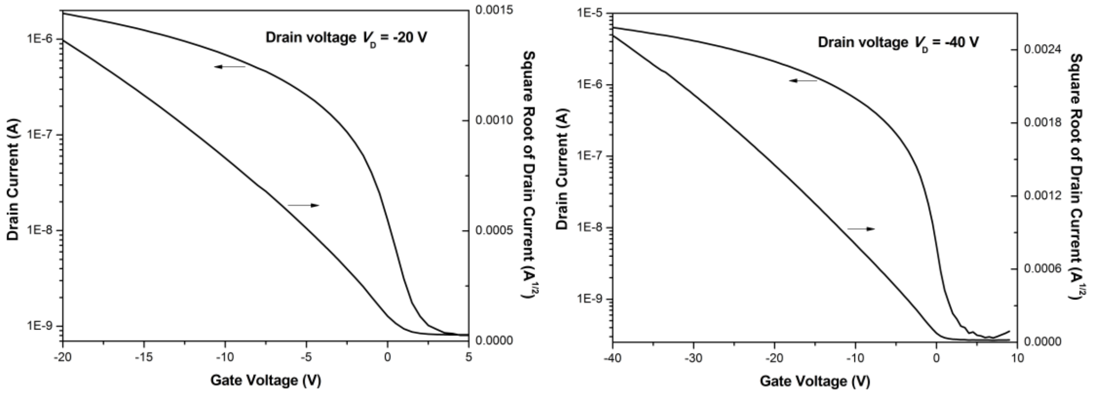

(a) (b)

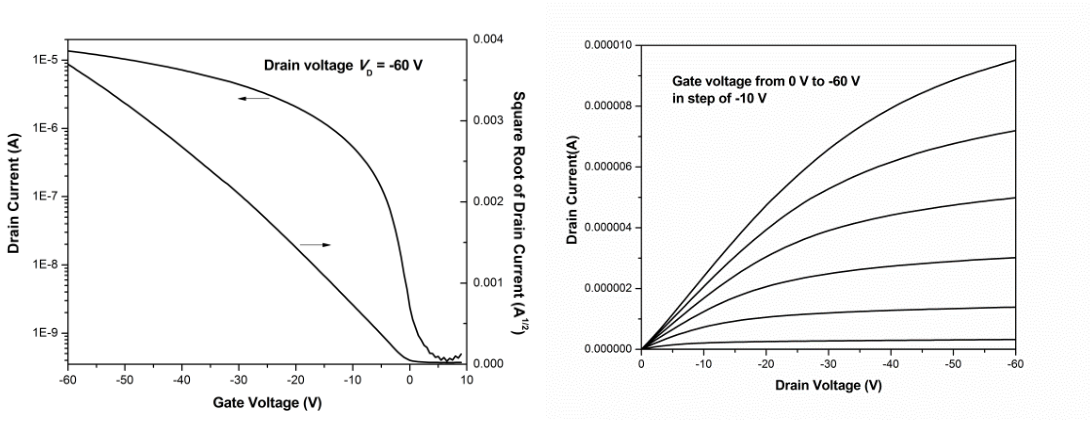

(c) (d)

Fig. 5-9 The transfer characteristics of TIPs-pentacene OFETs using the dielectric S1 at V_D of -20 V (a), -40 V (b), and -60 V (c); The output characteristics (d) of TIPs-pentacene OFETs using the dielectric S1

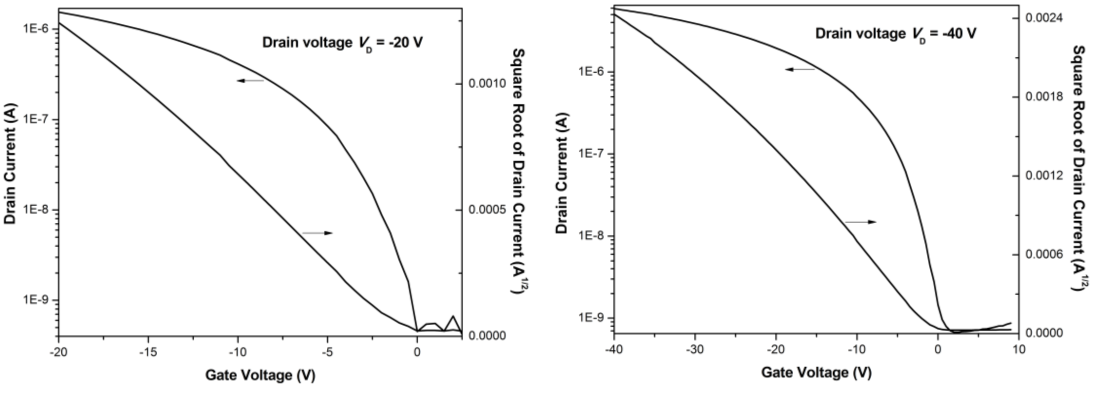

(a) (b)

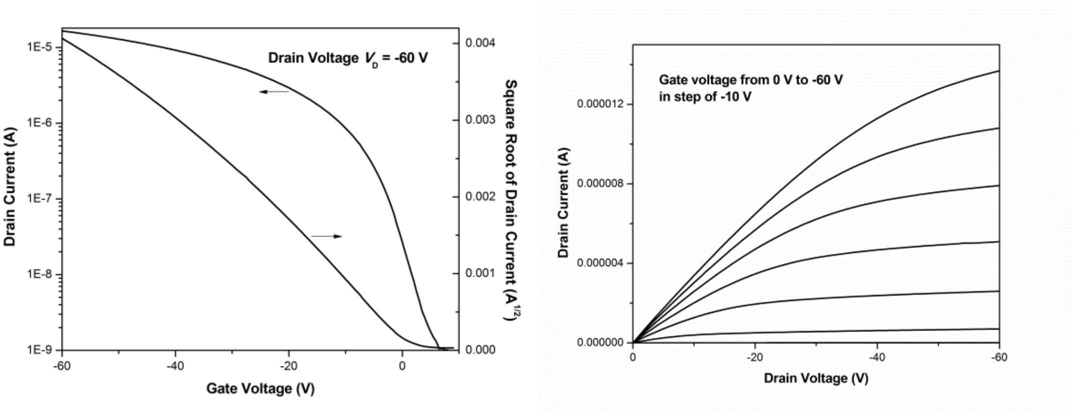

(c) (d)

Fig. 5-10 The transfer characteristics of TIPs-pentacene OFETs using the dielectric S2 at V_D of -20 V (a), -40 V (b), and -60 V (c); The output characteristics (d) of TIPs-pentacene OFETs using the dielectric S2

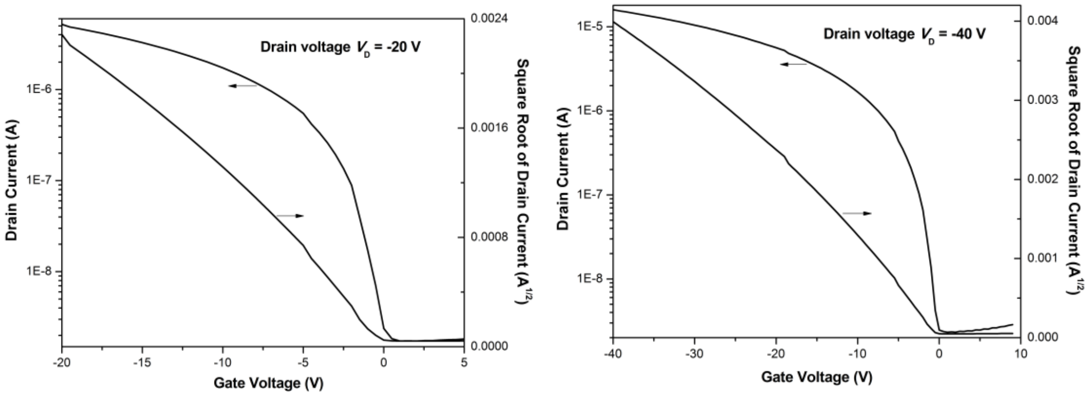

(a) (b)

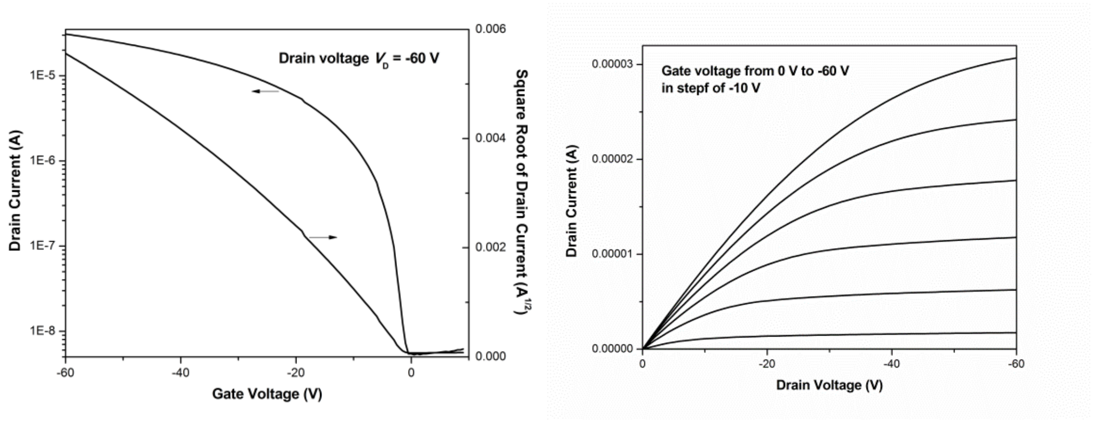

(c) (d)

Fig. 5-11 The transfer characteristics of TIPs-pentacene OFETs using the dielectric S3 at V_D of -20 V (a), -40 V (b), and -60 V (c); The output characteristics (d) of TIPs-pentacene OFETs using the dielectric S3

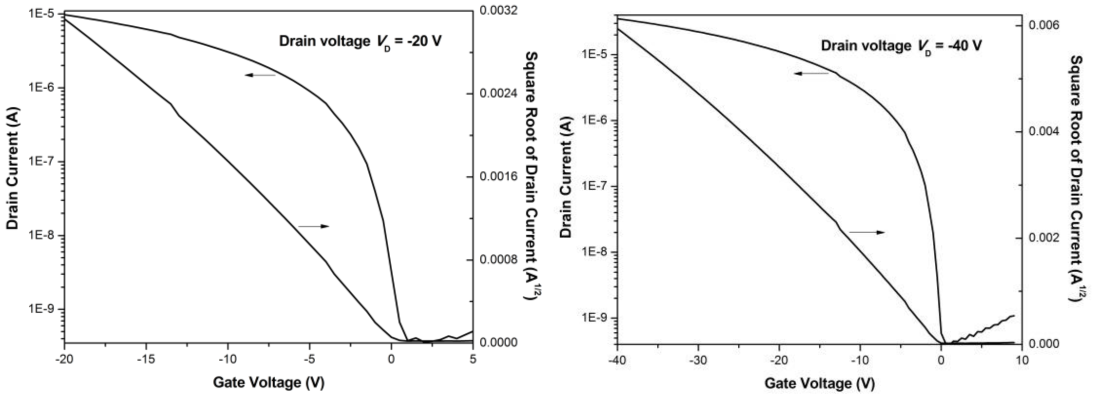

(a) (b)

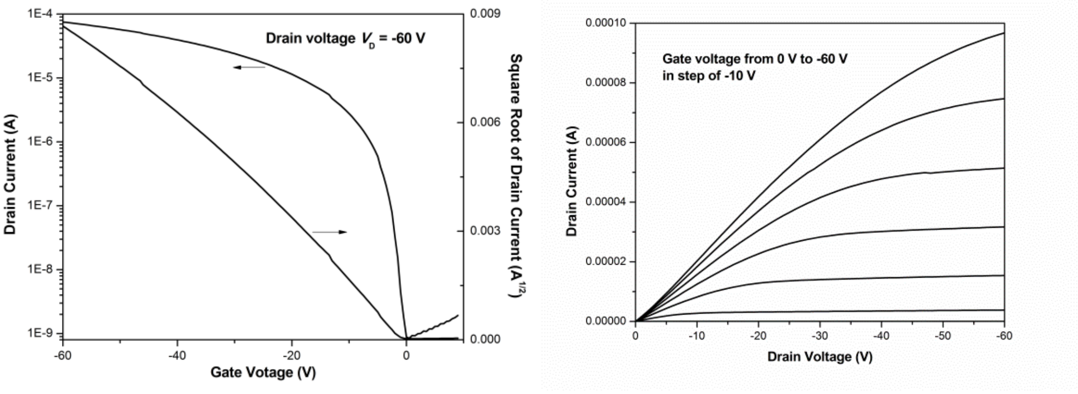

(c) (d)

Fig. 5-12 The transfer characteristics of TIPs-pentacene OFETs using the dielectric S4 at V_D of -20 V (a), -40 V (b), and -60 V (c); The output characteristics (d) of TIPs-pentacene OFETs using the dielectric S4

Table 5-4 tabulates the properties of polymer nanocomposite dielectric inks with different $BaTiO_3$ loadings for TIPs-pentacene OFETs. With an increase of $BaTiO_3$ loading from 0 wt% to 52 wt%, the dielectric constant was enhanced from 6.4 to 10, when the capacitance increased from 0.63 nF/cm^2 to 0.99 nF/cm^2. The OFETs mobility was dependent on the dielectric constant. When the dielectric constant was increased by 56% from 6.4 to 10, the average OFETs mobility was improved by a factor of 4 from 0.04 cm^2/Vs to 0.16 cm^2/Vs. The capacitance of the dielectric was obtained from the capacitance-voltage curve with a capacitor area of 1×1 cm^2, which was measured at a low frequency of 1 kHz. In addition, with an increase in $BaTiO_3$ loading, the surface roughness of the dielectric films was increased, with dielectric S1 of 51 nm, S2 of 64 nm, S3 of 69 nm and S4 of 81 nm, respectively.

Table 5-4 Properties of polymer nanocomposite dielectrics and TIPs-pentacene OFETs

Ink	***C* (nF/cm^2)**	***k***	**R_q (nm)**	**V_T (V)**	**I_{on}/I_{off}**	**μ (cm^2/Vs)**
S1	0.63	6.4	51	0.2	10^4	0.04
S2	0.68	6.9	64	1.8	10^4	0.04
S3	1.0	7.9	69	-0.6	10^4	0.05
S4	0.99	10	81	-0.3	10^4	0.16

5.5 Conclusions

An ink formulation based on high-*k* P(VDF-TrFE) as a polymer matrix has been presented with the objective of low-voltage OFET operation. Low-*k* PMMA has been blended to tune the bulk crystallinity and surface morphology of the dielectric films, thereby reducing the amount of the ferroelectric crystalline to avoid hysteresis. Modified $BaTiO_3$ has been loaded into the polymer matrix to achieve high capacitance, low gate leakage current, and small hysteresis of OFETs. In addition, the fumed silica as the viscosity modifier has endowed its good printability and compatibility of the dielectric ink with the PET substrate. Fully-additive printed TIPs-pentacene OFETs have been successfully fabricated on the PET substrate using the optimized dielectrics.

With GPTMS-modified $BaTiO_3$ loading of 52%, the transistor can be operated at a relatively low drain voltage of -20 V, having a mobility of 0.2 cm^2/Vs and an I_{on}/I_{off} of 10^4. This dielectric ink was shown to be promising for the realization of fully-additive printed analog and digital printed circuits.

Chapter 6 Conclusions and Future work

6.1 Conclusions

The grand vision of this PhD program is to realize/fabricate sophisticated printed circuits and systems and OPVs using a fully-additive printing process appropriate for flexible substrates, particularly the fully-additive screen printing process. To this end, the specific objectives herein pertain to the first two chains of the PE supply chain, specifically the design and synthesis of organic semiconductors, formulation of printable dielectrics and printing thereof.

In Chapter 1, the motivation of this PhD program encompassing the aforesaid grand vision and specific objectives was unambiguously articulated. As a preamble to the research work presented in Chapters 3, 4 and 5, Chapter 2 presented a broad literature overview and review of PE, including a critical review of reported work pertaining to the specific objectives herein.

In Chapter 3, synthesis and characterization of a *p*-type organic semiconductor has been accomplished. Specifically, a novel regioregular, selenophene and thiophene-based PBTBS was synthesized, and OPVs based on PBTBS as the electron donor material blended with PCBM were fabricated and characterized. Compared to PQT-12, the EQE of solar cells exhibited much better performance with ~3.37% at 550 nm. The PBTBS-based OFETs featured *p*-channel characteristics and exhibited a hole mobility of 1×10^{-3} cm^2/Vs.

A novel solution-processable *n*-type organic semiconductor T3PT3 based on PDI and hexylthiophenes was also successfully synthesized. Its photovoltaic properties applied as the electron acceptor material in BHJ OPVs were investigated.

The work in Chapter 3 has been published [35] in the Solar Energy Materials & Solar Cells journal.

In Chapter 4, a polymer nanocomposite dielectric for realizing OFETs on an Al foil has been formulated. Specifically, P(VDF-TrFE) blending PMMA was chosen as the polymer matrix for polymer nanocomposite dielectric with an optimum blending concentration of 30 wt%. High-*k* $BaTiO_3$ was incorporated into the blend polymer matrix of P(VDF-TrFE)/PMMA to improve the electrical properties. To achieve fully-additive printed OFETs fabrication, two screen-printable dielectric materials P(VDF-TrFE)/PMMA/Silica (PPS) and P(VDF-TrFE)/PMMA/$BaTiO_3$/Silica (PPBS) were formulated.

Compared to OFETs using spin-coated dielectrics, the screen-printed transistors herein using PPBS as the gate dielectric exhibited a comparable mobility of 0.01 cm^2/Vs, but featured a substantially smaller positive V_T of 2 V. The smaller voltage was attributed to higher capacitance resulting from much thinner dielectric films. The device performance can be improved by optimization of the ink formulation and device fabrication.

The work in Chapter 4 has been published [36] in the Organic Electronics journal.

In Chapter 5, printable dielectrics for fully-additive PE based on screen printing on flexible plastic foils have been formulated. Specifically, a novel screen-printable polymer nanocomposite dielectric ink was successfully formulated. With GPTMS-modified $BaTiO_3$ loading of 52%, the ensuing printed transistor can be operated at a low drain voltage of -20 V, having a mobility of 0.2 cm^2/Vs and an I_{on}/I_{off} of 10^4. This dielectric ink is promising for the realization of fully-additive printed analog and digital printed circuits.

The work in Chapter 5 has been published [37] in the Royal Society of Chemistry (RSC) Advances journal.

In conclusion, this thesis has delineated research contributions to the first two chains of the PE supply chain, specifically towards the design and synthesis of organic semiconductors, formulation of printable dielectrics, and printing thereof for fully-additive PE for realizing circuits and systems.

6.2 Future work

Not unexpectedly, the progress of PE technology will continue to evolve with the first two chains of PE being major components of the PE supply chain. The research contributions in this PhD program have augmented towards said evolution, and further interesting future research includes the following pertaining to Materials and Printing.

6.2.1 Materials engineering

Our future work pertaining to materials includes the design and synthesis of new *p*- and *n*-type organic semiconductors as well as polymer dielectrics for PE. In general, for sake of practical PE, the requirements of stability, solubility and purity should be considered for device performance and lifetime with organic semiconductors as active materials.

As discussed in Chapter 3, the synthesis of the *n*-type organic semiconductor T3PT3 is largely inapplicable to the industry. Specifically, the solubility and film-forming properties of this compound were insufficient, including intolerable short circuits in solar cell device measurements. It is hence suggested here that the polymer based on alkylthiophenes and PDI needs to be synthesized to improve its solution-based processability.

The donor-acceptor motif could be used to achieve good *n*- and *p*-type organic semiconductors as active semiconductors in OPVs or OFETs. Bandgap engineering is necessary to improve the electrical stability of the organic semiconductors, and largely influences the charge injection from the metal electrode. It is suggested here that low bandgap polymers based on donor and acceptor moieties be considered as promising organic semiconductors to achieve the ambipolar CMOS inverters. In short, it is suggested herein that unipolar *n*- and *p*-type organic semiconductors with comparable mobility as well as ambipolar organic semiconductors be researched.

For the polymer nanocomposite dielectric, as the polymer matrix greatly influences the dielectric properties, it would be interesting to explore other high-*k* polymer dielectric materials as the polymer matrix in the ink formulation. Further research would include the synthesis of inorganic nanoparticles with different sizes in situ polymerization for polymer nanocomposite dielectric ink formulation. It is prudent to note that although the flexibility of the polymer matrix might be limited by the loading of nanoparticles, it would be interesting to explore multilayer dielectric materials could be explored for low-voltage operation. One possibility is the composition of cross-linked polymer dielectric as the top layer and the high-*k* inorganic dielectric as the bottom layer.

6.2.2 Fully-additive printed electronics

It has already been discussed herein that high-*k*, thin, screen-printable polymer nanocomposite dielectric is promising for PE. On this basis, it would be interesting to explore P(VDF-TrFE)/PMMA/$BaTiO_3$/Silica as the gate dielectric for fabricating *p*-type TIPs-pentacene OFETs to realize fully-additive printed analog and digital printed circuits.

References

1. Rogers, J.A., *Electronics: A diverse printed future.* Nature, 2010. **468:** p.177-178.
2. Wong, W.S., et al., *Flexible electronics: Materials and applications*. A. Salleo, Editor. 2009, Springer.
3. Venugopal, S.M., et al., *Flexible electronics: What can it do? What should it do?* IEEE International Reliability Physics Symposium Proceedings, 2010. p. 644-649.
4. Arias, A.C., et al., *All printed thin film transistors for flexible electronics*. Proceedings of SPIE - The International Society for Optical Engineering, 2008. **7054**: 70540L.
5. Barret, M., et al., *Inkjet-printed low-voltage organic thin-film transistors: Towards low-cost flexible*. Materials Research Society Symposium Proceedings, 2007. **1003:** p. 147-152.
6. Barret, M., et al., *Inkjet-printed polymer thin-film transistors: Enhancing performances by contact resistances engineering.* Organic Electronics: physics, materials, applications, 2008. **9**(6): p. 1093-1100.
7. Blanchet, G., et al., *Printing techniques for plastic electronics.* Journal of Imaging Science and Technology, 2003. **47**(4): p. 296-303.
8. De Gans, B.J., et al., *Inkjet printing of polymers: State of the art and future developments.* Advanced Materials, 2004. **16**(3): p. 203-213.
9. Jang, J., et al., *Organic thin-film transistor and its application to large area electronics*. IDMC 2007 - International Display Manufacturing Conference and FPD Expo - Proceedings, 2007. p. 427-430.
10. Karwa, A., et al., *Printable electronics: Patterning of conductive materials for novel applications*. Materials Research Society Symposium Proceedings, 2005. **828:** p. 293-297.
11. Leenen, M.A.M., et al., *Printable electronics: Flexibility for the future.* Physica Status Solidi (A) Applications and Materials, 2009. **206**(4): p. 588-597.
12. Ling, M.M., et al., *Thin film deposition, patterning, and printing in organic thin film transistors.* Chemistry of Materials, 2004. **16**(23): p. 4824-4840.
13. Milmo, S., *Printed electronics make gains, but there are challenges ahead.* Ink World, 2008. **14**(8): p. 12-13.
14. Savastano, D., *RFID and printed electronics.* Ink World, 2007. **13**(5): p. 32-34.
15. Chang, J., et al., *Fully printed electronics on flexible substrates: High gain amplifiers and DAC.* Organic Electronics: physics, materials, applications, 2014. **15**(3): p. 701-710.
16. Cantatore, E., *Applications of organic and printed electronics.* 2013, Springer.
17. Organic Electronics Association (OEA), *Organic and Printed Electronics 5th edition.* 2013.
18. Takeda, Y., et al., *Integrated circuits using fully solution-processed organic TFT devices with printed silver electrodes.* Organic Electronics, 2013. **14**(12): p. 3362-3370.
19. Baeg, K.J., et al., *Low-voltage, high speed inkjet-printed flexible complementary polymer electronic circuits.* Organic Electronics: physics, materials, applications, 2013. **14**(5): p. 1407-1418.
20. Guerin, M., et al., *High-gain fully printed organic complementary circuits on flexible plastic foils.* IEEE Transactions on Electron Devices, 2011. **58**(10): p. 3587-3593.
21. Young, R.T., et al., *Laser processing of semiconductor materials*. Annual Review of Materials Science. 1982. **12:** p. 323-350.
22. Singh, R., et al., *A laser-trimmed rail-to-rail precision CMOS operational amplifier.* IEEE Transactions on Circuits and Systems II: Express Briefs, 2011. **58**(2): p. 75-79.
23. Wang, J.A., et al. *The high-speed ADC based on the adjustable digital trimming technique. 2008 International Conference on Communications, Circuits and Systems Proceedings, ICCCAS 2008*. 2008. p. 1358-1360.

24. Xiong, W., et al., *A 3-V, 6-bit C-2C digital-to-analog converter using complementary organic thin-film transistors on glass.* IEEE Journal of Solid-State Circuits, 2010. **45**(7): p. 1380-1388.
25. Jung, M., et al., *All-Printed and roll-to-roll-printable 13.56-MHz-operated 1-bit RF tag on plastic foils.* IEEE Transactions on Electron Devices, 2010. **57**(3): p. 571-580.
26. Zhao, J., et al., *Fabrication and electrical properties of all-printed carbon nanotube thin film transistors on flexible substrates.* Journal of Materials Chemistry, 2012. **22**(38): p. 20747-20753.
27. Lau, P.H., et al., *Fully printed, high performance carbon nanotube thin-film transistors on flexible substrates.* Nano Letters, 2013. **13**(8): p. 3864-3869.
28. Cho, S.Y., et al., *Inkjet-printed organic thin film transistors based on TIPS pentacene with insulating polymers.* Journal of Materials Chemistry C, 2013. **1**(5): p. 914-923.
29. Park, S.K., et al., *High mobility solution processed 6,13-bis(triisopropyl-silylethynyl) pentacene organic thin film transistors.* Applied Physics Letters, 2007. **91**(6): 063514.
30. Snow, E.S., et al., *Random networks of carbon nanotubes as an electronic material.* Applied Physics Letters, 2003. **82**(13): p. 2145-2147.
31. Friend, R.H., et al., *Electroluminescence in conjugated polymers.* Nature, 1999. **397**(6715): p. 121-128.
32. Halls, J.J.M., et al., *Efficient photodiodes from interpenetrating polymer networks.* Nature, 1995. **376**(6540): p. 498-500.
33. Yu, G., et al., *Polymer photovoltaic cells: Enhanced efficiencies via a network of internal donor-acceptor heterojunctions.* Science, 1995. **270**(5243): p. 1789-1791.
34. Gelinck, G.H., et al., *Flexible active-matrix displays and shift registers based on solution-processed organic transistors.* Nature Materials, 2004. **3**(2): p. 106-110.
35. Qiao, F., et al., *Photovoltaic characterization of poly(2,5-bis(3-dodecylthiophen-2-yl)-2',2''-biselenophene) for organic solar cells.* Solar Energy Materials and Solar Cells, 2010. **94**(3): p. 442-445.
36. Hou, X., et al., *Polymer nanocomposite dielectric based on P(VDF-TrFE)/PMMA/BaTiO$_3$ for TIPs-pentacene OFETs.* Organic Electronics, 2015. **17**(0): p. 247-252.
37. Hou, X., et al., *Formulation of novel screen-printable dielectric ink for fully-printed TIPs-pentacene OFETs.* RSC Advances, 2014. **4**(71): p. 37687-37690.
38. Pernstich, K.P., et al., *Threshold voltage shift in organic field effect transistors by dipole monolayers on the gate insulator.* Journal of Applied Physics, 2004. **96**(11): p. 6431-6438.
39. Kano, M., et al., *Control of device parameters by active layer thickness in organic field-effect transistors.* Applied Physics Letters, 2011. **98**(7): 073307.
40. Dimitrakopoulos, C.D., et al., *Conduction mechanisms and a potential fundamental limit to charge-carrier mobility in organic semiconductors.* IBM Journal of Research and Development, 2001. **31**(1): p. 11-27.
41. Dimitrakopoulos, C.D., et al., *Organic Thin Film Transistors for Large Area Electronics.* Advanced Materials, 2002. **14**(2): p. 99-117.
42. Karl, N., *Charge carrier transport in organic semiconductors.* Synthetic Metals, 2003. **133-134**: p. 649-657.
43. Kohler, A., *Organic semiconductors: No more breaks for electrons.* Nature Materials, 2012. **11**(10): p. 836-837.
44. Chua, L.-L., et al., *General observation of n-type field-effect behaviour in organic semiconductors.* Nature, 2005. **434**(7030): p. 194-199.
45. Umeyama, T., et al., *Design and control of organic semiconductors and their nanostructures for polymer-fullerene-based photovoltaic devices.* Journal of Materials Chemistry A, 2014. **2**(30): p. 11545-11560.
46. Duan, C., et al., *Recent development of push-pull conjugated polymers for bulk-heterojunction photovoltaics: rational design and fine tailoring of molecular structures.* Journal of Materials Chemistry, 2012. **22**(21): p. 10416-10434.

47. Meijer, E.J., et al., *Solution-processed ambipolar organic field-effect transistors and inverters.* Nature Materials, 2003. **2**(10): p. 678-682.
48. Park, B., et al., *Enhanced hole mobility in ambipolar rubrene thin film transistors on polystyrene.* Applied Physics Letters, 2008. **92**(13): 133302.
49. Li, Z., et al., *Induced crystallization of rubrene in thin-film transistors.* Advanced Materials. **22**(30): p. 3242-3246.
50. Park, S.K., et al., *Environmental and operational stability of solution-processed 6,13-bis(triisopropyl-silylethynyl) pentacene thin film transistors.* Organic Electronics: physics, materials, applications, 2009. **10**(3): p. 486-490.
51. Lucas, B., et al., *Organic transistors and phototransistors based on small molecules.* Polymer International, 2012. **61**(3): p. 374-389.
52. Iino, H., et al., *Availability of liquid crystalline molecules for polycrystalline organic semiconductor thin films.* Japanese Journal of Applied Physics, Part 2: Letters, 2006. **45**(33-36): p. L867-L870.
53. Gao, P., et al., *Dithieno[2,3-d;2'3'-d']benzo[1,2-b;4,5-b'] dithiophene (DTBDT) as semiconductor for high-performance, solution-processed organic field-effect transistors.* Advanced Materials, 2009. **21**(2): p. 213-216.
54. Sirringhaus, H., et al., *Integrated optoelectronic devices based on conjugated polymers.* Science, 1998. **280**(5370): p. 1741-1744.
55. Bao, Z., et al., *Soluble and processable regioregular poly(3-hexylthiophene) for thin film field-effect transistor applications with high mobility.* Applied Physics Letters, 1996. **69**(26): p. 4108-4110.
56. Ong, B.S., et al., *High-Performance Semiconducting Polythiophenes for Organic Thin-Film Transistors.* Journal of the American Chemical Society, 2004. **126**(11): p. 3378-3379.
57. McCulloch, I., et al., *Influence of molecular design on the field-effect transistor characteristics of terthiophene polymers.* Chemistry of Materials, 2005. **17**(6): p. 1381-1385.
58. Sirringhaus, H., et al., *Mobility enhancement in conjugated polymer field-effect transistors through chain alignment in a liquid-crystalline phase.* Applied Physics Letters, 2000. **77**(3): p. 406-408.
59. McCulloch, I., et al., *Liquid-crystalline semiconducting polymers with high charge-carrier mobility.* Nature Materials, 2006. **5**(4): p. 328-333.
60. DeLongchamp, D.M., et al., *High carrier mobility polythiophene thin films: Structure determination by experiment and theory.* Advanced Materials, 2007. **19**(6): p. 833-837.
61. Jung, Y., et al., *The effect of interfacial roughness on the thin film morphology and charge transport of high-performance polythiophenes.* Advanced Functional Materials, 2008. **18**(5): p. 742-750.
62. Lim, B., et al., *A new poly(thienylenevinylene) derivative with high mobility and oxidative stability for organic thin-film transistors and solar cells.* Advanced Materials, 2009. **21**(27): p. 2808-2814.
63. Parmer, J.E., et al., *Organic bulk heterojunction solar cells using poly(2,5-bis(3-tetradecyllthiophen-2-yl)thieno[3,2,-b] thiophene).* Applied Physics Letters, 2008. **92**(11): 113309.
64. Wang, C., et al., *Microstructural origin of high mobility in high-performance poly(thieno-thiophene) thin-film transistors.* Advanced Materials. **22**(6): p. 697-701.
65. Shi, J., et al., *All-Printed Carbon Nanotube finFETs on Plastic Substrates for High-Performance Flexible Electronics.* Advanced Materials, 2012. **24**(3): p. 358-361.
66. Li, Y., et al., *A High Mobility P-Type DPP-Thieno[3,2-b]thiophene Copolymer for Organic Thin-Film Transistors.* Advanced Materials, 2010. **22**(43): p. 4862-4866.
67. Newman, C.R., et al., *Introduction to Organic Thin Film Transistors and Design of n-Channel Organic Semiconductors.* Chemistry of Materials, 2004. **16**(23): p. 4436-4451.

68. Huo, L., et al., *Synthesis and absorption spectra of n-type conjugated polymers based on perylene diimide.* Macromolecular Rapid Communications, 2008. **29**(17): p. 1444-1448.
69. Yuan, M.C., et al., *Synthesis and characterization of donor-bridge-acceptor alternating copolymers containing perylene diimide units and their application to photovoltaic cells.* Journal of Polymer Science, Part A: Polymer Chemistry. **48**(6): p. 1298-1309.
70. Singh, T.B., et al., *Soluble derivatives of perylene and naphthalene diimide for n-channel organic field-effect transistors.* Organic Electronics: physics, materials, applications, 2006. **7**(6): p. 480-489.
71. Yuney, K., et al., *Synthesis, photochemical, and electrochemical properties of naphthalene-1,4,5,8-tetracarboxylic acid-bis-(N,N'-bis-(2,2,4(2,4,4)-trimethylhexylpolyimide)) and poly(N,N'-bis-(2,2,4(2,4,4)-trimethyl-6-aminohexyl) 3,4,9,10-perylenetetracarboxdiimide).* European Polymer Journal, 2007. **43**(6): p. 2308-2320.
72. Melzer, C., et al., *Organic Field-Effect Transistors for CMOS Devices*, in *Organic Electronics*, T. Grasser, G. Meller, and L. Li, Editors. 2010, Springer Berlin Heidelberg. p. 189-212.
73. Yan, H., et al., *A high-mobility electron-transporting polymer for printed transistors.* Nature, 2009. **457**(7230): p. 679-686.
74. Dodabalapur, A., et al., *Organic heterostructure field-effect transistors.* Science, 1995. **269**(5230): p. 1560-1562.
75. Katz, H.E., et al., *A soluble and air-stable organic semiconductor with high electron mobility.* Nature, 2000. **404**(6777): p. 478-481.
76. Babel, A., et al., *High Electron Mobility in Ladder Polymer Field-Effect Transistors.* Journal of the American Chemical Society, 2003. **125**(45): p. 13656-13657.
77. Yan, H., et al., *Solution processed top-gate n-channel transistors and complementary circuits on plastics operating in ambient conditions.* Advanced Materials, 2008. **20**(18): p. 3393-3398.
78. Ito, Y., et al., *Crystalline ultrasmooth self-assembled monolayers of alkylsilanes for organic field-effect transistors.* Journal of the American Chemical Society, 2009. **131**(26): p. 9396-9404.
79. Chang, J.F., et al., *Patterning of solution-processed semiconducting polymers in high-mobility thin-film transistors by physical delamination.* Advanced Materials, 2009. **21**(24): p. 2530-2535.
80. Piliego, C., et al., *High Electron Mobility and Ambient Stability in Solution-Processed Perylene-Based Organic Field-Effect Transistors.* Advanced Materials, 2009. **21**(16): p. 1573-1576.
81. Yamamoto, K., et al., *Evaluation of molecular orientation and alignment of poly(3-hexylthiophene) on Au (111) and on poly(4-vinylphenol) surfaces.* Thin Solid Films, 2008. **516**(9): p. 2695-2699.
82. Gil, E., et al., *Characteristics of* SiO_x *thin films deposited by atmospheric pressure chemical vapor deposition as a function of* $HMDS/O_2$ *flow rate.* Thin Solid Films. **518**(22): p. 6403-6407.
83. Lee, M.W., et al., *Oxygen plasma effects on performance of pentacene thin film transistor*. Japanese Journal of Applied Physics, Part 1: Regular Papers and Short Notes and Review Papers, 2003. **42**(7 A): p. 4218-4221.
84. Cahyadi, T., et al., *Electret mechanism, hysteresis, and ambient performance of sol-gel silica gate dielectrics in pentacene field-effect transistors.* Applied Physics Letters, 2007. **91**(24): 242107.
85. Tan, H.S., et al., *The effect of dielectric constant on device mobilities of high-performance, flexible organic field effect transistors.* Applied Physics Letters, 2009. **94**(26): 263303.

86. Cahyadi, T., et al., *Enhancement of carrier mobilities of organic semiconductors on sol-gel dielectrics: investigations of molecular organization and interfacial chemistry effects.* Advanced Functional Materials, 2009. **19**(3): p. 378-385.
87. Facchetti, A., *Dielectric materials: Gels excel.* Nature Materials, 2008. **7**(11): p. 839-840.
88. Cho, J.H., et al., *Printable ion-gel gate dielectrics for low-voltage polymer thin-film transistors on plastic.* Nature Materials, 2008. **7**(11): p. 900-906.
89. Cho, J.H., et al., *High-capacitance ion gel gate dielectrics with faster polarization response times for organic thin film transistors.* Advanced Materials, 2008. **20**(4): p. 686-690.
90. Noh, Y.Y., et al., *Downscaling of self-aligned, all-printed polymer thin-film transistors (Nature Nanotechnology (2007) 2, (784-789)).* Nature Nanotechnology, 2008. **3**(1): p. 58.
91. Facchetti, A., et al., *Gate dielectrics for organic field-effect transistors: New opportunities for organic electronics.* Advanced Materials, 2005. **17**(14): p. 1705-1725.
92. Yang, S.Y., et al., *Low-voltage pentacene field-effect transistors with ultrathin polymer gate dielectrics.* Applied Physics Letters, 2006. **88**(17): 173507.
93. Yoon, M.H., et al., *Low-voltage organic field-effect transistors and inverters enabled by ultrathin cross-linked polymers as gate dielectrics.* Journal of the American Chemical Society, 2005. **127**(29): p. 10388-10395.
94. Chua, L.L., et al., *High-stability ultrathin spin-on benzocyclobutene gate dielectric for polymer field-effect transistors.* Applied Physics Letters, 2004. **84**(17): p. 3400-3402.
95. Chua, L.L., et al., *Observation of field-effect transistor behavior at self-organized interfaces.* Advanced Materials, 2004. **16**(18): p. 1609-1615.
96. Das, R.N., et al., *Printable electronics: Towards materials development and device fabrication.* Circuit World, 2011. **37**(1): p. 38-45.
97. Tchoul, M.N., et al., *Assemblies of titanium dioxide-polystyrene hybrid nanoparticles for dielectric applications.* Chemistry of Materials, 2010. **22**(5): p. 1749-1759.
98. Kim, P., et al., *High energy density nanocomposites based on surface-modified* $BaTiO_3$ *and a ferroelectric polymer.* ACS Nano, 2009. **3**(9): p. 2581-2592.
99. Zhou, T., et al., *Improving dielectric properties of* $BaTiO_3$*/ferroelectric polymer composites by employing surface hydroxylated* $BaTiO_3$ *nanoparticles.* ACS Applied Materials and Interfaces, 2011. **3**(7): p. 2184-2188.
100. Li, J., et al., *Electrical energy storage in ferroelectric polymer nanocomposites containing surface-functionalized* $BaTiO_3$ *nanoparticles.* Chemistry of Materials, 2008. **20**(20): p. 6304-6306.
101. Morris, J.E., *Nanopackaging: Nanotechnologies and electronics packaging*. 2007.
102. Rasul, A., et al., *Flexible high capacitance nanocomposite gate insulator for printed organic field-effect transistors.* Thin Solid Films, 2010. **518**(23): p. 7024-7028.
103. Ramesh, S., et al., *Dielectric nanocomposites for integral thin film capacitors: Materials design, fabrication and integration issues.* IEEE Transactions on Advanced Packaging, 2003. **26**(1): p. 17-24.
104. Tuncer, E., et al., *Electrical properties of epoxy resin based nano-composites.* Nanotechnology, 2007. **18**(2): 025703.
105. Iijima, M., et al., *Surface modification of* $BaTiO_3$ *particles by silane coupling agents in different solvents and their effect on dielectric properties of* $BaTiO_3$*/epoxy composites.* Colloids and Surfaces A: Physicochemical and Engineering Aspects, 2009. **352**(1-3): p. 88-93.
106. Ramajo, L., et al., $BaTiO_3$*-epoxy composites for electronic applications.* International Journal of Applied Ceramic Technology, 2010. **7**(4): p. 444-451.
107. Dang, Z.M., et al., *Fabrication and dielectric characterization of advanced* $BaTiO_3$*/polyimide nanocomposite films with high thermal stability.* Advanced Functional Materials, 2008. **18**(10): p. 1509-1517.

108. Xie, L., et al., *Core-shell structured poly(methyl methacrylate)/BaTiO$_3$ nanocomposites prepared by in situ atom transfer radical polymerization: A route to high dielectric constant materials with the inherent low loss of the base polymer.* Journal of Materials Chemistry, 2011. **21**(16): p. 5897-5906.
109. Kobayashi, Y., et al., *Fabrication of barium titanate nanoparticles-polymethylmethacrylate composite films and their dielectric properties.* Polymer Engineering and Science, 2009. **49**(6): p. 1069-1075.
110. Jung, M., et al., *All-Printed and roll-to-roll-printable 13.56-MHz-operated 1-bit RF tag on plastic foils.* IEEE Transactions on Electron Devices, 2010. **57**(3): p. 571-580.
111. Ryu, G.S., et al., *A printed OTFT-backplane for AMOLED display.* Organic Electronics: physics, materials, applications, 2013. **14**(4): p. 1218-1224.
112. Jacob, S., et al., *High performance printed N and P-type OTFTs for complementary circuits on plastic substrate*. 2012.
113. Husermann, R., et al., *Gate bias stress in pentacene field-effect-transistors: Charge trapping in the dielectric or semiconductor.* Applied Physics Letters, 2011. **99**(8): 083303.
114. Chung, S., et al., *All-inkjet-printed organic thin-film transistor inverter on flexible plastic substrate.* IEEE Electron Device Letters, 2011. **32**(8): p. 1134-1136.
115. Huebler, A.C., et al., *Ring oscillator fabricated completely by means of mass-printing technologies.* Organic Electronics: physics, materials, applications, 2007. **8**(5): p. 480-486.
116. Hübler, A.C., et al., *Three-dimensional integrated circuit using printed electronics.* Organic Electronics: physics, materials, applications, 2011. **12**(3): p. 419-423.
117. Hoppe, H., et al., *Organic solar cells: An overview.* Journal of Materials Research, 2004. **19**(7): p. 1924-1945.
118. Mishra, A., et al., *Small molecule organic semiconductors on the move: Promises for future solar energy technology.* Angewandte Chemie - International Edition, 2012. **51**(9): p. 2020-2067.
119. Singh, R.P., et al., *Polymer solar cells: An overview.* Macromolecular Symposia, 2013. **327**(1): p. 128-149.
120. Bundgaard, E., et al., *Low band gap polymers for organic photovoltaics.* Solar Energy Materials and Solar Cells, 2007. **91**(11): p. 954-985.
121. Bao, Z., et al., *Soluble and processable regioregular poly(3-hexylthiophene) for thin film field-effect transistor applications with high mobility.* Applied Physics Letters, 1996. **69**(26): p. 4108-4110.
122. Koster, L.J.A., et al., *Ultimate efficiency of polymer/fullerene bulk heterojunction solar cells.* Applied Physics Letters, 2006. **88**(9): 093511.
123. Kunugi, Y., et al., *Organic Field-Effect Transistor Using Oligoselenophene as an Active Layer.* Chemistry of Materials, 2002. **15**(1): p. 6-7.
124. Heeney, M., et al., *Regioregular poly(3-hexyl)selenophene: A low band gap organic hole transporting polymer.* Chemical Communications, 2007(47): p. 5061-5063.
125. Lee, W.-H., et al., *Synthesis and characterization of new selenophene-based conjugated polymers for organic photovoltaic cells.* Journal of Polymer Science Part A: Polymer Chemistry, 2012. **50**(3): p. 551-561.
126. Crouch, D.J., et al., *Thiophene and Selenophene Copolymers Incorporating Fluorinated Phenylene Units in the Main Chain: Synthesis, Characterization, and Application in Organic Field-Effect Transistors.* Chemistry of Materials, 2005. **17**(26): p. 6567-6578.
127. Ong, T.-T., et al., *Synthesis, characterization and electrochemical properties of polybiselenophene.* Polymer, 2003. **44**(19): p. 5597-5603.
128. Ong, B.S., et al., *Thiophene polymer semiconductors for organic thin-film transistors.* Chemistry - A European Journal, 2008. **14**(16): p. 4766-4778.
129. Jiang, X.M., et al., *Spectroscopic Studies of Photoexcitations in Regioregular and Regiorandom Polythiophene Films.* Advanced Functional Materials, 2002. **12**(9): p. 587-597.

130. Chang, R., et al., *Aggregated states of luminescent conjugated polymers in solutions.* Chemical Physics Letters, 2000. **317**(1-2): p. 153-158.
131. Wu, T.Y., et al., *Synthesis and optically acid-sensory and electrochemical properties of novel polyoxadiazole derivatives.* Macromolecules, 2004. **37**(3): p. 725-733.
132. Ong, B., et al., *Structurally Ordered Polythiophene Nanoparticles for High-Performance Organic Thin-Film Transistors.* Advanced Materials, 2005. **17**(9): p. 1141-1144.
133. Ie, Y., et al., *Dendritic oligothiophene bearing perylene bis(dicarboximide) groups as an active material for photovoltaic device.* Chemical Communications, 2009(10): p. 1213-1215.
134. Jang, J., et al., *High Tg cyclic olefin copolymer gate dielectrics for N,N'-ditridecyl perylene diimide based field-effect transistors: Improving performance and stability with thermal treatment.* Advanced Functional Materials. **20**(16): p. 2611-2618.
135. Chen, Z., et al., *Naphthalenedicarboximide- vs perylenedicarboximide-based copolymers. synthesis and semiconducting properties in bottom-gate N-channel organic transistors.* Journal of the American Chemical Society, 2009. **131**(1): p. 8-9.
136. Fischer, M.K.R., et al., *Dendritic oligothiophene-perylene bisimide hybrids: Synthesis, optical and electrochemical properties.* Journal of Materials Chemistry, 2009. **19**(8): p. 1129-1141.
137. Ie, Y., et al., *Physical properties, charge carrier mobility, and photovoltaic performance of dendritic oligothiophene bearing naphthalene bis(dicarboximide) groups.* Japanese Journal of Applied Physics. **49**(1 Part 2): 01AC03.
138. Ie, Y., et al., *Photovoltaic performance and charge carrier mobility of dendritic oligothiophene bearing perylene bis(dicarboximide) groups.* Synthetic Metals, 2009. **159**(9-10): p. 797-801.
139. Ma, C.Q., et al., *Functionalized 3D oligothiophene dendrons and dendrimers - Novel macromolecules for organic electronics.* Angewandte Chemie - International Edition, 2007. **46**(10): p. 1679-1683.
140. Negishi, N., et al., *Ambipolar characteristics of dendritic oligothiophene/fullerene linkage molecules.* Chemistry Letters, 2007. **36**(4): p. 544-545.
141. Yan, H., et al., *A high-mobility electron-transporting polymer for printed transistors.* Nature, 2009. **457**(7230): p. 679-686.
142. Gallaher, J.K., et al., *Controlled aggregation of peptide-substituted perylene-bisimides.* Chemical Communications, 2012. **48**(64): p. 7961-7963.
143. Kim, B.G., et al., *Organic dye design tools for efficient photocurrent generation in dye-sensitized solar cells: Exciton binding energy and electron acceptors.* Advanced Functional Materials, 2012. **22**(8): p. 1606-1612.
144. Periasamy, M., et al., *Methods of enhancement of reactivity and selectivity of sodium borohydride for applications in organic synthesis.* Journal of Organometallic Chemistry, 2000. **609**(1-2): p. 137-151.
145. Qian, H., et al., *Heterocyclic Annelated Di(perylene bisimide): Constructing Bowl-Shaped Perylene Bisimides by the Combination of Steric Congestion and Ring Strain.* The Journal of Organic Chemistry, 2009. **74**(16): p. 6275-6282.
146. Ortiz, R.P., et al., *High-k organic, inorganic, and hybrid dielectrics for low-voltage organic field-effect transistors.* Chemical Reviews, 2010. **110**(1): p. 205-239.
147. Maliakal, A., et al., *Inorganic oxide core, polymer shell nanocomposite as a high-k gate dielectric for flexible electronics applications.* Journal of the American Chemical Society, 2005. **127**(42): p. 14655-14662.
148. Yildirim, F.A., et al., *Spin-cast composite gate insulation for low driving voltages and memory effect in organic field-effect transistors.* Applied Physics Letters, 2007. **90**(8): 083501.
149. Baeg, K.J., et al., *Toward printed integrated circuits based on unipolar or ambipolar polymer semiconductors.* Advanced Materials, 2013. **25**(31): p. 4210-4244.

150. Jung, S.W., et al., *Low-voltage-operated top-gate polymer thin-film transistors with high capacitance poly(vinylidene fluoride-trifluoroethylene)/poly(methyl methacrylate) dielectrics.* Journal of Applied Physics, 2010. **108**(10): 102810.
151. Mendes, S.F., et al., *Effect of filler size and concentration on the structure and properties of poly(vinylidene fluoride)/*$BaTiO_3$ *nanocomposites.* Journal of Materials Science, 2012. **47**(3): p. 1378-1388.
152. Mennig, M., et al., *Multilayer NIR reflective coatings on transparent plastic substrates from photopolymerizable nanoparticulate sols.* Thin Solid Films, 1999. **351**(1-2): p. 225-229.
153. Luo, K., et al., *Dispersion and functionalization of nonaqueous synthesized zirconia nanocrystals via attachment of silane coupling agents.* Langmuir, 2008. **24**(20): p. 11497-11505.
154. Kilaru, M.K., et al., *Strong charge trapping and bistable electrowetting on nanocomposite fluoropolymer:* $BaTiO_3$ *dielectrics.* Applied Physics Letters, 2007. **90**(21): 212906.
155. Wang, W., et al., *Hysteresis mechanism in low-voltage and high mobility pentacene thin-film transistors with polyvinyl alcohol dielectric.* Applied Physics Letters, 2012. **101**(3): 033303.